

Nanoconfined MMA Polymerization and Structural Recovery in Ge-Se Glasses

by

Haoyu Zhao, B.Sc. Engg.

A Dissertation

In

Chemical Engineering

Submitted to the Graduate Faculty
of Texas Tech University in
Partial Fulfillment of
the Requirements for
the Degree of

DOCTOR OF PHILOSOPHY

Approved

Sindee L. Simon
Chair of Committee

Gregory B. McKenna

Ronald C. Hedden

Edward L. Quitevis

Mark Sheridan
Dean of the Graduate School

December, 2014

Copyright 2014, Haoyu Zhao

ACKNOWLEDGMENTS

It is a pleasure to thank the support of many people who made the completion of this doctoral dissertation possible. I would like to express my sincere gratitude to all of them. First of all, I would like to gratefully and sincerely thank Professor Sindee Simon for her guidance, understanding, patience, motivation and encouragement I received throughout the research work. She has always made herself available to clarify my doubts despite her busy schedules and I consider it as a great opportunity to do my doctoral program under her guidance and to learn from her research expertise. Thanks for her input and valuable discussions. I would like to thank Professor Gregory McKenna and Professor Ronald Hedden for the impressive lectures and perceptive advice with my best respect. I would also like to express my appreciation to Professor Edward Quitevis and Professor Shiren Wang for their valuable opinion and also for participating in my committee from my qualifying exam.

I would like to thank all the members of Professor Simon's group, especially, Dr. Yung Koh for his continuous help in DSC of absolute heat capacity measurements. I would also like to express my appreciation to Dr. Ziniu Yu for his help in GPC study.

I gratefully acknowledge endless support from my father, my mother, and my fiancé. They not only take good care of me in personal life but also encourage me to overcome all the difficulties I faced during the past six years. I cannot imagine how I can finish this long journey without their love and sacrifices.

Table of Contents

ACKNOWLEDGMENTS	II
ABSTRACT	V
LIST OF TABLES	VII
LIST OF FIGURES	VIII
CHAPTER 1: INTRODUCTION	1
References	5
CHAPTER 2: BACKGROUND	10
2.1 Kinetics of Free Radical Polymerization	10
2.2 Autoacceleration Phenomenon (Gel Effect)	12
2.3 High Temperature PMMA Polymerization.....	15
2.4 Thermodynamics of Free Radical Polymerization.....	18
2.5 Statistical Model for Stereoregular Chain Propagation	19
2.6 Structural Recovery (Physical Aging Process)	22
2.7 Intermediate Phase of Chalcogenide Glasses.....	24
References	26
CHAPTER 3: METHYL METHACRYLATE POLYMERIZATION IN NANOPOROUS CONFINEMENT	32
3.1 Introduction	32
3.2 Methodology	34
3.2.1 Materials.....	34
3.2.2 DSC Measurements.....	35
3.3 Results	37
3.4 Discussion	41
References	45
CHAPTER 4: THE EFFECT OF NANOCONFINEMENT ON METHYL METHACRYLATE POLYMERIZATION: T_g, MOLECULAR WEIGHT, AND TACTICITY	61
4.1 Introduction	61
4.2 Methodology	63
4.2.1 Materials.....	63
4.2.2 Polymer Characterization.....	64
4.3 Results	65
4.4 Discussion	72
4.5 Conclusion	76
References	78
CHAPTER 5: EQUILIBRIUM FREE- RADICAL POLYMERIZATION OF METHYL METHACRYLATE UNDER NANOCONFINEMENT	96
5.1 Introduction	96
5.2 Methodology	99
5.2.1 Materials.....	99
5.2.2 Polymerization.....	99
5.3 Results	102
5.4 Discussion	107

5.5 Conclusion	108
References	110
CHAPTER 6: THE KINETICS OF THE GLASS TRANSITION AND PHYSICAL AGING IN GERMANIUM SELENIDE GLASSES	124
6.1 Introduction	124
6.2 Methodology	127
6.2.1 Materials Preparation	127
6.2.2 DSC Measurements	127
6.3 Results	130
6.4 Discussion	139
6.5 Conclusion	141
References	142
CHAPTER 7: CONCLUSION.....	164
References	167
CHAPTER 8: FUTURE WORK	170
8.1 Generalization	170
8.2 Synthesized tool to obtain prespecified properties	170
8.3 Very high temperature polymerization	171
8.4 In situ polymerized nanocomposites	174
References	176

ABSTRACT

The effect of nanoconfinement on the free radical polymerization of methyl methacrylate (MMA) is investigated using differential scanning calorimetry, gel permeation chromatography, and ^1H nuclear magnetic resonance. Both hydrophobic and hydrophilic controlled pore glass (CPG) with pore diameters of 13 to 110 nm are used for polymerization under nanoconfinement. The effective reaction rates are unchanged in hydrophobic pores but significantly increased in hydrophilic pores. For both pore surfaces, the time required to reach autoacceleration decreases with decreasing pore size, with the effect much more pronounced in the hydrophilic pores. These results are quantitatively described by a model incorporated with nanoconfinement effects using free volume theory. For the PMMA synthesized under CPG, the number-average and weight-average molecular weights increase because the onset of autoacceleration shifts to shorter times, whereas the polydispersity index at full conversion decreases relative to the bulk value. The higher percentages of isotactic-rich triads in hydrophilic pores are observed and the dependence of tacticity on temperature is predicted by the first-order Markov model. In addition, the glass transition temperature increases for both pore surfaces, but the increase in hydrophilic pores is more pronounced. For the high temperature equilibrium polymerization, the ceiling temperature is shifted to lower temperatures in 13 nm diameter nanopores, with pore surface chemistries showing no significant effects. The observed lower equilibrium conversion and ceiling temperatures are attributed to the larger negative change in entropy on propagation, which is a constant for the bulk equilibrium

polymerization but changes within increasing polymerization temperature in nanopores presumably due to the reduced chain length at high temperature.

The kinetics associated with the glass transition is investigated using conventional DSC for germanium selenide glasses with Ge content ranging from 0 to 30 atom %. As Ge content increases, the glass transition region broadens and the step change in heat capacity at T_g decreases. The change in enthalpy linearly increases with the logarithm of aging time and then levels off at an equilibrium value that increases with decreasing aging temperature. The time required to reach equilibrium increases with decreasing aging temperature and, at a given distance from T_g , the time increases with decreasing germanium content. The results indicate that all samples show expected structural recovery, and no evidence is found for an intermediate phase characterized by high stability and absence of physical aging.

LIST OF TABLES

3.1. Specifications of CPGs, as provided by manufacturer.....	50
3.2. Total heat of reaction and the time to reach autoacceleration of the reactant under nanoscale constraints at different sizes at 80 °C.....	51
4.1. Tacticity versus temperatures for bulk and nanoconfined PMMA.....	85
4.2. T_g of synthesized samples in pores versus after MMA removal and extraction.....	86
5.1. The fitting results for equilibrium conversion as function of inverse temperature for bulk and nanoconfined PMMA.....	114
5.2. Values for ΔS_p assuming $\Delta H_p = -56$ kJ/mol; and a function of temperature ($\Delta S_p(T)$).....	115
6.1. Parameters characterizing relaxation in the glass transition region for various Ge-Se glasses.....	152
6.2. Aging temperatures used for different glass compositions.....	153

LIST OF FIGURES

2.1. Comparison of conversion versus reaction time from literature [2].	13
2.2. The evolution of conversion for bulk and nanoconfined at 90 °C [2].	14
2.3. Monomer conversion as function of temperatures from literature [15].....	17
2.4. Schematic of vinyl monomer propagation by chain end effect. [1].....	20
2.5. Schematic of vinyl monomer propagation by penultimate effect. [1]	21
2.6. Schematic of the evolution of volume or enthalpy on physical aging.	24
3.1. Heat flow versus time of isothermal polymerization at different temperatures for representative bulk samples.....	52
3.2a. Heat flow versus time of isothermal polymerization at 80 °C for representative samples in nanoconfined hydrophobic CPGs of diameter D. A representative bulk sample ($D=\infty$) is shown for comparison.	53
3.2b. Heat flow versus time of isothermal polymerization at 80 °C for representative samples in nanoconfined hydrophilic CPGs of diameter D. A representative bulk sample ($D=\infty$) is shown for comparison.....	54
3.3. The induction time for bulk and samples in nanoconfined pores as a function of reciprocal temperature. Closed symbols indicate the nanoconfined hydrophobic samples and open symbols indicate the nanoconfined hydrophilic samples.....	55
3.4a. Conversion versus time of isothermal polymerization for representative bulk and nanoconfined hydrophobic samples at 80 °C.....	56
3.4b. Conversion versus time of isothermal polymerization for representative bulk and nanoconfined hydrophilic samples at 80 °C.....	57
3.5. The effective rate constant prior to autoacceleration normalized by the bulk value for nanoconfined samples as a function of reciprocal pore diameter. Closed symbols indicate the nanoconfined hydrophobic samples and open symbols indicate the nanoconfined hydrophilic samples.	58
3.6. An Arrhenius plot for the effective rate constant prior to autoacceleration for bulk and nanoconfined samples. Closed symbols indicate the nanoconfined hydrophobic samples and open symbols indicate the nanoconfined hydrophilic samples.	59
3.7. The time required to reach autoacceleration normalized by the time for the bulk samples as a function of reciprocal diameter. Closed symbols indicate the nanoconfined hydrophobic samples and open symbols indicate the nanoconfined hydrophilic samples.	60
4.1a. Number-average molecular weight as function of conversion for PMMA synthesized in nanopores and in bulk. Symbols represent experimental data and lines represent the previous modeling results [11,12].....	87

4.1b. Weight-average molecular weight as function of conversion for PMMA synthesized in nanopores and in bulk. Symbols represent experimental data and lines represent the previous modeling results [11,12].....	88
4.2. The polydispersity (PDI) versus conversion for hydrophobic/hydrophilic pores and bulk at 80 °C. Symbols represent the experimental data. The dashed line is the guide to the eye. The inset figure is the prediction from the previous modeling work [11,12]..	89
4.3. ¹ H NMR spectra of α -CH ₃ of PMMA in CDCl ₃ for PMMA synthesized at 80 °C in bulk (top panel) or in hydrophilic 13 nm pores (bottom panel).	90
4.4. The dependence of isotactic triads, atactic triads, and syndiotactic triads on temperature for PMMA synthesized in nanopores and in bulk. The symbols represent NMR experimental data and lines are fitting results from first-order Markov model.....	91
4.5. The dependence of isotactic to syndiotactic diad ratio (P_i/P_s) on temperature for PMMA synthesized in nanopores and in bulk. The symbols represent diads calculated from NMR experimental data and lines are a fit to equation (4.2).	92
4.6. Heat flow versus temperature for PMMA polymerized in bulk and synthesized under nanoconfined conditions at 80 °C. The dashed lines and solid lines represent samples after extraction and after MMA removal, respectively. The vertical line indicates the glass transition temperature.....	93
4.7a. Heat flow versus temperature for bulk and nanoconfined samples polymerized in pinhole at 60 °C. The solid line indicates the glass transition temperature.	94
4.7b. Heat flow versus temperature for bulk and nanoconfined samples polymerized in pinhole at 95 °C. The solid line indicates the glass transition temperature.	95
5.1. Schematic plot to show how entropy changes under nanoconfinement. Solid lines represent the entropy in bulk and the dashed lines represent the entropy in nanoconfined system.	116
5.2a. Schematic of one step method to investigate the equilibrium reaction at temperatures from 60 to 140 °C for bulk polymerization and from 60 to 130 °C for nanoconfined polymerization.	117
5.2b. Schematic of two step method to investigate the equilibrium reaction at higher temperature.....	118
5.3ab. The equilibrium conversion as a function of the reciprocal of polymerization temperature. Dashed lines represent the linear fitting results, where Figure 5.3a is the best fit and Figure 5.3b is the fixed slope fit.....	119
5.4. The heat of reaction and conversion as a function of isothermal temperature for bulk using one step (open symbols) and two step (solid symbols) methods. The dashed lines are based on the equation (2.16) using constant value of ΔH_p of bulk value (-56 kJ/mol).....	120

5.5. The heat of reaction and conversion as a function of isothermal temperature for both bulk and nanoconfined samples using one step (open symbols) and two step (solid symbols) methods. The dashed lines are based on the equation (2.16) using constant value of ΔH_p of bulk value (-56 kJ/mol) and the solid line is the exponential model using ΔS_p as function of temperature.	121
5.6. The difference between the entropy for the propagation reaction of bulk samples and nanoconfined samples as a function of polymerization temperature. Open symbols represent data from one step method above 110 °C and solid symbols represent data from two step method. Dashed line represents the exponential fitting results. The inset shows $[\ln(\Delta S_{p,bulk} - \Delta S_{p,conf})]$ against the reciprocal temperature. Dashed line represents the linear fitting results.....	122
5.7. The kinetic chain length changes ($\ln v$) with the reciprocal temperatures based on equation (5.6). Open symbols represent chain length data from the experimental number average molecular weight by the ratio of M_n/M_o [14]. Solid symbols represent chain length data from the calculated results based on the equations from previous work [25,26]. Dashed line represents the linear fitting results. ..	123
6.1. Schematic for DSC experiment of aging response	154
6.2. Absolute heat capacity versus temperature for average coordination number ranging from 2.0 (Se) to 2.6 ($Ge_{30}Se_{70}$). The dashed line is a guide to the eye..	155
6.3. Normalized heat capacity versus temperature for different composition Ge-Se alloys for heating rates of 10 K/min (solid line) and 0.1 K/min (dashed line)..	156
6.4. T_g and ΔC_p as a function of average coordination number. Squares and circles refer to T_g and ΔC_p , respectively. The solid symbols indicate data obtained from conventional DSC after cooling at 10 K/min. The open symbols are from the step scan technique. The red line is the fit to equation (6.6) and the green line is the fit to equation (6.7).....	157
6.5. The dependence of fictive temperature on cooling rate for Ge_xSe_{100-x} samples with the fictive temperature obtained on cooling at 10 K/min serving as reference. The $r_c = 2.0$ data are taken from reference [34]......	158
6.6. Representative DSC heat flow curves as a function of the aging time t for an aging temperature $T_a \approx T_g - 15$ K for various composition glasses.	159
6.7. The enthalpy loss on aging (ΔH_a) as a function of the logarithm of the isothermal aging time for the aging temperatures nominally 5 K, 10 K, and 15 K below T_g . The dashed lines are fits using the KWW function. Data for pure selenium, $r_c = 2.0$, are taken from reference [34].	160
6.8. $\Delta H_{a\infty}/\Delta C_p$ as a function of the difference between the reference fictive temperature and the aging temperature for various compositions. The line represents the expectation from equation (6.10). Data for pure selenium, $r_c = 2.0$, are taken from reference [34].	161

- 6.9. The dependence of the aging rate on the average coordination number. The inset shows aging rate versus aging temperature plotted as distance from the reference fictive temperature. The $r_c = 2.0$ data are taken from reference [34]. 162
- 6.10. The time required to reach equilibrium (t_∞) as a function of average coordination number for different aging temperatures. The dashed line is a guide to the eye. The $r_c = 2.0$ data is taken from reference [34] and the open symbols represent extrapolated values. The inset is a schematic Angell plot [55] showing the logarithm of the relaxation time versus T_g/T for strong and fragile glass formers. 163

CHAPTER 1

INTRODUCTION

Glass is an amorphous solid and can be divided into two categories: organic glass and inorganic glass. Poly(methyl methacrylate) (PMMA) is a well known transparent organic glass in industrial field. The conventional processing technology to obtain PMMA is through free-radical bulk or solution polymerization resulting transparent and brittle glass with moderate molecular weight. The kinetics and thermodynamics of PMMA bulk polymerization has been systematically studied in literature. [1] However, when the reaction environment is restricted to nano-scale geometry, the properties of synthesized PMMA change, and this has become an attractive topic that motivated the researchers over the past two decades to investigate the effects of nanoconfinement upon polymerization. [2] For example, nanoconfinement was found to increase molecular weight and decrease polydispersity index (PDI) [2-4] or decrease molecular weight and increase PDI [5]. Changes in tacticity, final yield of polymer and chain conformation were also observed [4]. Thus, it is practical to regard nanoconfined matrix as a synthesis tool [3,6,7] to produce a well-modified PMMA glass with desired properties, and that is our focus of this dissertation.

On the other hand, chalcogenide glass is a useful inorganic glass which is widely used in optical and remote sensing applications. [8,9] Several research groups [10,11] have proposed an ideal intermediate phase [12,13] of the binary Ge-Se

chalcogenide glass in which the influence of aging behavior on glass properties is minimized. [14] Although the existence of the intermediate phase, which occurs at an atom percentage of Ge/Se = 0.25, has been reported by calorimetric studies using conventional differential scanning calorimeter (DSC) [15] or temperature-modulated DSC (TMDSC) [16], opposite conclusions have been drawn depending on techniques, [14] aging temperature, [17] and storage conditions [18]. Therefore, the proof of the intermediate phase is further examined as part of this work.

This dissertation contains eight chapters. In Chapter 2, the general background related to the kinetics and thermodynamics of free-radical polymerization, autoacceleration effect in bulk and nanopores, the statistical model of stereospecific propagation, and the aging behavior associated with binary Ge-Se are described. Chapters 3-6 are taken from original journal manuscripts including introduction, methodology, results, discussion and conclusions. Certain parts of the journal articles are rewritten to avoid the redundancy and to add additional supporting information.

Chapter 3 focuses on the enhanced reactivity of nanoconfined methyl methacrylate (MMA) polymerization and the influence of nanoconfinement size and surface chemistry. This work is motivated by previous modeling work from our laboratory [19] dealing with the polymerization of MMA under nanopores. Unlike other research groups focusing on the changes in molecular weight or tacticity for PMMA synthesized in nanopores [2-7], the changes in effective reaction rate, the onset of autoacceleration and the apparent activation energy are investigated in controlled pores glasses for both hydrophobic and hydrophilic pore surfaces and for

pore diameter ranging from 13 nm to 110 nm. The results, which were published in *Polymer* [20], showed that samples synthesized in hydrophilic pores have higher initial propagation rate and lower activation energy due to the surface catalytic effects compared with samples synthesized in hydrophobic pores. In addition, the onset of autoacceleration shifts to shorter times for both cases with effects in hydrophilic pores being more pronounced. The reduced times to reach autoacceleration are explained by a decreased chain diffusivity under nanoconfinement and the previous modeling work [19] predicted the trend. The experimental data presented in the dissertation have been quantitatively modeled using an extension of Verros's model [20] by Begum and published in *Polymer* [21,22]; the modeling results are not included in this dissertation.

Chapter 4 focuses on the changes in properties for the PMMA samples synthesized under the smallest 13 nm pore size for both hydrophobic and hydrophilic samples. The number-average and weight-average molecular weights (M_n and M_w , respectively) measured by Yu and Hedden using gel permeation chromatography (GPC) are found to increase in nanopores due to the earlier onset of autoacceleration, which is consistent with literature [2-4,6,7]. Moreover, T_g is significantly increased in hydrophobic pores solely due to confinement effect and the increased magnitude of T_g is even higher in hydrophilic pores due to the added specific interaction between PMMA and pore surface silanol groups. Similar experimental observations were reported for PMMA ultrathin films [24] and PMMA synthesized in nanocomposites [25]. The impressive part of the modified PMMA properties in Chapter 4 is that

MMA/CPG system in hydrophilic pores tends to produce a more highly isotactic PMMA compared with other literature [4,26]. This Chapter has been published in *Polymer* [27].

Extending work on nanoconfined MMA polymerization, Chapter 5 focuses on the equilibrium reaction of MMA at high temperatures. The effect of nanoconfinement is found to shift the ceiling temperature to lower temperatures indicating that the change in entropy on propagation decreases in nanopores. Unlike the change in entropy on propagation which is independent of temperature for bulk polymerization [1], the scaling in the literature [28-31] indicated that the change in entropy for the nanoconfined reactor is associated with chain length and may, thus, depend on temperature. The paper is in preparation and will be submitted soon.

In Chapter 6, we change the research subject from organic glass (PMMA) to inorganic glass (Ge-Se) to study the aging behavior on network structure. The various compositions Ge-Se glasses are synthesized by Professor Sabyasachi Sen's group from UC Davis. Since the glass state is non-equilibrium state, glasses spontaneously evolve to equilibrium in a process called structural recovery or physical aging. Some research groups [10,11,32] have suggested a specific composition of chalcogenide glasses that does not show aging behavior. However, based on the preliminary work from Dr. Marek Pyda, our work published in the *Journal of Non-Crystalline Solids* [33], demonstrated that all Ge-Se samples, independent of composition, show the typical structure recovery phenomenon. The existence of an ideal "non-aging" phase is not found.

References

1. Odian G. Principles of Polymerization. 3rd ed. New York: Wiley; 2004.
2. Li XC, King TA, Pallikari-Viras F. "Characteristics of composites based of PMMA modified gel silica glasses" *Journal of Non-Crystalline Solids* 1994;170:243-249.
3. Ng SM, Ogino S, Aida T, Koyano KA, Tatsumi T. "Free radical polymerization within mesoporous zeolite channels" *Macromolecular Rapid Communications* 1997;18:991-996.
4. Uemura T, Ono Y, Kitagawa K, Kitagawa S. "Radical polymerization of vinyl monomers in porous coordination polymers: Nanochannel size effects on reactivity, molecular weight, and stereostructure" *Macromolecules* 2008;41:87-94.
5. Pallikari-Viras F, Li XC, King TA. "Thermal analysis of PMMA/gel silica glass composites" *Journal of Sol-Gel Science and Technology* 1996;7:203-209.
6. Kageyama K, Ng SM, Ichikawa H, Aida T. "Macromolecular synthesis using mesoporous zeolites" *Macromolecular Symposia* 2000;157:137-142.
7. Ikeda K, Kida M, Endo K. "Polymerization of methyl methacrylate with radical initiator immobilized on the inside wall of mesoporous silica" *Polymer Journal* 2009;41:672-678.
8. Zakery A. "Pulsed laser deposition of chalcogenide films for nonlinear photonic applications" *Journal of Optoelectronics and Advanced Materials* 2005;7:1143-1155.

9. Golovchak R, Shpotyuk O, Kozdras A, Bureau B, Vlček M, Ganjoo A, Jain H. "Atomistic model of physical ageing in Se-rich As–Se glasses" *Philosophical Magazine* 2007;87:4323-4334.
10. Thorpe MF, Jacobs DJ, Chubynsky MV, Phillips JC. "Self-organization in network glasses" *Journal of Non-Crystalline Solids* 2000;266-269:859-866.
11. Wang Y, Boolchand P, Micoulaut M. "Glass structure, rigidity transitions and the intermediate phase in the Ge–As–Se ternary" *Europhysics Letters* 2000;52:633-639.
12. Phillips JC. "Topology of covalent non-crystalline solids I: Short-range order in chalcogenide alloys" *Journal of Non-Crystalline Solids* 1979;34:153-181.
13. Lucovsky G, Phillips JC. "Intermediate phases in binary and ternary alloys: a new perspective on semi-empirical bond constraint theory" *Journal of Physics: Condensed Matter* 2007;19:455218(1-20).
14. Shpotyuk O, Hyla M, Boyko V, Golovchak R. "Reversibility windows in selenide-based chalcogenide glasses" *Physica B: Condensed Matter* 2008;403:3830-3837.
15. Golovchak R, Gorecki Cz, Kozdras A, Shpotyuk O. "Physical ageing effects in vitreous arsenic selenides" *Solid State Communications* 2006;137:67-69.
16. Qu T, Boolchand P. "Shift in elastic phase boundaries due to nanoscale phase separation in network glasses: the case of $\text{Ge}_x\text{As}_x\text{S}_{1-2x}$ " *Philosophical Magazine* 2005;85:875-884.

17. Golovchak R, Kozdras A, Shpotyuk O, Gorecki Cz, Kovalskiy A, Jain H. "Temperature-dependent structural relaxation in $As_{40}Se_{60}$ glass" *Physics Letters A* 2011;375:3032–3036.
18. Elabbar AA, Abu-Sehly AA. "Structural relaxation and rigidity transition in aged and rejuvenated As_xSe_{100-x} glasses" *Physica B: Condensed Matter* 2011;406:4261-4265.
19. Begum F, Simon SL. "Modeling methyl methacrylate free radical polymerization in nanoporous confinement" *Polymer* 2011;52:1539-1545.
20. Verros GD, Latsos T, Achilias DS. "Development of a unified framework for calculating molecular weight distribution in diffusion controlled free radical bulk homo-polymerization" *Polymer* 2005;46:539–552.
21. Begum F, Zhao HY, Simon SL. "Modeling methyl methacrylate free radical polymerization: Reaction in hydrophilic nanopores" *Polymer* 2012;53:3238-3244.
22. Begum F, Zhao HY, Simon SL. "Modeling methyl methacrylate free radical polymerization: Reaction in hydrophobic nanopores" *Polymer* 2012;53:3261-3268.
23. Zhao HY, Simon SL. "Methyl methacrylate polymerization in nanoporous confinement" *Polymer* 2011;52:4093-4098.
24. Keddie JL, Jones RAL, Cory RA. "Interface and surface effects on the glass-transition temperature in thin polymer films" *Faraday Discussions* 1994;98:219-230.

25. Ouaad K, Djadoun S, Ferfera-Harrar H, Sbirrazzuoli N, Vincent L. "Synthesis and thermal behavior of poly(methyl methacrylate)/Maghnia bentonite nanocomposite prepared at room temperature via in situ polymerization initiated by a new Ni(II) α -benzoinoxime complex" *Journal of Applied Polymer Science* 2011;119:3227–3233.
26. Nishihara M, Teramoto K, Sakurai T, Takafuji M, Mashimo T, Ihara H. "Enhancement of isotacticity in bulk radical polymerization of poly (methyl methacrylate) under strong gravity field" *Polymer Journal* 2003;35:276-279.
27. Zhao HY, Yu ZN, Begum F, Hedden RC, Simon SL. "The effect of nanoconfinement on methyl methacrylate polymerization: T_g , molecular weight, and tacticity" *Polymer* 2014;55:4959-4965.
28. De Gennes PG. *Scaling Concepts in Polymer Physics*. Ithaca, NY: Cornell University Press; 1979.
29. Kong CY, Muthukumar MJ. "Polymer translocation through a nanopore. II. Excluded volume effect" *Journal of Chemical Physics* 2004;120:3460-3466.
30. Sakaue T, Raphael E. "Polymer chains in confined spaces and flow-injection problems: some remarks" *Macromolecules* 2006;39:2621-2628.
31. Cacciuto A, Luijten E. "Self-avoiding flexible polymers under spherical confinement" *Nano Letters* 2006;6:901–905.
32. Yang G, Bureau B, Rouxel T, Gueguen Y, Gulbitten O, Roiland C, Soignard E, Yarger JL, Troles J, Sangleboeuf JC, Lucas P. "Correlation between structure

and physical properties of chalcogenide glasses in the As_xSe_{1-x} system"

Physical Review B 2010;82:195206 (1-8).

33. Zhao HY, Koh YP, Pyda M, Sen S, Simon SL. "The kinetics of the glass transition and physical aging in germanium selenide glasses" Journal of Non-Crystalline Solids 2013;368:63-70.

CHAPTER 2

BACKGROUND

2.1 Kinetics of Free Radical Polymerization

Free radical polymerization is a chain addition reaction which includes four steps: initiation, propagation, termination and chain transfer. The kinetic mechanism of the initiation step is given by two elementary reactions [1]:

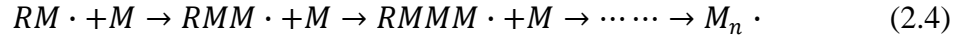


The initiator (I) can be decomposed by heat to form primary radicals ($R \cdot$) at a dissociation rate k_d , then the primary radical attaches to monomer (M) to form a monomer free radical species ($RM \cdot$) at an initiation rate k_i . Since the rate of forming the primary radical is much slower than the rate for forming the monomer radical [1], the initiation step is controlled by the slower reaction so that the initiation step rate (R_i) expression is described by the following equation:

$$R_i = 2fk_d[I] \quad (2.3)$$

where f is the initiation efficiency which is associated with the cage effect and $[I]$ is the concentration of initiator. The initial value of f is about 0.63 for methyl methacrylate (MMA) polymerization [1] and f decreases with the conversion increases and f drops to zero when vitrification occurs.

The chain propagation reaction is described by the successive addition of monomer to active chain end, and the elementary reaction is as following:



or in general,



where k_p is the rate constant for chain propagation, and $M_m \cdot$ and $M_{m+1} \cdot$ are the free radicals of chain lengths m and $m+1$, respectively. The rate expression for propagation (R_p) can be described by the following equation if we assume the propagation rate constant is independent of chain length:

$$R_p = k_p [M][M \cdot] \quad (2.6)$$

The termination reaction of MMA polymerization includes two type reactions: the combination termination and the disproportionation termination. The elementary reaction of combination termination can be expressed as the following:



The elementary reaction of disproportionation can be expressed as the following:



Thus, the rate reaction of termination (R_t) is described by the equation:

$$R_t = 2k_t [M \cdot]^2 \quad (2.9)$$

where k_t is the rate constant of termination reaction and every termination reaction terminates two free radicals so the coefficient of 2 is added in equation (2.9).

By combining equations (2.3), (2.6), (2.9) with the steady state approximation [1] that the rate of free radical initiation equals the rate of free radical termination ($R_i=R_t$), the rate reaction of propagation or polymerization (R_p) is expressed by the following equation:

$$R_p = k_p \left(\frac{fk_d}{k_t} \right)^{1/2} [I]^{1/2} [M] \quad (2.10)$$

This equation only describes the kinetically-controlled stage of the polymerization in which diffusion control is unimportant. The kinetic chain length (ν) is defined as the ratio of R_p to R_t expressed by the following equation:

$$\nu = \frac{R_p}{R_t} = \frac{k_p}{2(fk_d k_t)^{1/2}} \cdot \frac{[M]}{[I]^{1/2}} \quad (2.11)$$

which is directly related to number-average molecular weight (M_n) for free radical polymerization depending on the type of termination.

2.2 Autoacceleration Phenomenon (Gel Effect)

The autoacceleration effect (also known as Trommsdorff-Norrish effect) is regarded as the signature of bulk free radical polymerization. The occurrence of autoacceleration is attributed to a significantly increase in viscosity resulting in a reduction of the termination rate relative to the propagation rate. At low conversions, without autoacceleration, the conversion increases approximately linearly with increasing reaction time. However, as the extent of conversion increases, the higher viscosity of the mixture impedes the diffusion of free radicals while only slightly reducing chain propagating rate so that the ratio of $k_p/k_t^{1/2}$ is enhanced leading to a significant increase in conversion and molecular weight as equations (2.10) and (2.11) indicate.

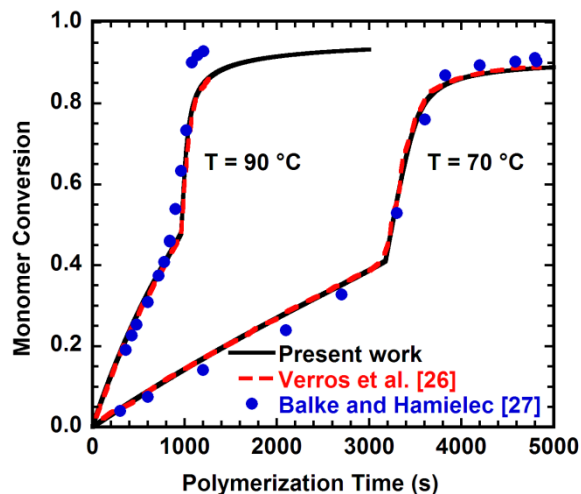


Figure 2.1. Comparison of conversion versus reaction time from literature [2].

Figure 2.1 is the comparison between experiments and modeling results from our laboratory [2], which shows the effects of autoacceleration on the reaction rate. The kinetically-controlled stage is observed at low conversion (50 % and 40 % for 70 and 90 °C, respectively) and this stage shifts to shorter polymerization time within increasing reaction temperature. The point where the slope abruptly changes for the conversion versus polymerization time data is defined as the onset of autoacceleration. Since the effects of autoacceleration are associated with propagation and termination reaction rate, the onset of autoacceleration also shifts to shorter time as reaction temperature increases. The solid lines are modifications of Verros's model [3] (dashed lines) that considers the diffusion effects, including those associated with initiation, propagation, and termination.

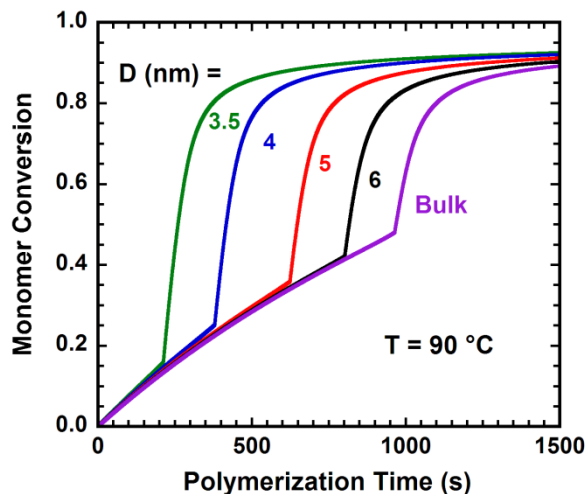


Figure 2.2. The evolution of conversion for bulk and nanoconfined at 90 °C [2].

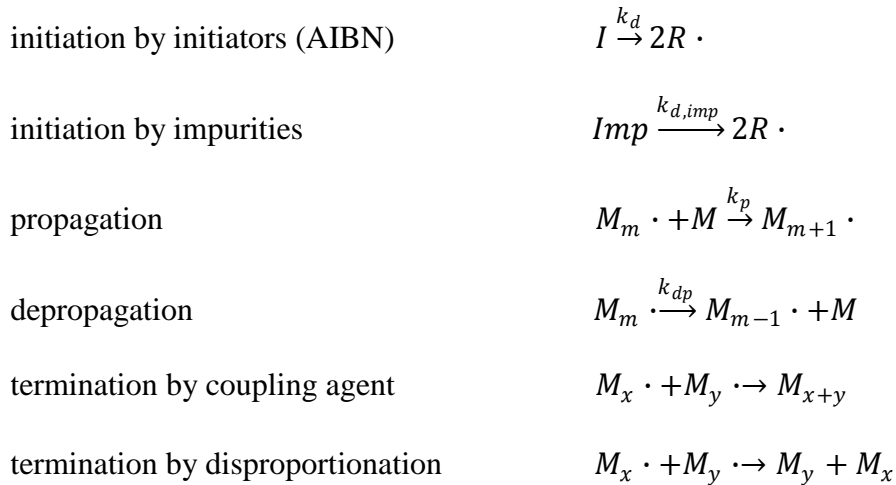
Begum extends the model [3] to incorporate the effect of nanoconfinement on diffusivity using the scaling of $D_{\text{conf}} = d^2 M^{-3}$ in literature [4,5]. The modified model can qualitatively predict the effects of nanoconfinement on MMA polymerization that autoacceleration shifts to shorter times as pore diameter decreases and the conversion to initiate the autoacceleration also decreases in the smaller pore size, as shown in Figure 2.2. Motivated by the model predictions, to quantify this increase in reactivity for MMA polymerization, we further performed experiments for MMA polymerized in CPG pores with different pore surface chemistries and successfully observed the expected enhancement in reaction kinetics. Then, Begum et al. [6,7] developed a simplified extension to the case of nanoconfinement using Doolittle free volume theory [8] which can quantitatively describe the increases in reaction kinetics of samples in hydrophobic and hydrophilic pores. This modified model also can qualitatively predict the evolution of molecular weight without adjustable parameters, as shown in Chapter 4.

2.3 High Temperature PMMA Polymerization

In MMA free radical polymerization at relatively low reaction temperatures, autoacceleration (gel effect) plays a crucial role resulting in diffusion controlled reaction at high conversions. Although the autoacceleration can expedite the polymerization, the large amount of heat accumulated in a very short time during this process may lead to many disadvantages, such as the reaction runaway or the low quality polymers with broad molecular weight distribution. For the practical application, especially in industrial reactor, solutions to reduce the difficulties raised from autoacceleration are suggested [9]. One way is to improve the heat transfer by decreasing the viscosity of monomer/polymer mixture, such as solution polymerization or suspension polymerization. An alternative method is to make the precursor of monomer/polymer mixture in bulk at very low conversion prior to the onset of autoacceleration and then transfer all the reactants in a specific condition that slowly polymerization can be achieved. [9] On the other hand, increasing the polymerization temperature above T_g of pure PMMA ($> 110\text{ }^\circ\text{C}$) seems a simple way to avoid the influence of gel effect because the polymerization process is performed in liquid phase such that heat is easily transferred by vigorously stirring. [9] However, considering the boiling temperature of MMA ($101\text{ }^\circ\text{C}$), the obstacle of this method is to adopt a pressurized reactor that decreases the vapor pressure of monomer to minimize the possible weight loss. Thus, some research groups [10-12] who investigated the PMMA polymerization at very high temperature have concluded that the classical kinetic models of PMMA polymerization at low temperatures are

insufficient since the influence of autoacceleration is obviously weakened at high temperature. A modified kinetics of PMMA polymerization at high temperature is taken into consideration.

Compared with the classical kinetics of PMMA polymerization, the high-temperature PMMA kinetics is modified by two additional steps. Firstly, impurities that takes part in the dissociation reaction becomes appreciable. At high temperature, peroxide-containing species generated from dissolved molecular oxygen may rapidly decompose to form the primary free radicals. [13,14] In addition to the effect of impurities, depolymerization dominates the propagation at high temperatures leading to the existence of a monomer/polymer equilibrium state. Therefore, the kinetics steps are modified [15] based on the classical kinetics mechanism:



where Imp, $k_{d,imp}$, and k_{dp} represents the impurities, the decomposition rate constant for impurities, and the depolymerization rate constant. For low temperature polymerization, the initiation step is slow so that the controlled step of the whole polymerization depends on the decomposition rate of initiators. However, high

temperature and rapidly decomposed impurities significantly enhance the initiation rate so that the controlled step of the whole polymerization is shifted to the equilibrium reaction between propagation and depropagation.

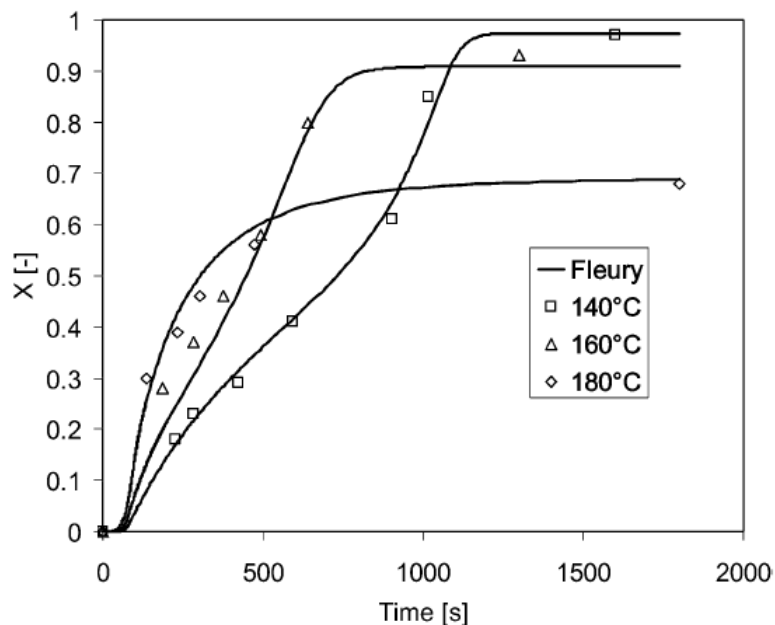


Figure 2.3. Monomer conversion as function of temperatures from literature [15].

Figure 2.3 shows the polymerization reaction of MMA initiated by 0.1 wt% di-*tert*-butyl peroxide (DTBP) at very high temperatures ranging from 140 to 180 °C. The symbols represent the experimental data obtained by DSC using medium-pressure steel pans. The solid lines are from modified Fleury model [10] which can reasonably fit the experimental results. It clearly shows that the effect of autoacceleration is attenuated with the reaction temperature increases; on the other hand, the final conversion is also reduced since the depolymerization becomes more appreciable as temperature increases.

2.4 Thermodynamics of Free Radical Polymerization

The thermodynamics of free radical polymerization can be described by the equation:

$$\Delta G_p = \Delta H_p - T \cdot \Delta S_p \quad (2.12)$$

where ΔG_p , ΔH_p , ΔS_p are the changes in Gibbs free energy, enthalpy, and entropy of the propagation reaction, respectively. For most vinyl monomer addition polymerizations, ΔH_p is negative since heat is released upon breaking the monomer π -bond and forming the polymer σ -bond, and ΔS_p is also negative due to the reduced degrees of freedom of the polymer compared to the monomer. Since the reaction spontaneously occurs when ΔG_p is negative, polymerization is favorable at low temperatures; however, ΔG_p becomes less negative as temperature increases and a polymer/monomer equilibrium exists at high temperatures. Above the ceiling temperature (T_c), ΔG_p will be positive such that monomer will not convert to polymer. One exception is the sulfur ring to chain polymerization, where both ΔH_p and ΔS_p are positive so that the opposite floor temperature (the lowest temperature for polymerization) rather than a ceiling temperature, is observed.

The equilibrium between polymer and monomer is described by the following equation [1]:



where $M_m \cdot$ is the free radical species of length m , M is the monomer, and K is the equilibrium constant defined as the ratio of the activities of the products to the reactants:

$$K = \frac{a_{M_{m+1}}}{a_{M_m} \cdot a_M} = \frac{1}{\phi_M} = \frac{1}{1-x} \quad (2.14)$$

where a_i is the activity of species i . The activities of the free radical species of length m and $m+1$ are the same, whereas the activity of the monomer is approximately equivalent to the volume fraction ϕ_M , which is the reciprocal of $1-x$, where x is the conversion of monomer. The equilibrium constant also depends on ΔG_p , temperature, and gas constant (R):

$$K = \exp(-\Delta G_p/RT) \quad (2.15)$$

Substituting equations (2.12) and (2.14) into equation (2.15) and rearranging, the relationship between conversion and the change in enthalpy or entropy is obtained:

$$\ln(1-x) = \frac{\Delta H_p}{RT} - \frac{\Delta S_p}{R} \quad (2.16)$$

At the ceiling temperature, ΔG_p is zero so that T_c is simply defined as the ratio of ΔH_p to ΔS_p :

$$T_c = \frac{\Delta H_p}{\Delta S_p} \quad (2.17)$$

2.5 Statistical Model for Stereoregular Chain Propagation

The stereoregular study of homopolymerized vinyl polymers is usually carried out using proton nuclear magnetic resonance (^1H NMR) experiments. For example, the tacticity of PMMA is measured by ^1H NMR focusing on the triads fractions [16-18], where the chemical shift window containing three peaks of α -methyl group ($\alpha\text{-CH}_3$) are assigned to isotactic (mm), syndiotactic (mr), and atactic triads (rr).

Stereospecific chain propagation is controlled by the last monomer unit of a polymer chain and is named chain end control. [1], such as shown in Figure 2.4.

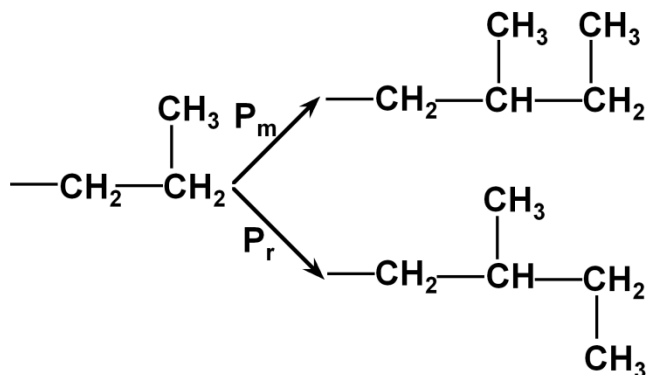


Figure 2.4. Schematic of vinyl monomer propagation by chain end effect. [1]

where P_m and P_r are conditional probabilities of forming isotactic or syndiotactic diads, respectively. Since the substituent group has to be either isotactic diad or syndiotactic diad, the percentage of mm, mr, and rr can be modeled by Bernoullian model and is calculated by the following equations:

$$mm = P_m^2 \quad (2.18)$$

$$mr = 2P_m P_r = 2P_m (1 - P_m) \quad (2.19)$$

$$rr = P_r^2 = (1 - P_m)^2 \quad (2.20)$$

For the Bernoullian model, only the last monomer unit affects the stereochemistry of the chain propagation and the other monomer units exert no influence on stereoregular addition [19] leading to the relationship of $P_m + P_r = 1.0$. Thus, the data of mm, mr, and rr triads provided by the NMR experiments can be converted to P_m and P_r and compare with the equation described by literature [20] ($mr/rr = 2P_m/(1-P_m)$) to verify the chain end control scenario.

On the other hand, unlike the polymer chain end control, penultimate unit control occurs when the monomer unit prior to the last monomer unit influence stereospecific chain propagation. [1] A schematic is shown in Figure 2.5:

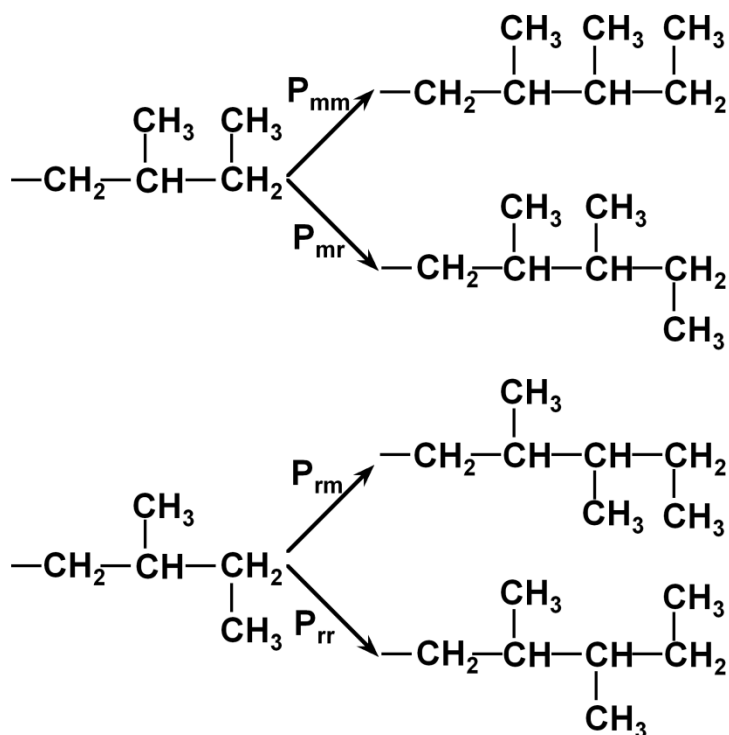


Figure 2.5. Schematic of vinyl monomer propagation by penultimate effect. [1]

where P_{mr} is the probability that a syndiotactic diad will be formed after an isotactic diad, and P_{mm} is the similar definition and equals $(1 - P_{mr})$; P_{rm} is the probability that an isotactic diad will be formed after a syndiotactic diad, and P_{rr} is the similar definition and equals $(1 - P_{rm})$. Thus, the percentage of mm, mr, and rr triads are calculated by equations:

$$mm = \frac{(1 - P_{mr})P_{rm}}{(P_{mr} + P_{rm})} \quad (2.21)$$

$$mr = \frac{2P_{mr}P_{rm}}{(P_{mr} + P_{rm})} \quad (2.22)$$

$$rr = \frac{(1-P_{rm})P_{mr}}{(P_{mr} + P_{rm})} \quad (2.23)$$

If penultimate effects dominates the stereospecific chain addition [19,21], the first-order Markov model is able to fit the data of triads. In this case, the percentage of triads data obtained from NMR experiments can provide the information of the four conditional probabilities P_{mm} , P_{mr} , P_{rm} , and P_{rr} as the following equations:

$$P_{mr} = \frac{mr}{(2mm + mr)} \quad (2.24)$$

$$P_{rm} = \frac{mr}{(2rr + mr)} \quad (2.25)$$

If the sum of P_{mr} and P_{rm} equals 1.0 then the stereospecific propagation obeys the Bernoullian Model. In general, PMMA polymerized at lower temperature with higher syndiotactic triads tends to be the Bernoullian fits but the tendency could shift to first-order Markov fits when the reaction temperature is higher or the isotactic triads become higher [22].

2.6 Structural Recovery (Physical Aging Process)

Glass-forming materials are liquids or rubber at high temperature. As the materials are cooled, enthalpy (H) or volume (V) decrease, and the mobility also gradually decreases; below T_g , the materials can no longer maintain equilibrium and deviate from the equilibrium line. [23] Therefore, the glassy state for materials is a non-equilibrium state so that both H or V spontaneously tend to evolve toward the equilibrium liquid line if the material is held isothermally in the glassy state. The

phenomenon that non-equilibrium glasses tend to recover to their equilibrium state is called structural recovery. [23] Structural recovery is also sometimes called physical aging; however, physical aging is also used to describe only the changes in mechanical properties that accompanies structure recovery. [23] For clarity, in this dissertation, the term "physical aging" is equivalent to the term "structural recovery".

A schematic of the evolution of enthalpy is shown in Figure 2.6. A schematic of volume versus temperature is similar with Figure 2.6. The enthalpy loss on aging (ΔH_a) increases with increasing aging time and finally the enthalpy loss stops evolving resulting in maximum value of enthalpy loss defined as equilibrium change in enthalpy ($\Delta H_{a\infty}$). The difference between $\Delta H_{a\infty}$ and ΔH_a ($\Delta H_{a\infty} - \Delta H_a$) reflects the distance from the equilibrium state. This distance from the equilibrium state is also quantified by the fictive temperature (T_f), introduced by Tool [24]. T_f is defined as the intersection between the extrapolated glass and liquid lines. In the schematic, T_f decreases with increasing aging time from an initial value of T_g . If the materials reach the equilibrium state, the value of T_f can theoretically decrease to the aging temperature (T_a).

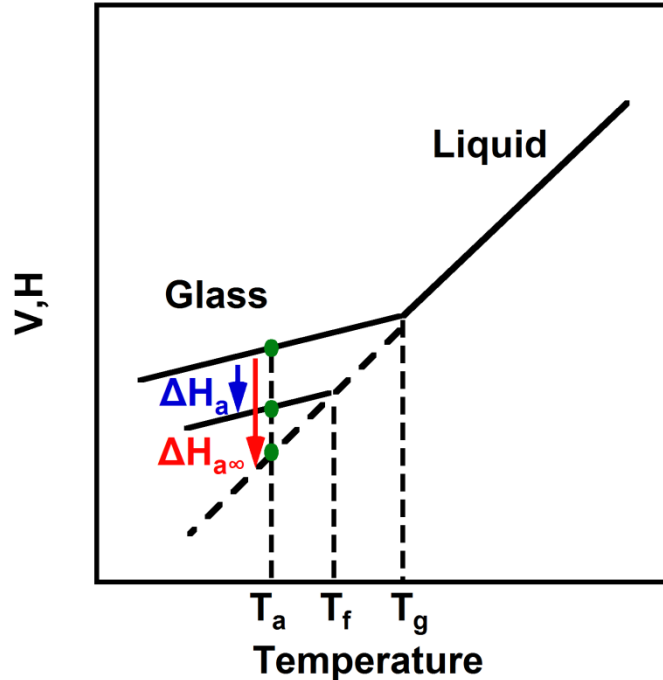


Figure 2.6. Schematic of the evolution of volume or enthalpy on physical aging.

2.7 Intermediate Phase of Chalcogenide Glasses

The intermediate phase was first proposed by Thorpe et al. [25] as a phase in which the stress induced during glass formation is minimized resulting in an stress-free rigid state. Moreover, Micoulaut and Phillips [26,27] further showed that the stress-free state may be achieved by increased local ordering or cluster formation in a binary chalcogenide glasses. The proposed intermediate phase comprises a relatively narrow composition range in the vicinity of mean coordination number (r_c) equals 2.4, although the transition range for real systems shows deviations from $r_c = 2.4$ due to the presence of terminal or dangling bonds [28], expanded valence shells [29,30], long-range forces associated with non-bonding lone electron pairs [31], and breaking of bond-bending constraints [32].

The interesting feature of the intermediate phase is that the non-reversing heat flow is absent in TMDSC measurements indicating no significant relaxation in the glassy state prior to the heating scan. The intermediate phase is important because, if it exists, remarkable properties may be achieved, including a stable non-aging [33], stress-free state [34], and an isotactically rigid local structure [35-37].

The absence of enthalpy changes during aging or non-reversing heat flow is the recognized criterion for the existence of the intermediate phase [38-41]. Referring to Figure 2.6, this could only occur if the liquid and glass states are similar such that the physical aging cannot occur. Although the existence of intermediate phase has been theoretically justified by the ability of the system to self organize to minimize the stress [28,31], the interpretation of the non-reversing heat flow obtained by TMDSC to define the boundaries of the intermediate phase has been criticized due to a lack of longer time aged samples [28]. The comparison between literature and our observations has been explicitly investigated in Chapter 6. Therefore, in Chapter 6, we examine enthalpy recovery for various compositions of Ge-Se glasses to investigate the existence of the proposed intermediate phase.

References

1. Odian G. Principles of Polymerization. 3rd ed. New York: Wiley; 2004.
2. Begum F, Simon SL. "Modeling methyl methacrylate free radical polymerization in nanoporous confinement" *Polymer* 2011;52:1539-1545.
3. Verros GD, Latsos T, Achilias DS. "Development of a unified framework for calculating molecular weight distribution in diffusion controlled free radical bulk homo-polymerization" *Polymer* 2005;46:539-552.
4. Begum F, Zhao HY, Simon SL. "Modeling methyl methacrylate free radical polymerization: Reaction in hydrophilic nanopores" *Polymer* 2012;53:3238-3244.
5. Begum F, Zhao HY, Simon SL. "Modeling methyl methacrylate free radical polymerization: Reaction in hydrophobic nanopores" *Polymer* 2012;53:3261-3268.
6. Cui T, Ding J, Chen JZY. "Dynamics of a self-avoiding polymer chain in slit, tube, and cube confinements" *Physical Review E* 2008;78:061802(1-7).
7. Avramova K, Milchev A. "Polymer chains in a soft nanotube: A Monte Carlo Study" *Journal of Chemical Physics* 2006;124:024909(1-8).
8. Doolittle AK. "Studies in Newtonian Flow. II. The dependence of the viscosity of liquids on free-space" *Journal of Applied Physics* 1951;22:1471-1475.
9. Fenouillot F, Terrisse J, Rimlinger T. "Experimental study and simulation of the polymerization of methyl methacrylate at high temperature in a continuous reactor" *Journal of Applied Polymer Science* 2001;79:2038-2051.

10. Fleury PA, Meyer T, Renken A. "Solution polymerization of methyl-methacrylate at high conversion in a recycle tubular reactor" *Chemical Engineering Science* 1992;47:2597-2602.
11. Fenouillot F, Terrisse J, Rimlinger T. "Polymerization of methyl methacrylate at high temperature with 1-butanethiol as chain transfer agent" *Journal of Applied Polymer Science* 1999;72:1589-1599.
12. Fenouillot F, Terrisse J, Rimlinger T. "Thermal polymerization of methyl methacrylate at high temperature" *International Polymer Processing* 1998;13:154-161.
13. Lehrle RS, Shortland A. "A study of the purification of methyl methacrylate suggests that the "thermal" polymerisation of this monomer is initiated by adventitious peroxides" *European Polymer Journal* 1988;24:425-429.
14. Bamford CH, Morris PR. "The oxidative polymerization of methyl methacrylate" *Die Makromolekulare Chemie* 1965;87:73-89.
15. Nising P, Meyer T. "Thermal initiation of MMA in high temperature radical polymerizations" *Industrial and Engineering Chemistry Research* 2004;43:7220-7226.
16. Bovey FA, Tiers GVD. "Polymer NSR spectroscopy. II. The high resolution spectra of methyl methacrylate polymers prepared with free radical and anionic initiators" *Journal of Polymer Science* 1960;44:173-182.

17. Fordham JWL, Burleigh PH, Sturm CL. "Stereoregulated polymerization in the free propagating species. III. Effect of temperature on the polymerization of vinyl chloride" *Journal of Polymer Science* 1959;41:73-82.
18. Bovey FA. "Polymer NSR spectroscopy. III. The rates of the propagation steps in the isotactic and syndiotactic polymerization of methyl methacrylate" *Journal of Polymer Science* 1960;46:59-64.
19. Price FP. "Copolymerization mathematics and the description of stereoregular polymers" *Journal of Chemical Physics* 1962;36:209-218.
20. Fox TG, Schnecko HW. "The effect of temperature, conversion and solvent on the stereospecificity of the free radical polymerization of methyl methacrylate" *Polymer* 1962;3:575-584.
21. Bovey FA. "The stereochemical configuration of vinyl polymers and its observation by nuclear magnetic resonance" *Accounts of Chemical Research* 1968;1:175-185.
22. Uemura T, Ono Y, Hijikata Y, Kitagawa S. "Functionalization of coordination nanochannels for controlling tacticity in radical vinyl polymerization" *Journal of the American Chemical Society* 2010;132:4917-4924.
23. McKenna GB, Simon SL, In: Cheng SZD editor. *Handbook of Thermal Analysis and Calorimetry, Applications to Polymers and Plastics Vol.3*. Elsevier Science; 2002.

24. Tool AQ. "Effect of heat-treatment on the density and constitution of high-silica glasses of the borosilicate type" *Journal of the American Ceramic Society* 1948;31:177-186.
25. Thorpe MF, Jacobs DJ, Chubynsky MV, Phillips JC. "Self-organization in Network Glasses" *Journal of Non-Crystalline Solids* 2000;266-269:859-866.
26. Micoulaut M. "Rigidity transitions and constraint counting in amorphous networks: Beyond the mean-field approach" *Europhysics Letters* 2002;58:830-836.
27. Micoulaut M, Phillips JC. "Rings and rigidity transitions in network glasses" *Physical Review B* 2003;67:104204(1-29).
28. Shpotyuk O, Hyla M, Boyko V, Golovchak R. "Reversibility windows in selenide-based chalcogenide glasses" *Physica B: Condensed Matter* 2008;403:3830-3837.
29. Caprion D, Schober HR. "Structure and relaxation in liquid and amorphous selenium" *Physical Review B* 2000;62:3709-3716.
30. Hohl D, Jones RO. "First-principles molecular-dynamics simulation of liquid and amorphous selenium" *Physical Review B* 1991;43:3856-3870.
31. Lucovsky G, Phillips JC. "Intermediate phases in binary and ternary alloys: a new perspective on semi-empirical bond constraint theory" *Journal of Physics: Condensed Matter* 2007;19:455218(1-20).

32. Golovchak R, Kozdras A, Shpotyuk O, Kozyukhin S, Saiter JM. "Long-term ageing behaviour in Ge–Se glasses" *Journal of Materials Science* 2009;44:3962–3967.
33. Chakravarty S, Georgiev DG, Boolchand P, Micoulaut M. "Ageing, fragility and the reversibility window in bulk alloy glasses" *Journal of Physics: Condensed Matter* 2005;17:L1-L7.
34. Wang F, Mamedov S, Boolchand P, Goodman B, Chandrasekhar M. "Pressure Raman effects and internal stress in network glasses" *Physical Review B* 2005;71:174201(1-22).
35. Feng XW, Bresser WJ, Boolchand P. "Direct evidence for stiffness threshold in Chalcogenide glasses" *Physical Review Letters* 1997;78:4422-4425.
36. Selvanathan D, Bresser WJ, Boolchand P. "Stiffness transitions in $\text{Si}_x\text{Se}_{1-x}$ glasses from Raman scattering and temperature-modulated differential scanning calorimetry" *Physical Review B* 2000;61:15061-15076.
37. Georgiev DG, Boolchand P, Micoulaut M. "Rigidity transitions and molecular structure of $\text{As}_x\text{Se}_{1-x}$ glasses" *Physical Review B* 2000;62:R9228-R9231.
38. Chen P, Boolchand P, Georgiev DG. "Long term aging of selenide glasses: evidence of sub- T_g endotherms and pre- T_g exotherms" *Journal of Physics: Condensed Matter* 2010;22:065104(1-16).
39. Madhu BJ, Jayanna HS, Asokan S. "Evidence of an intermediate phase in ternary $\text{Ge}_7\text{Se}_{93-x}\text{Sb}_x$ glasses" *European Physical Journal B* 2009;71:21-25.

40. Pattanayak P, Asokan S. "A sharp thermally reversing window in $\text{As}_{45}\text{Te}_{55-x}\text{I}_x$ chalcogenide glasses revealed by alternating differential scanning calorimetry and photo thermal deflection studies" *Journal of Non-Crystalline Solids* 2008;354:3824-3827.
41. Anbarasu M, Singh KK, Asokan S. "Evidence for a thermally reversing window in bulk Ge–Te–Si glasses revealed by alternating differential scanning calorimetry" *Philosophical Magazine* 2008;88:599-605.

CHAPTER 3

METHYL METHACRYLATE POLYMERIZATION IN NANOPOROUS CONFINEMENT

3.1 Introduction

Nanoconfinement is known to influence the reaction kinetics and polymerization products in free radical and step polymerizations. For free radical polymerizations, significant increases in molecular weight and decreases in PDI are generally observed. [1-8] For example, M_n increases from 3.6×10^4 g/mol to 3.6×10^5 g/mol for polymerization of MMA in the 2.7 nm-diameter pores of zeolite MCM-41 and PDI decreases from 2.8 to 1.7 [1]; in that work, the zeolite did not serve any catalytic role but was only used for nanoconfinement. Similar results were obtained for PMMA synthesized in gel silica glass having 4.4 nm pores and for various vinyl polymers formed in the small nanochannels of porous coordination polymers (PCP), [2,3] although disparate results have also been observed [9]. In addition to changes in molecular weight and PDI, increases in the degree of tacticity have been observed for nanoconfined styrene, methyl methacrylate, and vinyl acetate free radical polymerizations, and a decrease in the branching and an increase in the number of linear chains were also observed for nanoconfined poly(vinyl acetate) polymerization. [3] Decreased yields observed for various vinyl polymers in the smallest PCP nanochannels were attributed to a decrease in initiator efficiency. [3] Based on the work reported in the literature, nanoconfinement has the ability to not only influence molecular weights, but also to affect polymer configuration and yields in free radical

polymerizations.

The results can generally be explained by a decrease in the rate of termination due to a decrease in chain diffusivity upon nanoconfinement, consistent with literature showing reduction of polymer chain diffusivity upon nanoconfinement, at least in the direction perpendicular to cylindrical pore walls [10] and near rough walls [11,12]. Recent Monte Carlo studies also indicate that chain diffusivity scales with inverse molecular weight to the third power and confinement size to the second power in theta conditions.[13,14] Hence, chain diffusion is anticipated to slow dramatically upon nanoconfinement, whereas monomer diffusion does not, and as a result, the Tromsdorff or gel effect, also known as autoacceleration, is anticipated to occur much earlier in nanoconfined free radical polymerizations. Such an effect was demonstrated in our recent modeling work [15] in which the kinetic model of Verros et al. [16] for MMA polymerization was extended to account for changes in diffusivity upon nanoconfinement. Although limited conversion versus time curves were shown in the work on free radical polymerizations in PCP [3], to the best of our knowledge, the effect of nanoconfinement on the rate of free radical polymerization has not been experimentally quantified.

For step polymerizations, on the other hand, nanoconfinement has been found to accelerate the trimerization reaction of dicyanate esters to form polycyanurates, [17-19] as well as the polymerization of phenolic resins. [20] The nanoconfinement also affects the transition of sulfur living polymerization. [21] Monte Carlo simulations of a linear homopolymerization indicate that either an increase or decrease in reactivity

might be expected in nanoconfined step growth reactions due to the competition between reduced diffusivity of functional groups and enhanced local concentrations arising from layering next to the confinement surface. [22] On the other hand, molecular dynamics simulations show slower reactivity of functional groups near the wall coupled with similar reaction rates in the core of a pore. [23]

Here, our focus is on the rate of isothermal free radical polymerization of MMA inside nanopores using differential scanning calorimetry. We can observe where confinement effects become important for the MMA reaction kinetics by using CPG as the confinement matrix because it is available in a broad range of sizes from 13 to 110 nm. We examine the influence of pore surface chemistry on the reaction rate, activation energy, and the point at which autoacceleration occurs. The results are discussed in the context of the current literature.

3.2 Methodology

3.2.1 Materials

MMA monomer and AIBN initiator were obtained from Aldrich. The MMA was purified by passing it through a disposable prepacked column (Aldrich, No. 306312) at least three times to remove hydroquinone. The monomer was mixed with 0.5 wt % AIBN and then degassed for 10 minutes at room temperature under vacuum. If not used immediately, the solution of monomer and initiator was stored in a freezer at -20 °C. No change in the heat of reaction was found as a function of time in freezer indicating that minimal reaction (< 1%) occurred during storage.

Controlled pore glasses (CPG, Millipore) with pore diameters (D) of 13, 50, and 110 nm were used as the confinement system. The CPG is composed of nanoporous borosilicate particles and has been shown to be stable with respect of organic liquids [18, 24]. Particles have a mesh size of 120/200 μm with a bulk density of 300 g/L, as provided by the manufacturer. Specific pore volume and surface area are also provided by manufacturer, as shown in Table 3.1.

In this work, both native hydrophilic and hydrophobic pore surfaces are employed. Hydrophobic surfaces were obtained by replacing the native hydroxyl groups of the CPG with trimethylsilyl groups using hexamethyldisilazane following the procedure of Jackson and McKenna [25]. The silanization does not significantly change the pore diameter or diameter distribution [26]. All CPGs were cleaned with nitric acid at 120 $^{\circ}\text{C}$ for 10 h prior to silanization, or prior to use in the unsilanized case, and then rinsed with reverse osmosis water four to five times and dried under vacuum at 280 $^{\circ}\text{C}$ for 24 h. CPGs are stored over desiccant after cleaning and/or silanization.

3.2.2 DSC Measurements

A Mettler-Toledo differential scanning calorimeter DSC823e was used with a Julabo FT100 intracooler and nitrogen purge gas. Samples were prepared in 20 μL hermetic pans under a nitrogen blanket. First, 2 to 6 mg of CPG was put on the bottom of the pan and a prespecified quantity of monomer/initiator solution was placed on top using a syringe. The pore fullness ranged from 70 % to 90 % based on the ratio of the monomer volume added to the pore volume. Imbibement occurs in

seconds due to the capillary forces. The MMA monomer was completely imbibed in the nanopores based on inspection of multiple samples for both pore surface conditions. After DSC runs, the pans were reweighed to check for weight loss; 85 % of samples showed weight loss less than 5 % and the remainder showed losses up to 10 %.

The polymerization of MMA in bulk and in nanoporous confinement was carried out isothermally in the DSC at four temperatures, 60, 70, 80 and 95 °C. After the isothermal reaction, a dynamic scan from room temperature to 180 °C was used to measure any residual heat of reaction. Two to three replicate samples were used for each reaction condition. Heat flow (\dot{Q}) during isothermal reaction is related to the conversion of MMA (x):

$$x = \frac{1}{\Delta H_T} \int_{t_0}^t \dot{Q} dt \quad (3.1)$$

where the total heat of reaction ΔH_T is obtained from the heat evolved isothermally plus the residual heat from the dynamic scan. The heats of reaction are independent of confinement size and are the same as the bulk within the error of the measurements, as shown in Table 3.2. The average total heat of reaction for all samples is 545 ± 29 J/g, in good agreement with the value of 560 J/g reported in the literature [27].

Indium was used to calibrate the enthalpy and temperature at 10 K/min. For the isothermal condition, an isothermal calibration [28] was performed using indium at 0.1 K/min.

3.3 Results

Heat flow during isothermal polymerization is plotted versus time after induction of the reaction for representative bulk unconfined samples in Figure 3.1. As expected, the reaction rate is higher at higher temperatures as indicated by the larger initial heat flow. The Tromsdorff effect or autoacceleration is observed as the exothermic peak in the isothermal heat flow curves. The exothermic peaks shift to shorter times with increasing reaction temperature indicating that the time required to reach the onset of autoacceleration decreases as reaction temperature increases.

The heat flow for the bulk reaction at 80 °C is compared with representative results for samples confined in hydrophobic silanized pores in Figure 3.2a. Although the shapes of the exothermic peaks are similar, the exotherms shift to shorter times as pore size decreases indicating that the onset of autoacceleration occurs earlier in smaller pores. In hydrophilic pores, the effect of nanoconfinement on autoacceleration is more pronounced, as shown in Figure 3.2b. In addition, the initial rate of reaction increases with decreasing pore size in the hydrophilic pores, as indicated by the larger initial heat flow in the smaller pores.

The results shown in Figures 3.1 and 3.2ab are shown as a function of the time of reaction after induction. Both bulk and nanoconfined samples exhibit an induction time which decreases with increasing temperature as shown in Figure 3.3. The induction time becomes more significant at lower temperatures presumably due to the presence of residual hydroquinone or adventitious oxygen coupled with lower reaction rates. Within the scatter of the data, there is no significant change in induction time

upon nanoconfinement, with the exception of a slight increase for reaction in 13 nm diameter hydrophilic pores. The temperature dependence of the induction time is also the same for bulk and nanoconfined samples within the error of the measurements indicating that the activation energy for initiator dissociation is not influenced by nanoconfinement.

The isothermal heat flow data is converted to conversion versus time data using equation (3.1). Representative conversion versus time curves are shown for the reaction at 80 °C in Figures 3.4a and 3.4b for nanoconfined samples in hydrophobic and hydrophilic pores, respectively. A representative bulk curve is also shown in both figures for comparison. As expected for first-order reaction kinetics, conversion increases approximately linearly at low conversions. For hydrophobic pores (Figure 3.4a), the initial reaction rate is not a strong function of pore size, whereas in hydrophilic pores (Figure 3.4b), the initial slope of the conversion versus time curve increases as pore size decreases. After the initial portion of the curve, the reaction rate increases rapidly due to autoacceleration. In addition to autoacceleration occurring at earlier times in smaller pores, from these figures, it is also clear that the conversion required to reach autoacceleration decreases as pore size decreases. Similar behavior is observed for the other reaction temperatures.

An effective rate constant can be obtained from the conversion versus time data at low conversions prior to autoacceleration assuming a first order reaction model:

$$-\ln(1 - x) = k_{\text{eff}}t \quad (3.2)$$

where the effective rate constant, k_{eff} , is related to the individual rate constants and the initiator concentration [27]:

$$k_{\text{eff}} = k_p \left(\frac{fk_d}{k_t} [I]_o \right)^{\frac{1}{2}} \quad (3.3)$$

Where k_p , k_d , and k_t are the rate constants for propagation, initiator decomposition, and termination, respectively, f is the initiator efficiency, and $[I]_o$ is the initial concentration of initiator. This simplified reaction model is valid at low conversions when diffusion effects are not prevalent and when the initiator concentration has not substantially decreased from its initial value. The model fits both the bulk and nanoconfined data well from 2 to 20 % conversion. The results are shown in Figure 3.5 where the ratio of the effective rate constant for the nanoconfined reaction to that for the bulk reaction ($k_{\text{nano}}/k_{\text{bulk}}$) is plotted as a function of reciprocal pore size for the various reaction temperatures investigated. The effective rate constant for reaction in hydrophobic pores is unchanged from the bulk such that the normalized rate constant ($k_{\text{nano}}/k_{\text{bulk}}$) is 1.0 ± 0.1 , independent of pore size. On the other hand, in hydrophilic pores, the effective rate constant increases by a factor of 4 in 13 nm-diameter pores at 95 °C and by a factor of 8 at 60 °C.

The natural logarithm of the effective reaction rate constant is plotted versus reciprocal absolute temperature in Figure 3.6 indicating an Arrhenius temperature dependence:

$$k_{\text{eff}} = Ae^{(-E_{\text{app}}/RT)} \quad (3.4)$$

where A is the Arrhenius prefactor and E_{app} is the apparent activation energy. An apparent activation energy of 78 kJ/mol is obtained from the bulk data, consistent with literature reports ranging from 78 to 86 kJ/mol [27, 29-32]. No significant difference in activation energy is observed between the bulk reaction and nanoconfined reactions in hydrophobic pores. On the other hand, for samples reacting in hydrophilic 13 nm diameter pores, the apparent activation energy is 58 ± 5 kJ/mol, a 25% reduction compared to the bulk value; a student t-test indicates that the reduction is statistically significant. Reductions in the apparent activation energy from the bulk value are also observed for the reactions in larger hydrophilic pores, but these values do not statistically differ from the bulk value.

Autoacceleration is important in MMA free radical reaction since both the reactivity and molecular weight increase at this point in the reaction. As already discussed, autoacceleration occurs at earlier times and conversions with decreasing pore size. We quantify this effect by plotting the ratio of the time required to reach autoacceleration for nanoconfined and bulk samples in Figure 3.7. The time required to reach autoacceleration decreases with increasing temperature and decreasing pore size, especially in hydrophilic pores. In 13 nm-diameter hydrophobic pores, the onset of autoacceleration occurs at approximately 60 to 70 % of the time required for the bulk reaction. On the other hand, in 13 nm-diameter hydrophilic pores, the onset of autoacceleration occurs much earlier, at approximately 10 to 20 % of the time required for the bulk reaction.

3.4 Discussion

The initial rate of MMA polymerization in hydrophobic pores is the same as that in the bulk within the error of the measurements. In addition, the limiting conversion or polymer yield is not found to be a strong function of pore size, as shown in Figure 3.2a. Hence, the initiator efficiency f is not considered to be significantly influenced by nanoconfinement in our system. This differs from the results in the literature for confinement of several vinyl monomers in porous coordination polymers (PCP), where limiting conversions dropped dramatically upon nanoconfinement [3]. The difference may be attributed to the range of pore sizes investigated. In PCP, pore sizes ranged from 0.4 to 1 nm, significantly smaller than the smallest pores examined in this work.

In contrast to the unchanged reaction rate in hydrophobic pores prior to autoacceleration, for the reaction in hydrophilic pores, the reaction rate at low conversions is enhanced by as much as a factor of eight in 13 nm-diameter pores at 60 °C. The explanation for the obviously enhanced reactivity in native CPGs with decreasing pore size may lie in the influence of the native hydroxyl groups on the CPG surface. In the work of O'Driscoll and coworkers, an increase in the effective rate constant for MMA polymerization was observed with increasing concentration of benzyl alcohol solvent, and this was attributed to stabilization of the MMA monomer by complexation by solvent. [33,34] However, in addition to increasing the effective rate constant in that work, increasing benzyl alcohol content also resulted in an increase in the apparent activation energy. [34] In the present work, we observe that

the effective rate constant increases approximately linearly with reciprocal pore diameter in hydrophilic pores. Hence, the increase is approximately linearly related to the ratio of the surface area to internal volume of the pores, consistent with the increase being due to the hydroxyl groups on the CPG surface. However, we also observe a decrease in the apparent activation energy which is not consistent with O'Driscoll's observations for the effects of benzyl alcohol. Recent work by Lutkenhaus and coworkers, however, found both an increase in the amidation reaction rate and a concomitant decrease in the activation energy with decreasing film thickness for reactive layer-by-layer polymer assemblies on both alumina and native silicon substrates; replacement of the hydroxyl groups using hexamethyldisilazane resulted in reactivities and activation energies similar to those of thicker films indicating that catalysis by the surface hydroxyl groups was primarily responsible for the nanoconfinement effect. [35] Although the changes of activation energy in previous work are not consistent, the catalytic effects of hydroxyl groups were explicitly confirmed just as explanation on the results of our hydrophilic porous system.

In addition to the enhanced initial reaction rate in hydrophilic pores, the onset of autoacceleration occurs earlier in both types of nanopores, with even earlier onset in the hydrophilic pores. The onset of autoacceleration is known to be due to the suppression of the termination reaction as molecular weight increases and chain diffusivity decreases with increasing conversion. The decrease in the time required to reach autoacceleration for the nanoconfined reaction relative to the bulk reaction

provides evidence that chain diffusivity decreases under nanoconfinement. In recent modeling work from our laboratory [15], we extended the MMA polymerization model of Verros et al. [16] to account for changes in diffusivity upon nanoconfinement and found qualitatively similar results as are experimentally observed in this work. The fact that the timescale to reach autoacceleration is shorter in the hydrophilic pores is consistent with the faster initial reaction rate in those pores such that changes in diffusivity also occur at earlier times.

To quantitatively model the experimental data shown in this chapter, we modified the previous kinetic model of nanoconfined MMA polymerization [15] to combine with the diffusion-controlled phenomenon based on the Doolittle free volume theory [36]. The simplified model is able to capture the conversion as a function of temperature for MMA polymerization in different CPG pore diameter environment, where the reduced onset of autoacceleration in nanopores and the significantly enhanced initial reaction rate for samples in hydrophilic pores are both quantitatively described by the model. Future work will attempt to extend the model to show the changes in molecular weights in CPG system without adjustable parameters.

3.5 Conclusions

The effect of nanoconfinement on methyl methacrylate (MMA) polymerized in the nanopores of controlled pore glass (CPG) has been investigated for both hydrophobic and hydrophilic pores. The initial rate of reaction prior to autoacceleration is similar for the bulk reaction and for reaction in hydrophobic pores, but the initial rate is considerably faster in hydrophilic pores and increases

approximately linearly with reciprocal pore size. The apparent activation energy of the initial reaction shows no statistical difference from bulk values, except for the reaction in hydrophilic 13 nm-diameter pores which shows a 25% reduction in apparent activation energy. The time required to reach autoacceleration (the Tromsdorff effect) decreases with decreasing pore size in both types of pores, but the effect is more dramatic for the reaction in hydrophilic pores. The decreasing time to reach autoacceleration is presumed to be due to the decrease in the diffusivity of long chains under nanoconfinement which results in a decrease in the rate of termination of free radicals. These results are qualitatively consistent with recent modeling results.

References

1. Ng SM, Ogino S, Aida T, Koyano KA, Tatsumi T. "Free radical polymerization within mesoporous zeolite channels" *Macromolecular Rapid Communications* 1997;18:991-996.
2. Li XC, King TA, Pallikari-Viras F. "Characteristics of composites based of PMMA modified gel silica glasses" *Journal of Non-Crystalline Solids* 1994;170:243-249.
3. Uemura T, Ono Y, Kitagawa K, Kitagawa S. "Radical polymerization of vinyl monomers in porous coordination polymers: Nanochannel size effects on reactivity, molecular weight, and stereostructure" *Macromolecules* 2008;41:87-94.
4. Kageyama K, Ng SM, Ichikawa H, Aida T. "Macromolecular synthesis using mesoporous zeolites" *Macromolecular Symposia* 2000;157:137-142.
5. Kalogeras IM, Neagu ER. "Interplay of surface and confinement effects on the molecular relaxation dynamics of nanoconfined poly(methyl methacrylate) chains" *European Physical Journal E* 2004;14:193-204.
6. Ni XF, Shen ZQ, Yasuda H. "Polymerization of methyl methacrylate with samarocene complex supported on mesoporous silica" *Chinese Chemical Letters* 2001;12:821-822.
7. Ikeda K, Kida M, Endo K. "Polymerization of methyl methacrylate with radical initiator immobilized on the inside wall of mesoporous silica" *Polymer Journal* 2009;41:672-678.

8. Kalogeras IM, Vassilikou-Dova A. "Dielectric probe of intermolecular interactions in poly (methyl methacrylate)(PMMA) and PMMA+ SiO₂ matrixes doped with luminescent organics" *Journal of Physical Chemistry B* 2001;105:7651-7662.
9. Pallikari-Viras F, Li XC, King TA. "Thermal Analysis of PMMA/gel Silica Glass Composites" *Journal of Sol-Gel Science and Technology* 1996;7:203-209.
10. Baschnagel J, Binder K. "Dynamics of glassy polymer melts in confined geometry: A Monte Carlo simulation" *Journal de Physique I* 1996;6:1271-1294.
11. Scheidler P, Kob W, Binder K. "The relaxation dynamics of a confined glassy simple liquid" *European Physical Journal E* 2003;12:5-9.
12. Teboul V, Simionesco CA. "Properties of a confined molecular glass-forming liquid" *Journal of Physics: Condensed Matter* 2002;14:5699-5709.
13. Avramova K, Milchev A. "Polymer chains in a soft nanotube: A Monte Carlo Study" *Journal of Chemical Physics* 2006;124:024909(1-8).
14. Cui T, Ding J, Chen JZY. "Dynamics of a self-avoiding polymer chain in slit, tube, and cube confinements" *Physical Review E* 2008;78:061802(1-7).
15. Begum F, Simon SL. "Modeling methyl methacrylate free radical polymerization in nanoporous confinement" *Polymer* 2011;52:1539-1545.

16. Verros GD, Latsos T, Achilias DS. "Development of a unified framework for calculating molecular weight distribution in diffusion controlled free radical bulk homo-polymerization" *Polymer* 2005;46:539-552.
17. Li QX, Simon SL. "Curing of bisphenol M dicyanate ester under nanoscale constraint" *Macromolecules* 2008;41:1310-1317.
18. Li QX, Simon SL. "Surface chemistry effects on the reactivity and properties of nanoconfined bisphenol M dicyanate ester in controlled pore glass" *Macromolecules* 2009;42:3573-3579.
19. Koh YP, Li QX, Simon SL. "T_g and reactivity at the nanoscale" *Thermochimica Acta* 2009;492:45-50.
20. Amanuel S, Malhotra VM. "Effects of physical confinement (< 125 nm) on the curing behavior of phenolic resin" *Journal of Applied Polymer Science* 2006;99:3183-3186.
21. Andrikopoulos KS, Kalampounias AG, Yannopoulos SN. "Confinement effects on liquid–liquid transitions: pore size dependence of sulfur's living polymerization" *Soft Matter* 2011;7:3404-3411.
22. Malvaldi M, Bruzzone S, Picchioni F. "Confinement effect in diffusion-controlled stepwise polymerization by Monte Carlo simulation" *Journal of Physical Chemistry B* 2006;110:12281-12288.
23. Lin PH, Kohale SC, Khare R. "Effect of nanoconfinement on kinetics of cross-Linking reactions: A Molecular Simulation Study" *Journal of Physical Chemistry B* 2011;115:12348-12355.

24. Koh YP, Simon SL. "Trimerization of monocyanate ester in nanopores"
Journal of Physical Chemistry B 2010;114:7727-7734.
25. Jackson CL, McKenna GB. "The melting behavior of organic materials
confined in porous solids" Journal of Chemical Physics 1990;93:9002-9011.
26. Erb V. Diploma Thesis, Max-Planck-Institut für Polymerforschung, Mainz,
1993.
27. Odian G. Principles of Polymerization. 3rd ed. New York: Wiley; 2004.
28. Simon SL, Sobieski JW, Plazek DJ. "Volume and enthalpy recovery of
polystyrene" Polymer 2001;42:2555-2567.
29. Armitage PD, Hill S, Johnson AF, Mykytiuk J, Turner JMC. "Bulk
polymerization of methyl methacrylate: Part I: some kinetic and modeling
considerations for isothermal reactions" Polymer 1988;29:2221-2228.
30. Bauduin G, Pietrasanta Y, Rousseau A, GranierAzema D, Bosc D, Guilbert M.
"Etude par DSC de la polymérisation en masse des méthacrylates de méthyle et
de pentafluorophényle" European Polymer Journal 1992;28:923-927.
31. Feliu JA, Sottile C, Bassani C, Ligthart J, Maschio G. "Thermal
characterization of the polymerization of methyl methacrylate" Chemical
Engineering Science 1996;51:2793-2798.
32. Maschio G, Bello T, Scali C. "Optimal operation strategies to control the
molecular weight distribution of polymer products" Chemical Engineering
Science 1994;49:5071-5086.

33. O'Driscoll KF, Monteiro ML, Klumperman B. "The effect of benzyl alcohol on pulsed laser polymerization of styrene and methyl methacrylate" *Journal of Polymer Science Part A: Polymer Chemistry* 1997;35:515-520.
34. Zammit MD, Davis TP, Willett GD, O'Driscoll KF. "The effect of solvent on the homo-propagation rate coefficients of styrene and methyl methacrylate" *Journal of Polymer Science Part A: Polymer Chemistry* 1997;35:2311-2321.
35. Jang WS, Jensen AT, Lutkenhaus JL. "Confinement effects on cross-linking within electrostatic layer-by-layer assemblies containing poly (allylamine hydrochloride) and poly (acrylic acid)" *Macromolecules* 2010;43:9473-9479.
36. Doolittle AK. "Studies in Newtonian Flow. II. The dependence of the viscosity of liquids on free-space" *Journal of Applied Physics* 1951;22:1471-1475.

Table 3.1. Specifications of CPGs, as provided by manufacturer

Product name	Mean pore surface diameter (nm)	Pore diameter distribution (%)	Specific pore volume (cm ³ /g)	Specific area (m ² /g)
CPG00130B	13.0	7.4	0.68	130.0
CPG00500B	50.0	3.7	1.10	50.9
CPG01000B	110.6	3.6	1.06	25

Table 3.2. Total heat of reaction and the time to reach autoacceleration of the reactant under nanoscale constraints at different sizes at 80 °C

Surface Condition	Property	D (nm)			
Hydrophobic Silanized CPG	ΔH_T (kJ/mol)	∞	110.0	50.0	13.0
		563.1 ± 12.5	553.7 ± 6.7	556.1 ± 2.3	551.0 ± 1.5
Hydrophilic Native CPG	ΔH_T (kJ/mol)	∞	110.0	50.0	13.0
		563.1 ± 12.5	553.9 ± 12.8	553.9 ± 6.2	537.4 ± 23.4

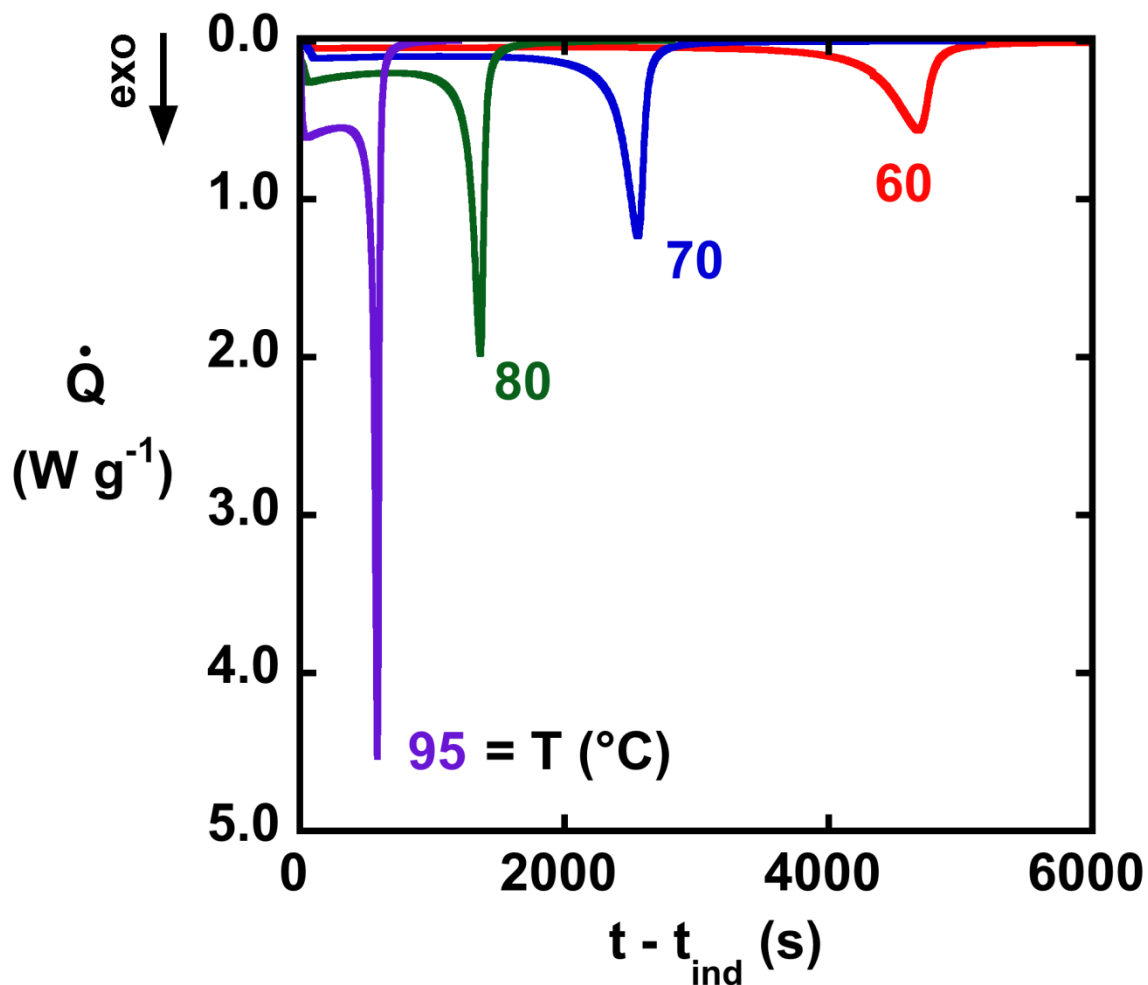


Figure 3.1. Heat flow versus time of isothermal polymerization at different temperatures for representative bulk samples.

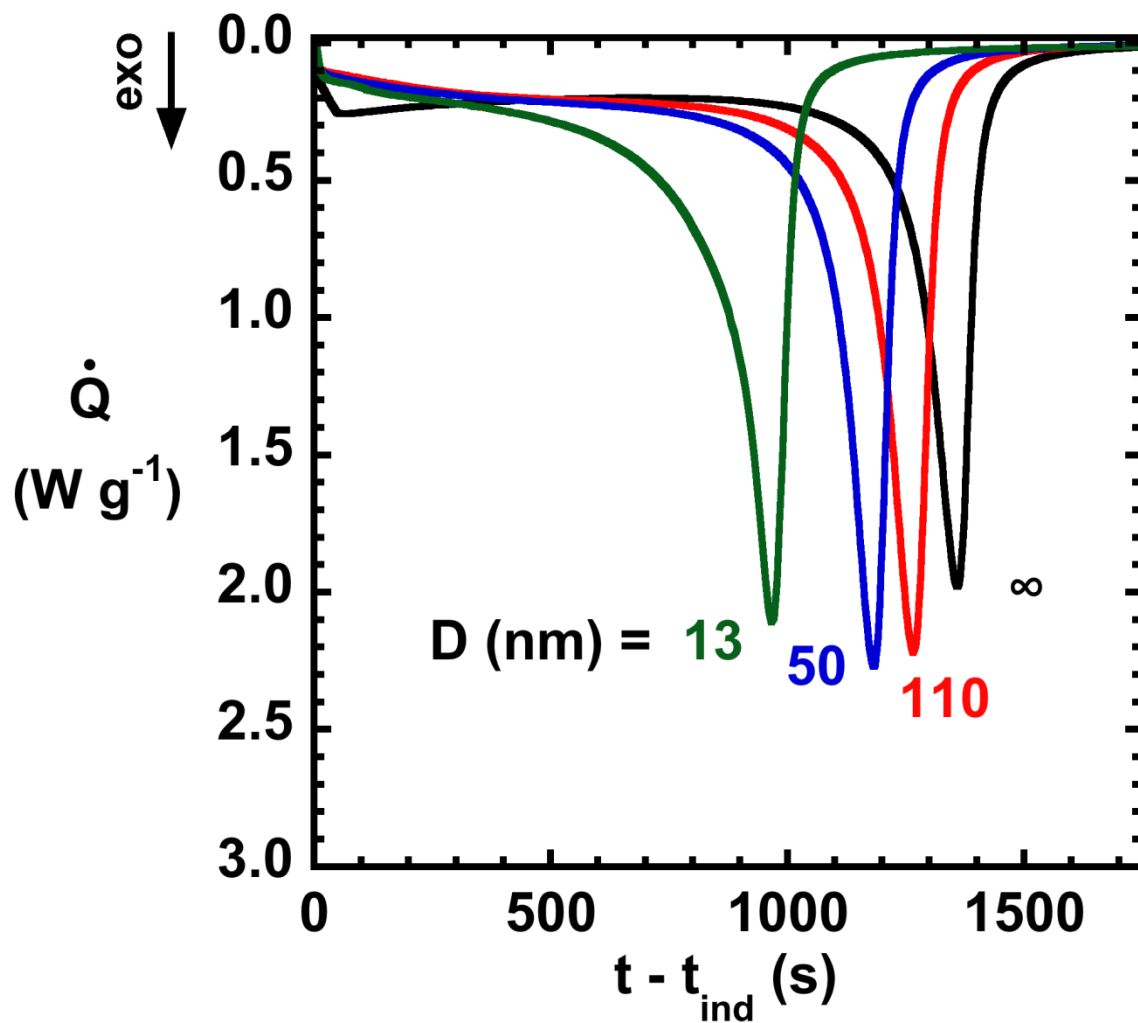


Figure 3.2a. Heat flow versus time of isothermal polymerization at 80 °C for representative samples in nanoconfined hydrophobic CPGs of diameter D . A representative bulk sample ($D = \infty$) is shown for comparison.

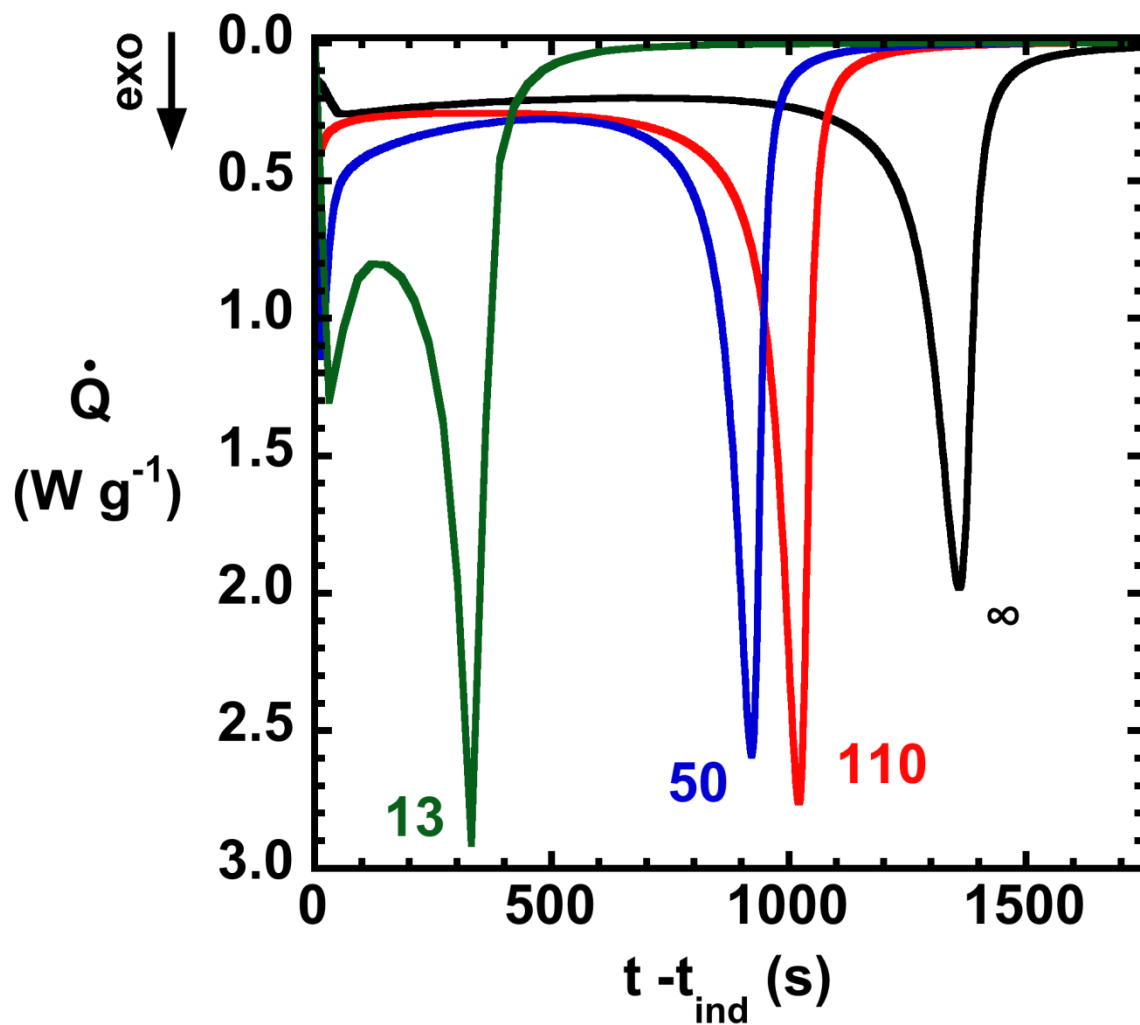


Figure 3.2b. Heat flow versus time of isothermal polymerization at 80 °C for representative samples in nanoconfined hydrophilic CPGs of diameter D . A representative bulk sample ($D=\infty$) is shown for comparison.

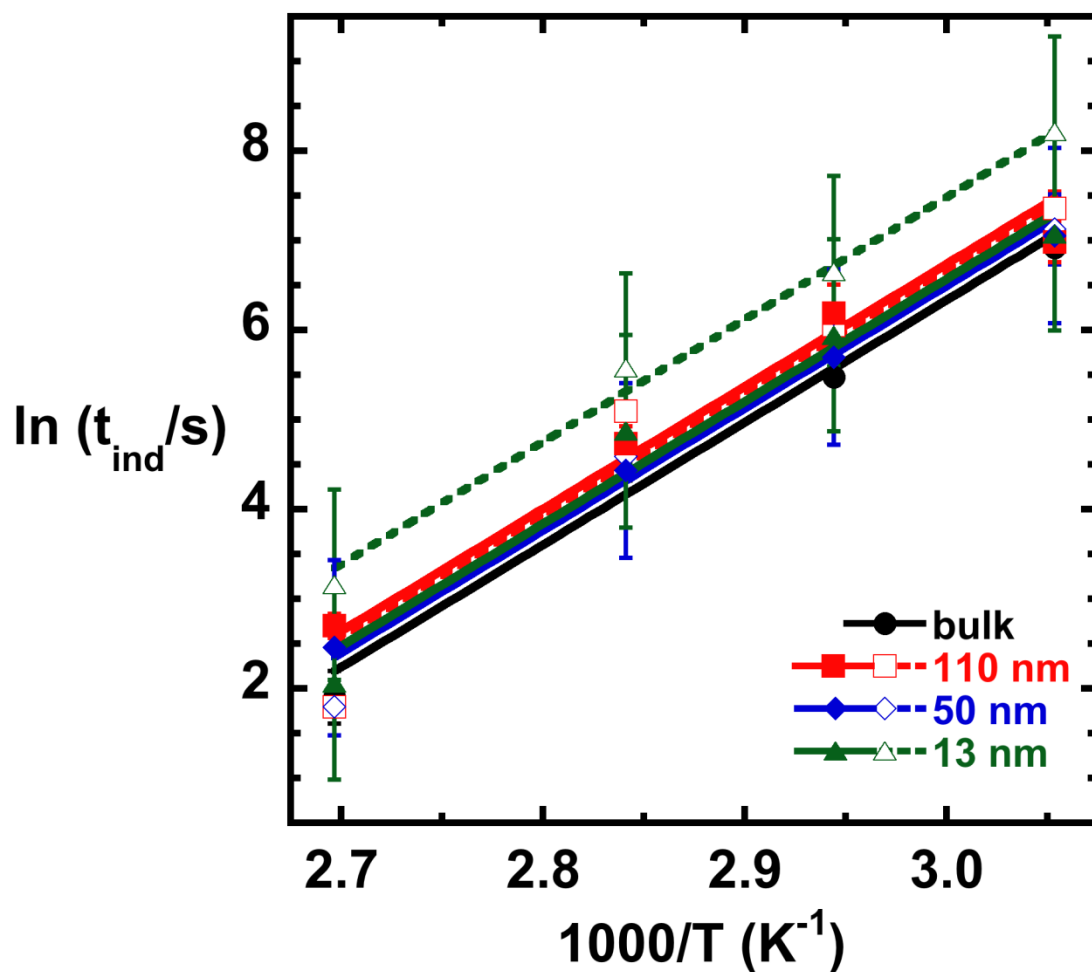


Figure 3.3. The induction time for bulk and samples in nanoconfined pores as a function of reciprocal temperature. Closed symbols indicate the nanoconfined hydrophobic samples and open symbols indicate the nanoconfined hydrophilic samples.

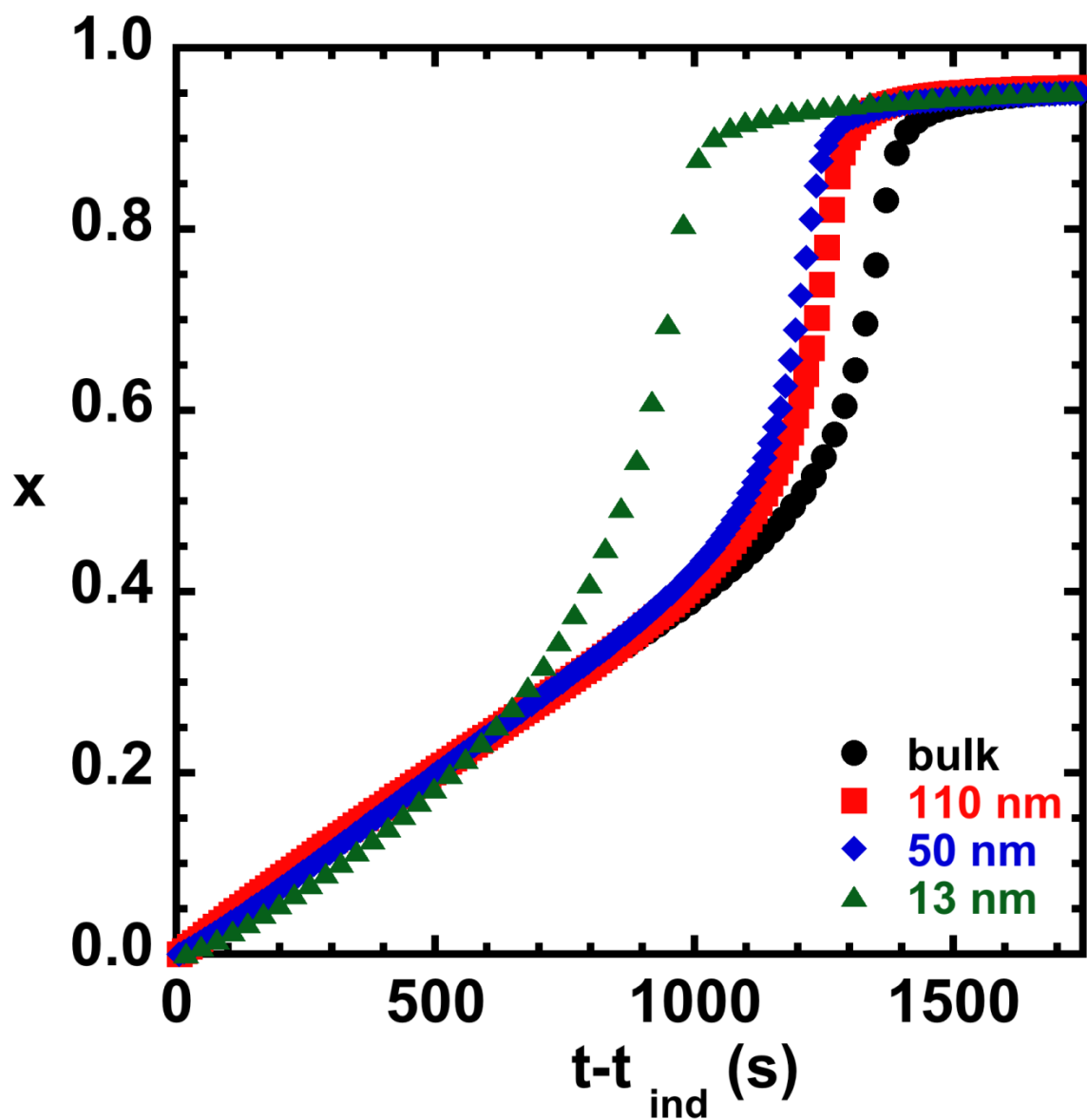


Figure 3.4a. Conversion versus time of isothermal polymerization for representative bulk and nanoconfined hydrophobic samples at 80 °C.

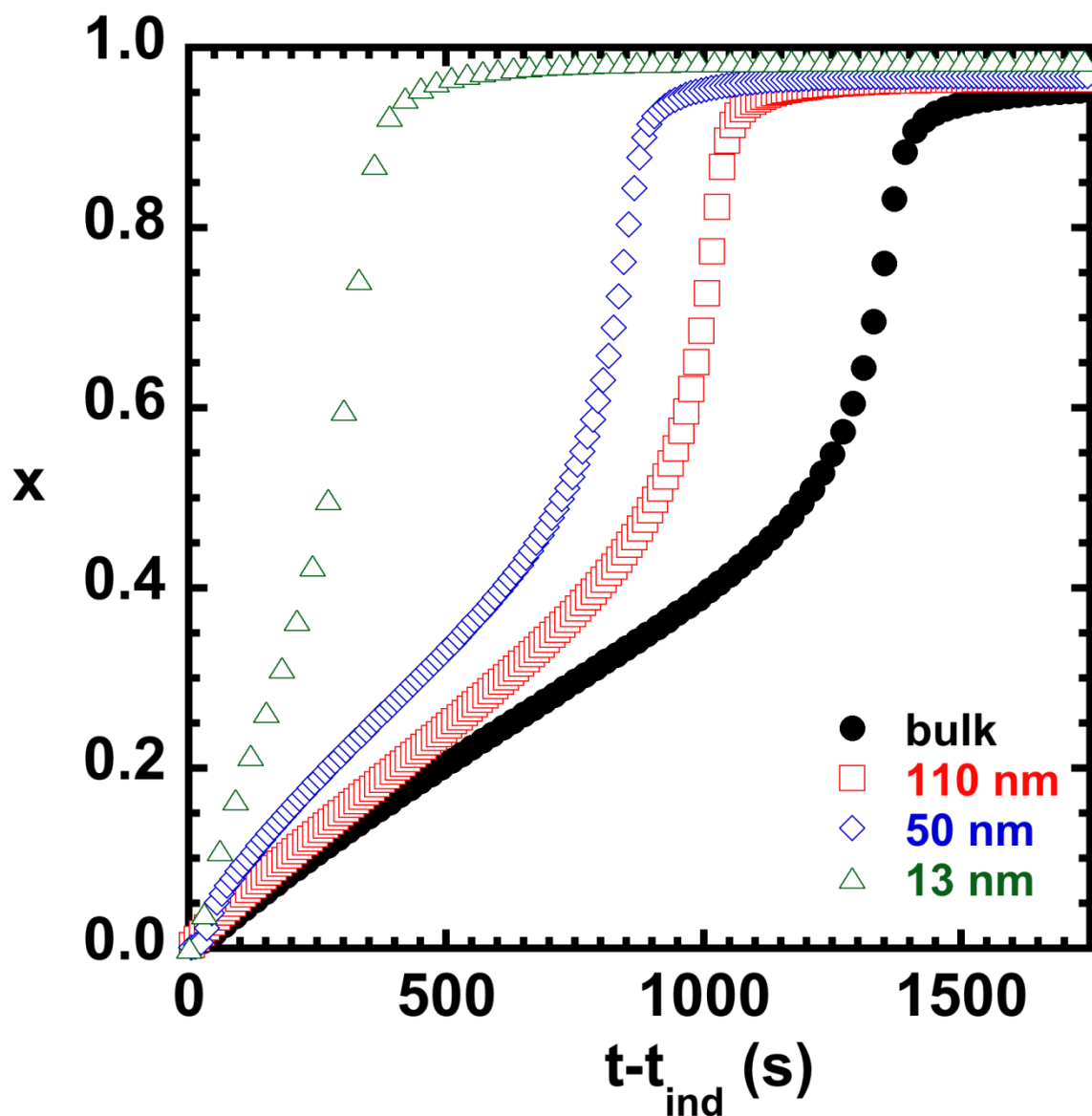


Figure 3.4b. Conversion versus time of isothermal polymerization for representative bulk and nanoconfined hydrophilic samples at 80 °C.

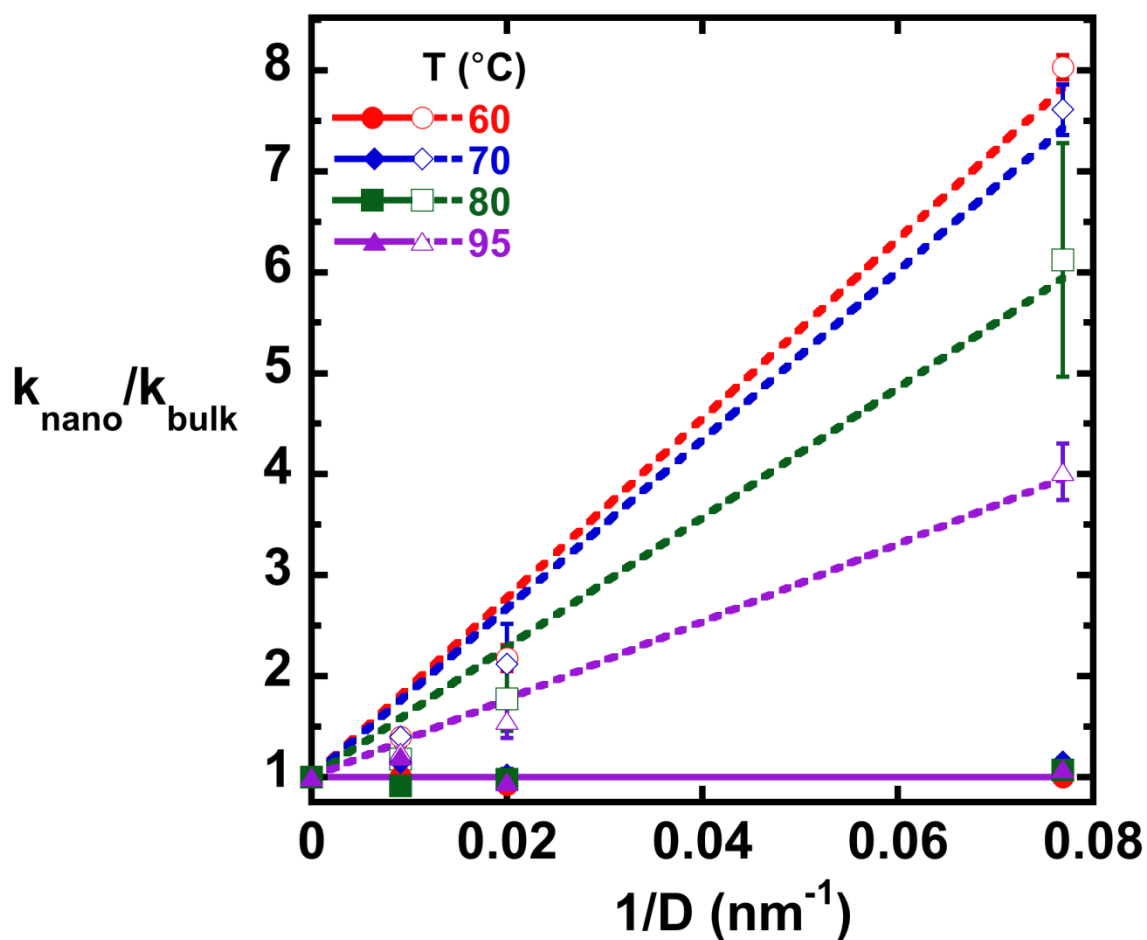


Figure 3.5. The effective rate constant prior to autoacceleration normalized by the bulk value for nanoconfined samples as a function of reciprocal pore diameter. Closed symbols indicate the nanoconfined hydrophobic samples and open symbols indicate the nanoconfined hydrophilic samples.

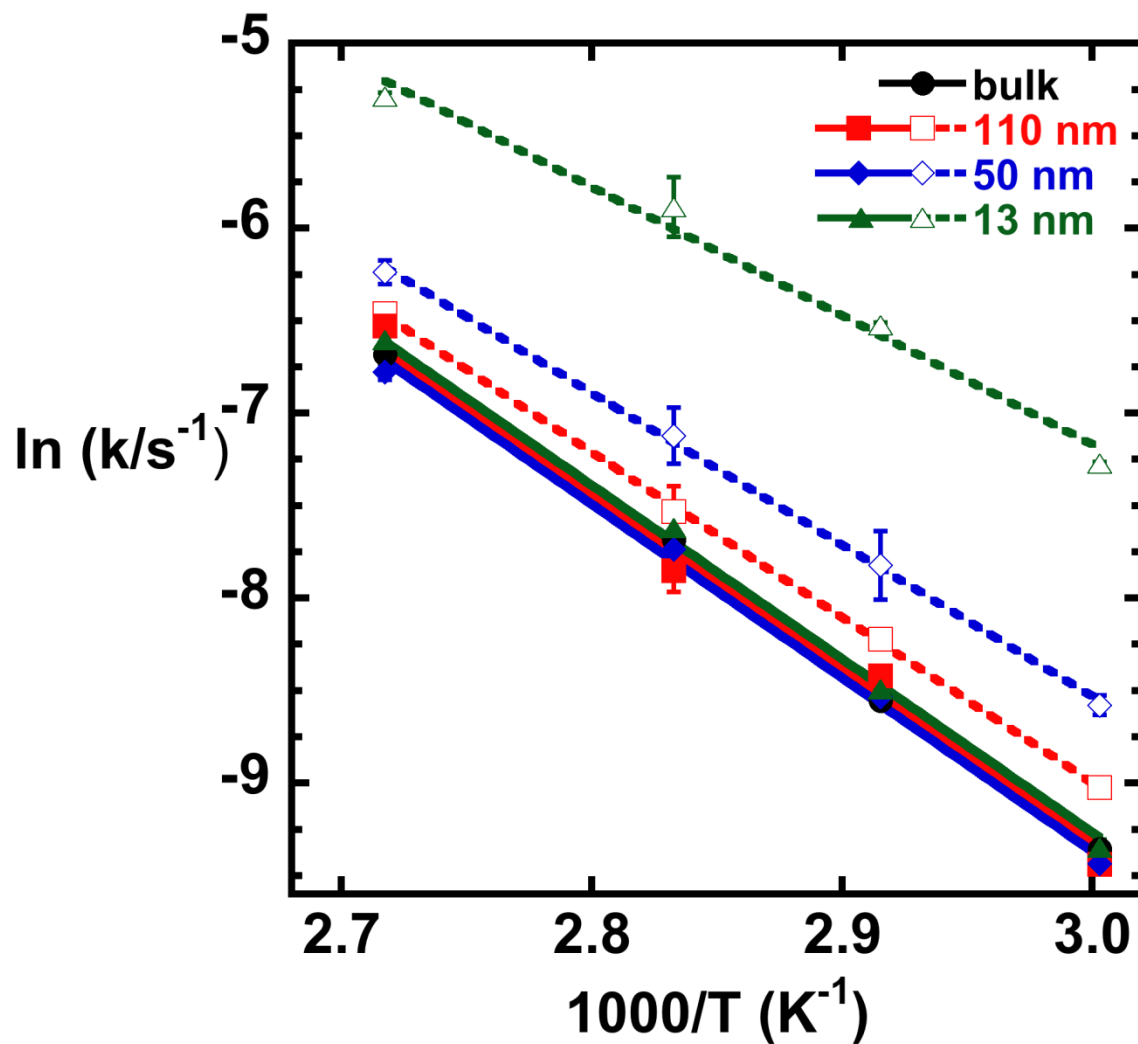


Figure 3.6. An Arrhenius plot for the effective rate constant prior to autoacceleration for bulk and nanoconfined samples. Closed symbols indicate the nanoconfined hydrophobic samples and open symbols indicate the nanoconfined hydrophilic samples.

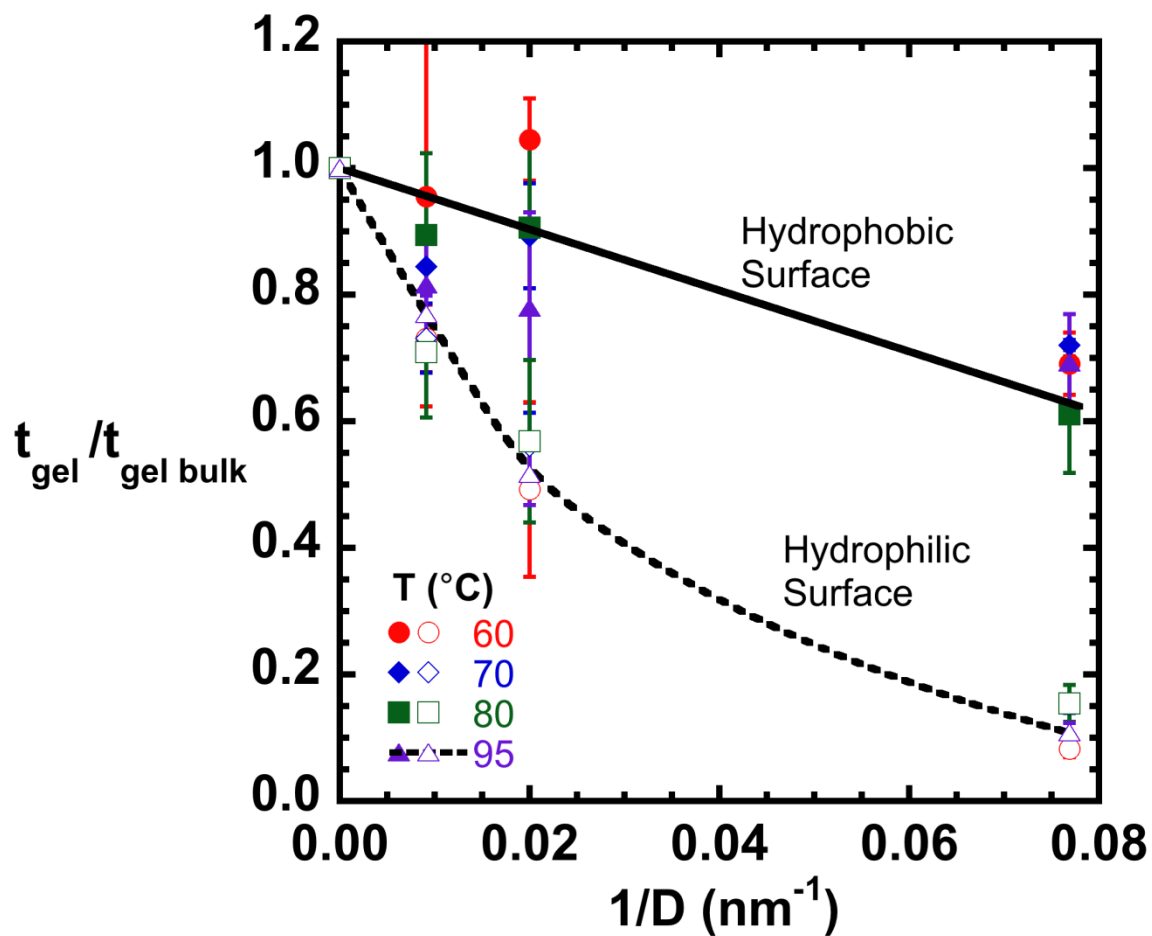


Figure 3.7. The time required to reach autoacceleration normalized by the time for the bulk samples as a function of reciprocal diameter. Closed symbols indicate the nanoconfined hydrophobic samples and open symbols indicate the nanoconfined hydrophilic samples.

CHAPTER 4

THE EFFECT OF NANOCONFINEMENT ON METHYL METHACRYLATE POLYMERIZATION: T_G , MOLECULAR WEIGHT, AND TACTICITY

4.1 Introduction

When monomer is polymerized in a nano-scale geometry, the resulting polymer properties are affected. For example, nanoconfinement is found to increase molecular weight and reduce the PDI in free radical polymerizations [1-8]. Synthesis under nanoconfinement also affects stereoregularity with the degree of isotacticity increasing for styrene, methyl methacrylate, and vinyl acetate polymerized in nanochannels of PCPs [7,9]. Moreover, the polymerization of vinyl acetate under nanoconfinement results in more linear structures with reduced chain branching [7]. The initiator efficiency in free radical polymerization has also been found to decrease under nanoconfinement resulting in a decrease in the final polymer yield [7]. Due to its potential to control polymer properties, it is of interest to further explore the use of nanoconfinement as a synthesis tool [2,3,7-9].

In Chapter 3, experimental work has previously focused on changes in reaction kinetics [10] for nanoconfined free radical polymerization of PMMA in CPG, where the onset of autoacceleration shifts to shorter time in both nanopores and the initial reaction rate is dramatically enhanced in hydrophilic pores. Both effects were quantitatively modeled [11-12] using a modified model from previous reaction kinetics model [13] based on Verros et al. model [14] to include scaling from the literature [15,16] for how chain diffusivity decreases on confinement. Given the

dramatic changes in polymerization reactivity and the reduced chain diffusivity, changes in the properties of PMMA synthesized under nanoconfinement, as reported in the literature [1-9], are expected. In this chapter, we examine the molecular weight and tacticity for PMMA synthesized in our CPG nanoconfined polymerization system; in addition, we examine the ability of kinetic and statistical models to describe the results.

PMMA obtained by solution free radical polymerization with AIBN is usually syndiotactic-rich, with the percentage of isotactic, syndiotactic, and atactic triads at approximately 6%, 56%, and 38% [17]. The conventional method to adjust the tacticity is by polymerization with metal catalysts (i.e., Ziegler-Natta catalysts) or, alternatively, by using living anionic polymerization [18] or free radical polymerization with fluoroalcohol or Lewis acids additives [19,20]. The potential to control tacticity for free radical polymerized PMMA without metal catalysts or strict environmental conditions via a physical method, such as nanoconfinement [7,9], may be practical and valuable. In prior work by other researchers [9], a helical pore geometry was used to control stereoregularity. In contrast, here, we show how surface chemistry coupled with nanoconfinement can be used to increase isotacticity.

In addition to increases in molecular weight and tacticity, the glass transition temperature (T_g) is found to increase for PMMA synthesized in nanopores [6,11,12,21] and in PMMA nanocomposites [22,23]. Strong specific interactions, such as hydrogen bonding, between PMMA and the substrate presumably account for the increase in T_g [24]. In this chapter, we further examine the effects of confinement

versus surface/substrate effects.

As mentioned, our focus is on the properties of PMMA synthesized under nanoconfinement in CPG. Gel permeation chromatography (GPC), ^1H nuclear magnetic resonance (^1H NMR), and differential scanning calorimetry (DSC) are used to characterize molecular weight, tacticity, and the glass transition temperature, respectively. The kinetic model used in previous work [11-13] is applied without adjustable parameters to predict the evolution of molecular weight under nanoconfinement, and a statistical model is applied to examine the dependence of tacticity on temperature. The results are discussed in the context of the current literature.

4.2 Methodology

4.2.1 Materials

The treatment of monomer MMA and initiator AIBN is the same as described in Chapter 3. The nanoconfined matrix (CPG) having cylindrical [25] pore diameters (D) of $13\text{ nm} \pm 7.4\%$ (manufacturer's specifications) was used as the confinement system. The CPG is composed of nanoporous borosilicate particles (37 to 74 μm in diameter) and is stable with respect to organic liquids [26, 27].

The PMMA products obtained by isothermal free radical polymerization needed to be extracted in order to study the changes in molecular weight and tacticity under nanoconfinement. First, CPG beads containing reacted polymer were immersed in tetrahydrofuran (THF) solvent including hydroquinone (~ 0.05 to 0.1 wt% of HQ) to

scavenge any active free radicals. After 72 h, the THF solution containing extracted PMMA and CPG was filtered and then dried at 80 °C in vacuum. The PMMA was extracted from the CPG based on the fact that the dried CPG showed no DSC signature for PMMA and no significant weight loss was observed using thermogravimetric analysis (TGA) to above 300 °C. After drying, a part of the extracted PMMA was redissolved in THF for GPC measurement, and a part PMMA was dissolved in CDCl₃ for ¹H NMR. A similar procedure using ethyl acetate (EA) as the extraction solvent also with hydroquinone was used to obtain extracted PMMA for T_g measurements due to the greater ease of removing the dried extracted sample from the vial.

4.2.2 Polymer Characterization

The molecular weights and corresponding polydispersity index were characterized by gel permeation chromatography using Phenomenex 00H-0444-K0, 00H-0445-K0, 00H-0446-K0 and 00H-0447-K0 columns in series with THF (HPLC Grade) as the mobile phase at 1 mL/min flow rate. A Varian 380-LC evaporative light scattering detector (ELSD) was used to monitor the effluent stream. The GPC calibration curve was obtained by characterizing six PMMA standards of different molecular weights ($M_p = 2.71, 10.9, 62.95, 298.9, 679, \text{ and } 1,677 \text{ kg mol}^{-1}$) purchased from Agilent Technologies. Molecular weights were calculated assuming a linear relationship between polymer mass concentration and detector response.

The polymer structure was analyzed by ¹H NMR using a JEOL ECS-400 spectrometer in CDCl₃ without tetramethylsilane. The chloroform peak at 7.24 ppm

was used for calibration. The triad tacticity of bulk PMMA was calculated by ^1H NMR to integrate the intensities of $\alpha\text{-CH}_3$ peaks to obtain the ratio of stereoregular sequences [17]. The study of PMMA tacticity focused on the chemical shift window of 0.6-1.4 ppm with the isotactic (mm), atactic (mr) and syndiotactic (rr) triads being assigned to 1.31-1.16, 1.11-0.95, and 0.95-0.72 ppm, respectively.

The glass transition temperatures (T_g) were obtained using a Mettler Toledo DSC823e with a Julabo FT100 intracooler and nitrogen purge gas. After isothermal reaction for times long enough to reach limiting conversions, three dynamic scans at 10 K/min from room temperature to 180 °C were used to measure the glass transition temperature. To investigate the T_g of "fully reacted PMMA" in nanopores without residual MMA solvent, after PMMA synthesis, a pinhole was introduced in the top of the hermetic pan, and then multiple DSC heating ramps to 180 °C were used to evaporate any residual MMA. For the bulk sample, this pinhole method gave a similar T_g value to that obtained using an extraction procedure (i.e., dissolving PMMA in ethyl acetate and then drying the sample for over 24 h at 80 °C in a vacuum oven): 111.4 °C vs. 111.8 °C, respectively.

4.3 Results

The M_n as a function of conversion for isothermal polymerization temperature of 80 °C is plotted in Figure 4.1a for PMMA samples extracted from 13 nm hydrophobic and hydrophilic pores, and data for bulk PMMA are also shown for comparison. The evolution of molecular weight shows two regions. In the initial kinetically controlled region, molecular weight decreases slightly with increasing

conversion. The value is given by the kinetic chain length ($\bar{\nu}$) assuming that termination reaction is dominated by disproportionation,

$$M_n = \bar{\nu} \cdot M_0 = \frac{k_p}{2(fk_d k_t)^{1/2}} \cdot \frac{[M] \cdot M_0}{[I]^{1/2}} \quad (4.1)$$

where M_0 is the molecular weight of monomer; k_p , k_d , k_t are the rate constants for the propagation, dissociation, and termination reactions; f is the initiator efficiency; and $[M]$ and $[I]$ are the monomer and initiator concentrations, respectively. The onset of autoacceleration, which occurs at around 40% conversion for the bulk, results in dramatic increase in $(k_p/k_t^{1/2})$ and in M_n . The number-average molecular weight near full conversion for bulk samples is 171,000 g/mol. This value is consistent with literature data [28] for PMMA polymerized in bulk with 0.5 wt% AIBN initiator (288,000 g/mol and 88,000 g/mol, at 70 and 90 °C, respectively [28]).

The evolution of the number-average molecular weight of PMMA synthesized in hydrophobic pores is similar to that of the bulk polymerization at low conversions. In Chapter 3, we have shown that the initial reaction rates in these two systems are the same, but since autoacceleration occurs earlier in the nanopores, at approximately 30% conversion [10], molecular weights in the pores are increased near full conversion. On the other hand, the number-average molecular weight of PMMA synthesized in hydrophilic pores is noticeable larger than either bulk or hydrophobic pores at all conversions because the initial reaction rate for MMA polymerization in hydrophilic pores is six times higher than that in the bulk and hydrophobic pores at the reaction temperature of 80 °C [10]. In addition, the earlier onset of autoacceleration at around 20% conversion for hydrophilic pores [10] causes further increases of the molecular

weight at high conversions. The models developed in previous work [11,12] to quantitatively describe the conversion versus time data (within 1% of the experimental data for the bulk reaction [11,12]) describe the M_n values reasonably well without any adjustable parameters and capture the dramatic increases in molecular weight due to autoacceleration.

The corresponding evolution of M_w during reaction at 80 °C is shown in Figure 4.1b and follows the same trend as number-average molecular weight. Samples synthesized in bulk and hydrophobic pores have similar weight-average molecular weights at low conversions, but M_w is significantly higher for samples synthesized in hydrophobic pores at high conversions due to the earlier onset of autoacceleration reported in this chapter ($M_{w,\text{hydrophobic}} = 600,000 \pm 49,000$ g/mol. $M_{w,\text{bulk}} = 402,000 \pm 17,000$ g/mol). In addition, M_w for samples synthesized in hydrophilic pores is increased at low conversion; however, only a small increase in M_w is observed for this sample as a function of conversion. Again, the data are reasonably described by our previous models [11,12] except that the predicted increase in M_w at autoacceleration is not observed for the PMMA synthesized in hydrophilic pores.

The dependence of the polydispersity index, PDI ($=M_w/M_n$) on conversion is shown in Figure 4.2. The PDI of bulk samples is initially 1.8 and decreases slightly at low conversions to approximately 1.6, then increases after autoacceleration to a value of 2.5 at full conversion. The initial PDI for samples in hydrophobic pores is similar to that of the bulk; however, the effect of nanoconfinement shifts the onset of autoacceleration to shorter times so that the increase in PDI for hydrophobic samples

occurs earlier relative to bulk. Although a higher PDI is observed immediately after autoacceleration, the final PDI in hydrophobic pores (~ 2.3) is smaller than in bulk, which is consistent with literature reports [1-3,6,7]. A similar but more dramatic effect is observed for PMMA synthesized in hydrophilic pores, with the final PDI being ~ 1.5 . Although the model [11,12] used for fitting the reaction kinetics describes M_n and M_w reasonably well, it does not quantitatively capture the evolution of PDI, as shown in the inset. The model does predict the increase in PDI after autoacceleration, but the model overestimates the PDI at high conversions, and it is unable to predict PDI values less than 2.0. The discrepancy may be related to a speculated increase in the rate of initiation upon nanoconfinement [11,12], although work by other researchers suggests initiator efficiency may decrease in nanoconfinement [7].

Representative NMR spectra of PMMA synthesized in bulk and hydrophilic pores for the reaction temperature of 80 °C are shown in Figure 4.3 to illustrate their differences in tacticity. Bulk PMMA is syndiotactic-rich with an appreciable atactic component ($mm/mr/rr = 8.9/34.5/56.5$). For the sample polymerized in hydrophilic nanopores, the two peaks assigned to the isotactic triads increase dramatically at the expense of both atactic and syndiotactic peaks, resulting in an isotactic-rich sample ($mm/mr/rr = 45.9/18.1/35.9$). For the sample polymerized in hydrophobic pores (not shown), the change is not as significant and the sample remains syndiotactic-rich, but with enhanced isotacticity relative to the bulk ($mm/mr/rr = 16.0/30.2/53.8$). The increased isotacticity for samples polymerized in CPG is primarily attributed to the strong interaction between PMMA and silanol groups in the case of hydrophilic pores

which is hypothesized to lead increased stereospecific chain growth [7]. A secondary minor enhancement in isotacticity arises from nanoconfinement.

The changes in tacticity as a function of temperature are plotted in Figure 4.4 for PMMA synthesized in bulk and in hydrophilic pores, while one data point at 80 °C is shown for samples prepared in hydrophobic pores. For the bulk samples, the isotactic and atactic character increase, whereas syndiotactic character decreases, with increasing temperature. This effect is expected because the syndiotactic structure is not favored at high temperature due to the lower energy for syndiotactic addition [29]. On the other hand, for the sample synthesized in hydrophilic pores, the isotactic character significantly increases as temperature increases, and both atactic and syndiotactic character decreases.

To quantitatively model the tacticity changes with temperature, statistical propagation models [30] are used. We focused on the chain end control models, as used in literature [31] for a PMMA having a similar degree of atacticity and also synthesized in the absence of catalyst. The Bernoullian model [30], which attributes tacticity effects to the last monomer unit, could only qualitatively reproduce the bulk data and could not describe the tacticity for PMMA synthesized in hydrophilic pores. The first-order Markov model [30], which includes the effect of the penultimate group, on the other hand, is able to quantitatively describe the temperature dependence of tacticity, as shown in Figure 4.4, for both bulk samples and samples synthesized in hydrophilic pores. A similar observation was found in results from Uemura et al. [9] where the first-order Markov model captured the increased isotacticity for PMMA

synthesized in PCP. In the first-order Markov model, the tacticity is simply described by the following equation [17,32,33]:

$$\ln\left(\frac{P_i}{P_s}\right) = \frac{S_i - S_s}{R} - \frac{H_i - H_s}{RT} \quad (4.2)$$

where P_i and P_s are the probabilities of the isotactic and syndiotactic diads, $S_i - S_s$ is the difference in entropy for propagating isotactic and syndiotactic diads, $H_i - H_s$ is the difference in enthalpy for propagating isotactic and syndiotactic diads, R is the gas constant, and T is the polymerization temperature. The ratio of diad probability is given by equations from literature [30,31]:

$$\frac{P_i}{P_s} = \frac{mm + mr/2}{rr + mr/2} \quad (4.3)$$

The results are plotted in an Arrhenius plot for both bulk and nanoconfined PMMA, as shown in Figure 4.5. From the slope and intercept, we obtain values of $H_i - H_s$ and $S_i - S_s$, respectively, and these are reported in Table 4.1 along with the tabulated experimental triad data and the model calculations. The enthalpic term weakly dominates the entropy term ($T \cdot \Delta S$) in bulk polymerization, leading to a slight tendency towards syndiotacticity, which decreases as temperature increases. However, for polymerization in hydrophilic pores, the entropic term increases dramatically and dominates the enthalpic term, resulting in a significant increase in isotacticity. In addition, the enthalpic term also increases, such that the temperature dependence of tacticity is stronger (see equation (4.2)).

The calorimetric traces for PMMA synthesized under bulk and nanoconfined conditions at 80 °C are shown in Figure 4.6. The solid lines show the DSC scans for

fully converted PMMA samples after residual MMA removal (i.e., using a pinhole in the lid of hermetic DSC pan), whereas the dashed lines are for samples extracted from the CPG after the synthesis in the nanopores. The results clearly show that T_g and the breadth of the transition both increase under nanoconfinement with samples synthesized in hydrophilic pores showing a more pronounced effect. Comparing the T_g of the fully converted samples in the CPG to that of the extracted samples (solid vs. dashed lines), we attribute the 8 K increase in T_g in the hydrophobic pores solely to the effect of nanoconfinement. An additional 4 K increase between the samples in and out of the CPG is observed for hydrophilic pores; this increase, which is considered significant, and can be explained by the interaction between PMMA and the silanol surface group [24]. A similar conclusion can be drawn from the T_g s of the as-prepared samples, where T_g increases by approximately 8 K in hydrophobic pores and by an additional 10 K in hydrophilic pores, as shown in Table 4.2. However, the as-prepared samples contain different amounts of residual MMA (with reduced residual monomer and higher polymer yields in hydrophilic pores [10-12]), which confounds the interpretation.

Based on the concern of the dependence of T_g on molecular weight [34], we also measure T_g for both bulk and nanoconfined samples at 60 and 95 °C in Figure 4.7ab, which stand for the highest to lowest molecular weight since molecular weight decreases as temperature increases. Comparing T_g for samples synthesized in bulk and in nanopores, the effect of molecular weights on T_g can be regarded as negligible, which is also consistent with Cowie's finding that the value of T_g stops increasing

with increasing molecular weight when the molecular weight is over 50,000 g/mol [35].

4.4 Discussion

As mentioned in the introduction and as found here, the T_g of PMMA synthesized under nanoconfinement increases. T_g changes are also observed for PMMA synthesized in bulk and then confined to nanoscale geometries. Keddie, Jones, and Cory first reported that the T_g of atactic PMMA ultrathin films supported on native silicon substrate increases with decreasing film thickness and is enhanced 6 K at 10 nm film thickness, whereas films on gold show the opposite trend with T_g decreasing 10 K relative to the bulk for a film thickness of approximately 15 nm. [24] Similar experiments on isotactic PMMA ultrathin films by Sharp and Forrest found that T_g increased 15 K in the case of uncapped PMMA supported on silicon substrates at 7 nm film thickness and T_g decreased 10 K in the case of capped PMMA supported on aluminum substrates at 7 nm. [36] Moreover, Prucker et al. found that T_g of PMMA supported on surface-treated hydrophobic silicon is reduced approximately 20 K relative to the bulk at 3 nm film thickness [37]. Hence, the literature clearly suggests that the strength of the interaction between the PMMA film and the substrate influences the T_g in thin films. On the other hand, without substrate, the study of freely standing PMMA films by Roth et al. shows that T_g monotonically decreases with decreasing film thickness [38]. The previous results are for PMMA films with low polydispersity (PDI) [36-38]. For atactic PMMA films, Vogt et al. [39] show that the change in T_g depends on PDI, with T_g increasing as film thickness decreases for

films with the lowest PDI (1.8), no change in T_g for films with intermediate PDI (2.2), and T_g decreasing as film thickness decreasing for films with the highest PDI (2.6). For our case, the PDI of samples in hydrophilic pores is similar to the lowest PDI reported in [39] (1.5 vs. 1.8) and the PDI of samples in hydrophobic pores is similar to the intermediate PDI in [39] (2.3 vs. 2.2). Thus, the different enhancements we observe for T_g in hydrophilic and hydrophobic pores may, in part, be influenced by PDI.

T_g confinement effects for thin films are clearly due to both free surface and substrate effects, whereas in our system for PMMA in nanopores, there is no free surface. Hence, literature dealing with confinement effects in other porous matrices or nanocomposites is perhaps more relevant to our case. For example, the T_g for PMMA polymerized in 5 nm diameter sol-gel-derived SiO_2 pore glasses [6] or 3 nm zeolite mesopores [21] increased 13 or 11 K, respectively. In PMMA nanocomposite systems where MMA is polymerized in the presence of metal nanoparticles (PMMA/Ce, PMMA/Co) [22] or in the presence of organic bentonite (PMMA/OBT) [23], T_g increased on the order of 10 K. In our system, the enhanced T_g in two dimensional confined hydrophobic pores is attributed to a confinement effect; on the other hand, the native hydrophilic pores with acidic silanol groups (-SiOH) distributed at the pore surface will interact with the carbonyl bond (-CO-) of PMMA via specific interactions [24]. Hence, the specific interactions plus confinement effect in hydrophilic CPG apparently further suppresses segmental mobility causing the T_g shifts to higher temperatures.

In addition to nanoconfinement, stereoregularity is an important factor for controlling T_g : the T_g of pure syndiotactic PMMA can be $140 \sim 160$ °C, as much as 50 °C higher than conventional atactic PMMA [34,40], whereas the T_g of pure isotactic PMMA is reduced to 40 °C [41]. The influence of stereoregularity on the nanoconfinement effect is also interesting. For example, the T_g of *s*-PMMA (>80%) decreases as film thickness decreases, whereas T_g of *i*-PMMA (>97%) increases as film thickness decreases [42]. Another discrepancy between syndiotacticity and isotacticity is that both α and β -relaxations shift to lower temperatures for syndiotactic thin films, whereas only the α -relaxation is shifted for isotactic thin films. Although our PMMA synthesized in hydrophilic pores shows a significantly higher percentage of isotactic triads, we do not attribute our changes in T_g to changes in tacticity because the T_g of the extracted samples is very close to the T_g of the bulk samples (i.e., within 3 K of the bulk for both samples extracted from hydrophobic and hydrophilic pores in spite of tacticity differences associated with the two pore types.) In addition, no broadening of the transition is observed after the samples are extracted from the nanopores.

Glass formers under nanoporous confinement generally show two T_g s. [26,43-50] The primary T_g is depressed and attributed to material in the pore center, whereas the secondary T_g is observed at higher temperatures and is attributed to wall surface interaction. [26,43-50] Recently, it has been reported that PMMA confined in 80 nm anodic aluminum oxide (AAO) templates [51] shows one T_g after being hyperquenched at cooling rates of 120 K/s and shows two T_g s after slowly cooling

rates of 10 K/min or after annealing above $T_{g,bulk}$ (> 130 °C) for several hours (> 2 hour). In the present work, however, we observe only a broadened single T_g with no indication of two T_g s even after 24 h of annealing at temperatures ranging from 130 to 150 °C. Therefore, we presume that although the center of the pore and the wall surface have different mobilities, the difference is such that the T_g at wall and T_g in the center merge to form one broadened transition, as shown in Figure 4.6. A possible explanation for the seeming discrepancy between our work and that in AAO [51] is the size of the pores. Our pores at 13 nm in diameter may be too small to support a large gradient in mobility, whereas Xue's AAO pores are 80 nm in diameter [51]. This explanation is supported by results from Ellison and Torkelson [52] where the mobility of a surface layer decreases with decreasing underlayer film thickness such that large gradients in mobility do not occur.

Our hydrophilic nanoporous confinement system has another interesting feature in its potential for producing free radical vinyl polymers with enhanced isotacticity. As shown in Figure 4.4, we obtained more than 50 % isotactic triads at 95 °C, an increase of almost a factor of five compared to the same polymerization in bulk. Stereoregular polymers are hard to achieve in free-radical polymerization since the steric repulsion of the substituent on the monomer favors syndiotacticity. For example, enhancements of isotacticity by a strong external gravity field [53] only show changes in isotacticity of one percentage with AIBN or several percentage points with benzyl mercaptan (e.g., from 5% to 10%). Alternatively, the stereoregularity of PMMA synthesized in PCP can be tuned by chemically substituting the organic ligand

resulting in more than a 20 % increased isotacticity relative to the bulk (from 5 % to 28 %) [7,9]. In the latter work, the enhancement in isotacticity was attributed to the small helical pore structure (< 1 nm), which forces stereospecific propagation due to steric effects of the ligand, rather than to interaction between PMMA and the pore surface [9]. In our case, in contrast, we observe a small increase in isotacticity for PMMA synthesized in hydrophobic 13 nm pores and a much larger increase for hydrophilic pores. Thus, our data suggest that specific interactions between the growing chain or monomer at the hydrophilic pore surface exerts a more important influence than the geometric confinement effect, inducing stereospecific propagation akin to the effects of fluoroalcohols but without the additives. We anticipate that higher isotacticity levels may be achievable by reducing the hydrophilic CPG pore diameter and increasing reaction temperatures.

4.5 Conclusion

The properties of PMMA synthesized in the nanopores of controlled pore glass (CPG) have been investigated for both hydrophobic and hydrophilic pores. The initial number-average molecular weights prior to autoacceleration are similar for PMMA synthesized in the bulk and hydrophobic pores, but higher molecular weights are observed for hydrophilic pores due to higher initial reaction rates. The number-average molecular weights increase at autoacceleration in all three cases, but due to the earlier onset of autoacceleration in the pores, molecular weights near full conversion are increased. The growth of weight-average molecular weight follows the same trend as M_n . The final PDI of samples synthesized in hydrophobic pores is

lower than that in bulk (2.3 vs. 2.5), whereas the effect in hydrophilic pores is even more pronounced (~ 1.5). The evolution of molecular weight is reasonably described by our previous model of the reaction kinetics without adjustable parameters.

Isotacticity is found to obviously increase in hydrophilic pores due to interaction with the silanol groups at the wall surface. Isotacticity increases with increasing temperature and the results are well represented by the statistical first-order Markov model. The glass transition temperature of PMMA in the CPG increases for both pores surfaces; a 10 K increase in T_g in hydrophobic pores is presumed to be solely due to confinement, whereas an additional 4 K increase observed in hydrophilic pores is presumed to be due to a confinement effect plus the interaction between PMMA and the surface silanol groups.

References

1. Li XC, King TA, Pallikari-Viras F. "Characteristics of composites based of PMMA modified gel silica glasses" *Journal of Non-Crystalline Solids* 1994;170:243-249.
2. Ng SM, Ogino S, Aida T, Koyano KA, Tatsumi T. "Free radical polymerization within mesoporous zeolite channels" *Macromolecular Rapid Communications* 1997;18:991-996.
3. Kageyama K, Ng SM, Ichikawa H, Aida T. "Macromolecular synthesis using mesoporous zeolites" *Macromolecular Symposia* 2000;157:137-142.
4. Ni XF, Shen ZQ, Yasuda H. "Polymerization of methyl methacrylate with samarocene complex supported on mesoporous silica" *Chinese Chemical Letters* 2001;12:821-822.
5. Kalogeras IM, Vassilikou-Dova A. "Dielectric probe of intermolecular interactions in poly (methyl methacrylate)(PMMA) and PMMA+ SiO₂ matrixes doped with luminescent organics" *Journal of Physical Chemistry B* 2001;105:7651-7662.
6. Kalogeras IM, Neagu ER. "Interplay of surface and confinement effects on the molecular relaxation dynamics of nanoconfined poly(methyl methacrylate) chains" *European Physical Journal E* 2004;14:193-204.
7. Uemura T, Ono Y, Kitagawa K, Kitagawa S. "Radical polymerization of vinyl monomers in porous coordination polymers: Nanochannel size effects on

- reactivity, molecular weight, and stereostructure" *Macromolecules* 2008;41:87-94.
8. Ikeda K, Kida M, Endo K. "Polymerization of methyl methacrylate with radical initiator immobilized on the inside wall of mesoporous silica" *Polymer Journal* 2009;41:672-678.
 9. Uemura T, Ono Y, Hijikata Y, Kitagawa S. "Functionalization of coordination nanochannels for controlling tacticity in radical vinyl polymerization" *Journal of the American Chemical Society* 2010;132:4917-4924.
 10. Zhao HY, Simon SL. "Methyl methacrylate polymerization in nanoporous confinement" *Polymer* 2011;52:4093-4098.
 11. Begum F, Zhao HY, Simon SL. "Modeling methyl methacrylate free radical polymerization: Reaction in hydrophilic nanopores" *Polymer* 2012;53:3238-3244.
 12. Begum F, Zhao HY, Simon SL. "Modeling methyl methacrylate free radical polymerization: Reaction in hydrophobic nanopores" *Polymer* 2012;53:3261-3268.
 13. Begum F, Simon SL. "Modeling methyl methacrylate free radical polymerization in nanoporous confinement" *Polymer* 2011;52:1539-1545.
 14. Verros GD, Latsos T, Achilias DS. "Development of a unified framework for calculating molecular weight distribution in diffusion controlled free radical bulk homo-polymerization" *Polymer* 2005;46:539-552.

15. Cui T, Ding J, Chen JZY. "Dynamics of a self-avoiding polymer chain in slit, tube, and cube confinements" *Physical Review E* 2008;78:061802(1-7).
16. Avramova K, Milchev A. "Polymer chains in a soft nanotube: A Monte Carlo Study" *Journal of Chemical Physics* 2006;124:024909(1-8).
17. Bovey FA, Tiers GVD. "Polymer NSR spectroscopy. II. The high resolution spectra of methyl methacrylate polymers prepared with free radical and anionic initiators" *Journal of Polymer Science* 1960;44:173-182.
18. Kitayama T, Nakagawa O, Hatada K. "Intra-and intermolecular stereocomplex formation of uniform stereoblock poly (methyl methacrylate)" *Polymer Journal* 1996;28:150-154.
19. Lutz JF, Jakubowski W, Matyjaszewski K. "Controlled/living radical polymerization of methacrylic monomers in the presence of Lewis acids: influence on tacticity" *Macromolecular Rapid Communications* 2004;25:486-492.
20. Yamada K, Nakano T, Okamoto Y. "Stereospecific free radical polymerization of vinyl esters using fluoroalcohols as solvents" *Macromolecules* 1998;31:7598-7605.
21. Moller K, Bein T, Fischer RX. "Entrapment of PMMA polymer strands in micro-and mesoporous materials" *Chemistry of Materials* 1998;10:1841-1852.
22. Zanotto A, Spinella A, Nasillo G, Caponetti E, Luyt AS. "Macro-micro relationship in nanostructured functional composites" *eXPRESS Polymer Letters* 2012;6:410-416.

23. Ouaad K, Djadoun S, Ferfera-Harrar H, Sbirrazzuoli N, Vincent L. "Synthesis and thermal behavior of poly(methyl methacrylate)/Maghnia bentonite nanocomposite prepared at room temperature via in situ polymerization initiated by a new Ni(II) α -benzoinoxime complex" *Journal of Applied Polymer Science* 2011;119:3227–3233.
24. Keddie JL, Jones RAL, Cory RA. "Interface and surface effects on the glass-transition temperature in thin polymer films" *Faraday Discussions* 1994;98:219-230.
25. Jackson CL, McKenna GB. "The melting behavior of organic materials confined in porous solids" *Journal of Chemical Physics* 1990;93:9002-9011.
26. Li QX, Simon SL. "Surface chemistry effects on the reactivity and properties of nanoconfined bisphenol M dicyanate ester in controlled pore glass" *Macromolecules* 2009;42:3573-3579.
27. Koh YP, Simon SL. "Trimerization of monocyanate ester in nanopores" *Journal of Physical Chemistry B* 2010;114:7727-7734.
28. Balke ST, Hamielec AE. "Bulk polymerization of methyl methacrylate" *Journal of Applied Polymer Science* 1973;17:905–949.
29. Fordham JW, Burleigh PH, Sturm CL. "Stereoregulated polymerization in the free propagating species. III. Effect of temperature on the polymerization of vinyl chloride" *Journal of Polymer Science* 1959;41:73-82.
30. Odian G. *Principles of Polymerization*. 3rd ed. New York: Wiley; 2004.

31. Moad G, Solomon DH, Spurling TH, Johns SR, Willing RI. "Tacticity of poly (methyl methacrylate). Evidence for a penultimate group effect in free-radical polymerization" *Australian Journal of Chemistry* 1986;39:43-50.
32. Ishitake K, Satoh K, Kamigaito M, Okamoto Y. "Stereospecific free radical and RAFT polymerization of bulky silyl methacrylates for tacticity and molecular weight controlled poly (methacrylic acid)" *Macromolecules* 2011;44:9108-9117.
33. Bovey FA. "Polymer NMR spectroscopy. III. The rates of the propagation steps in the isotactic and syndiotactic polymerization of methyl methacrylate" *Journal of Polymer Science* 1960;46:59-64.
34. Thompson EV. "Dependence of the glass transition temperature of poly (methyl methacrylate) on tacticity and molecular weight" *Journal of Polymer Science Part A-2: Polymer Physics* 1966;4:199-208.
35. Cowie JMG. "Some general features of T_g -M relations for oligomers and amorphous polymers" *European Polymer Journal* 1976;11:297-300.
36. Sharp JS, Forrest JA. "Dielectric and ellipsometric studies of the dynamics in thin films of isotactic poly (methyl methacrylate) with one free surface" *Physical Review E* 2003;67:031805(1-9).
37. Prucker O, Christian S, Bock H, Ruhe J, Frank CW, Knoll W. "On the glass transition in ultrathin polymer films of different molecular architecture" *Macromolecular Chemistry and Physics* 1998;199:1435-1444.

38. Roth CB, Pound A, Kamp SW, Murray CA, Dutcher JR. "Molecular-weight dependence of the glass transition temperature of freely-standing poly (methyl methacrylate) films" *European Physical Journal E* 2006;20:441-448.
39. Dion M, Larson AB, Vogt BD. "Impact of low-molecular mass components (oligomers) on the glass transition in thin films of poly (methyl methacrylate)" *Journal of Polymer Science Part B: Polymer Physics* 2010;48:2366-2370.
40. Karasz FE, MacKnight WJ. "The influence of stereoregularity on the glass transition temperatures of vinyl polymers" *Macromolecules* 1968;1:537-540.
41. Bywater S, Toporowski PM. "Effect of stereostructure on glass transition temperatures of poly (methyl methacrylate)" *Polymer* 1972;13:94-96.
42. Grohens Y, Hamon L, Reiter G, Soldera A, Holl Y. "Some relevant parameters affecting the glass transition of supported ultra-thin polymer films" *European Physical Journal E* 2002;8:217-224.
43. Schuller J, Melnichenko YB, Richert R, Fischer EW. "Dielectric Studies of the Glass Transition in Porous Media" *Physical Review Letters* 1994;73:2224-2227.
44. Gorbatschow W, Arndt M, Stannarius R, Kremer F. "Dynamics of H-bonded liquids confined to nanopores" *Europhysics Letters* 1996;35:719-724.
45. Arndt M, Stannarius R, Gorbatschow W, Kremer F. "Dielectric investigations of the dynamic glass transition in nanopores" *Physical Review E* 1996;54:5377-5390.

46. Park JY, McKenna GB. "Size and confinement effects on the glass transition behavior of polystyrene/o-terphenyl polymer solutions" *Physical Review B* 2000;61:6667-6676.
47. Trofymuk O, Levchenko AA, Navrotsky A. "Interfacial effects on vitrification of confined glass-forming liquids" *Journal of Chemical Physics* 2005;123:194509(1-7).
48. Zheng W, Simon SL. "Confinement effects on the glass transition of hydrogen bonded liquids" *Journal of Chemical Physics* 2007;127:194501(1-11).
49. Li QX, Simon SL. "Curing of bisphenol M dicyanate ester under nanoscale constraint" *Macromolecules* 2008;41:1310-1317.
50. Koh YP, Li QX, Simon SL. " T_g and reactivity at the nanoscale" *Thermochimica Acta* 2009;492:45-50.
51. Li LL, Zhou DS, Huang DH, Xue G. "Double glass transition temperatures of poly (methyl methacrylate) confined in alumina nanotube templates" *Macromolecules* 2014;47:297-303.
52. Ellison CJ, Torkelson JM. "The distribution of glass-transition temperatures in nanoscopically confined glass formers" *Nature Materials* 2003;2:695-700.
53. Nishihara M, Teramoto K, Sakurai T, Takafuji M, Mashimo T, Ihara H. "Enhancement of isotacticity in bulk radical polymerization of poly (methyl methacrylate) under strong gravity field" *Polymer Journal* 2003;35:276-279.

Table 4.1. Tacticity versus temperatures for bulk and nanoconfined PMMA

Temperature (°C)		60	70	80	95
Bulk					
Experimental	mm	0.062	0.079	0.089	0.119
	mr	0.331	0.343	0.346	0.345
	rr	0.607	0.578	0.566	0.537
First-order Markov model*	P _i	0.228	0.250	0.262	0.291
	P _s	0.772	0.750	0.738	0.709
	M R	0.726	0.686	0.661	0.592
	R M	0.214	0.229	0.234	0.243
	S _i - S _s	17.9 ± 1.9 J mol ⁻¹ K ⁻¹			
	H _i - H _s	9.3 ± 0.7 kJ mol ⁻¹			
	Hydrophilic 13 nm				
Experimental	mm	0.334	0.392	0.459	0.523
	mr	0.224	0.202	0.181	0.168
	rr	0.442	0.407	0.360	0.309
First-order Markov model*	P _i	0.446	0.493	0.550	0.607
	P _s	0.554	0.507	0.450	0.393
	M R	0.251	0.205	0.165	0.138
	R M	0.202	0.199	0.201	0.213
	S _i - S _s	55.8 ± 2.3 J mol ⁻¹ K ⁻¹			
	H _i - H _s	19.2 ± 0.8 kJ mol ⁻¹			
	Hydrophobic 13 nm				
Experimental	mm			0.160	
	mr			0.302	
	rr			0.538	
First-order Markov model*	P _i			0.311	
	P _s			0.689	
	M R			0.486	
	R M			0.219	

* First-order Markov model is obtained from literature 28, 29, where M | R is the probability that a syndiotactic diad will be formed after an isotactic diad, and R | M is the opposite.

Table 4.2. T_g of synthesized samples in pores versus after MMA removal and extraction

Temperature (°C)	60	70	80	95
As Prepared				
Bulk	100.9 ± 1.0	99.6	99.3	97.8 ± 0.9
Hydrophobic	107.5 ± 1.7	106.0	106.7	108.5 ± 0.3
Hydrophilic	118.5 ± 0.4	117.6	116.7	118.3 ± 0.6
After MMA Removal*				
Bulk	113.8	112.6	111.4	111.4
Hydrophobic	122.4	122.1	122.4	122.4
Hydrophilic	126.9	126.5	126.6	126.1
After Extraction**				
Bulk			111.8	
Hydrophobic			114.6	
Hydrophilic			114.5	

* Residual MMA removed by heating the sample to 180 °C using a DSC pan with a pinhole

** Dissolve multiple PMMA samples in ethyl acetate and then dry the samples for over 24 h at 80 °C in a vacuum oven

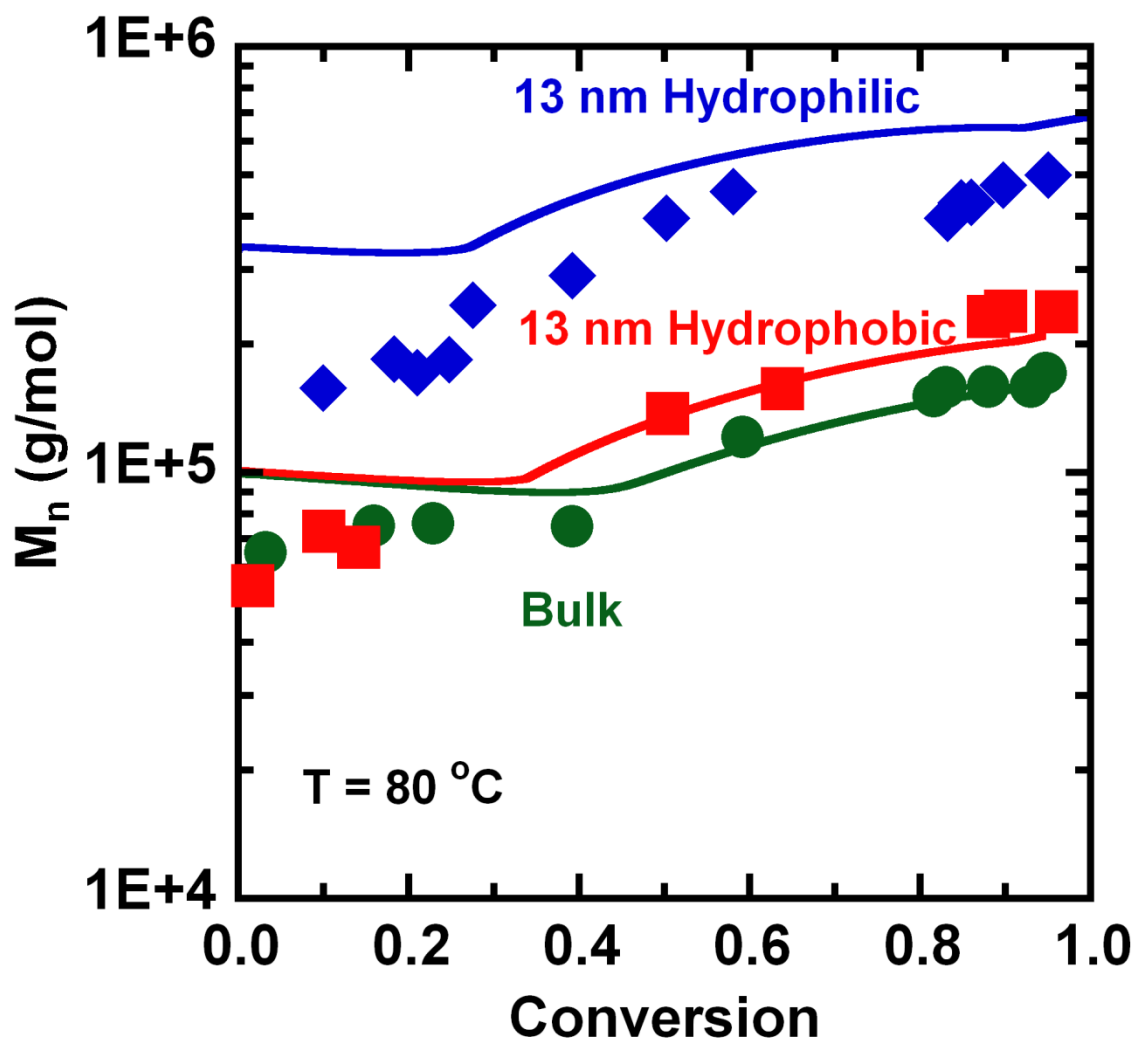


Figure 4.1a. Number-average molecular weight as function of conversion for PMMA synthesized in nanopores and in bulk. Symbols represent experimental data and lines represent the previous modeling results [11,12].

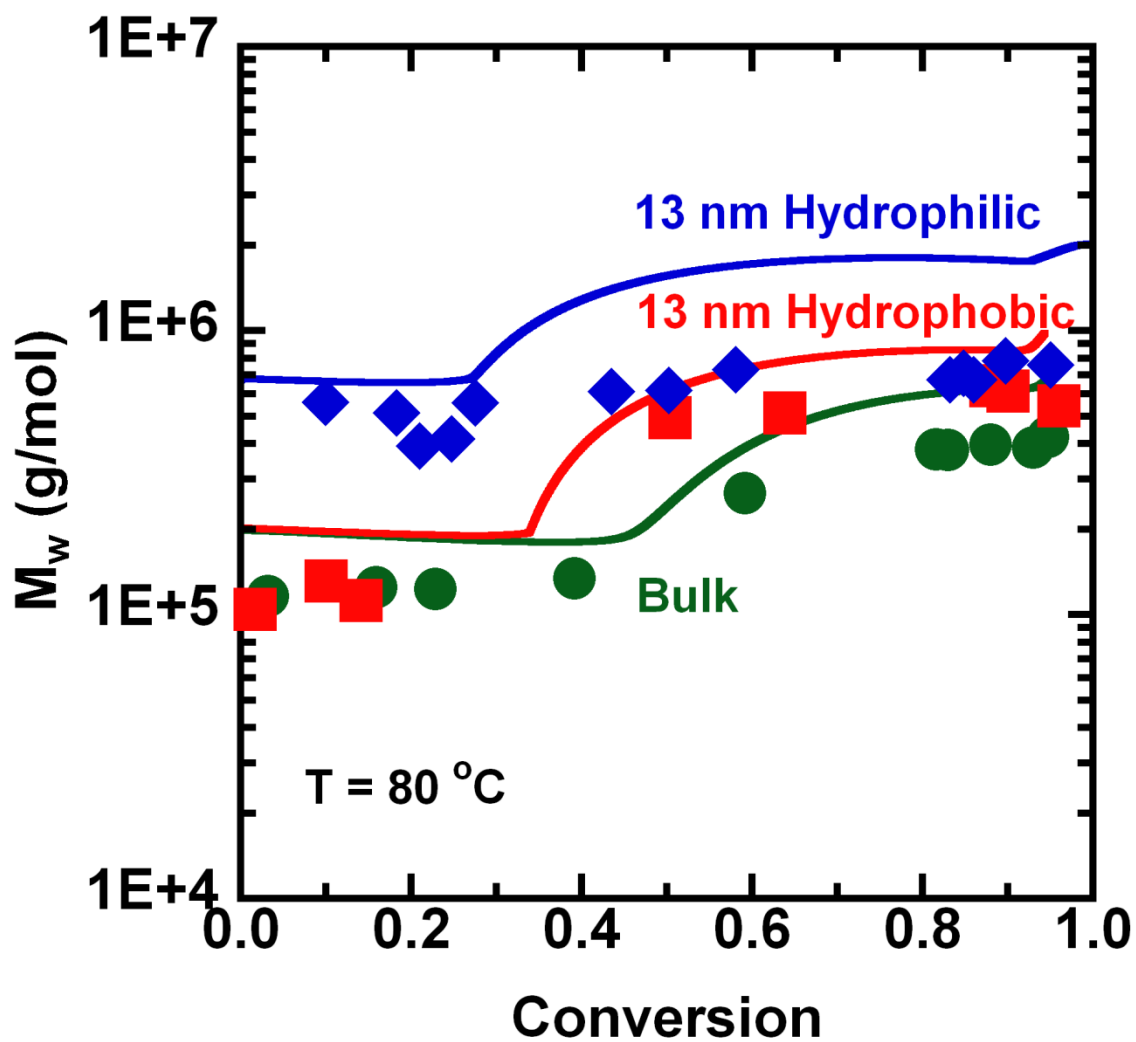


Figure 4.1b. Weight-average molecular weight as function of conversion for PMMA synthesized in nanopores and in bulk. Symbols represent experimental data and lines represent the previous modeling results [11,12].

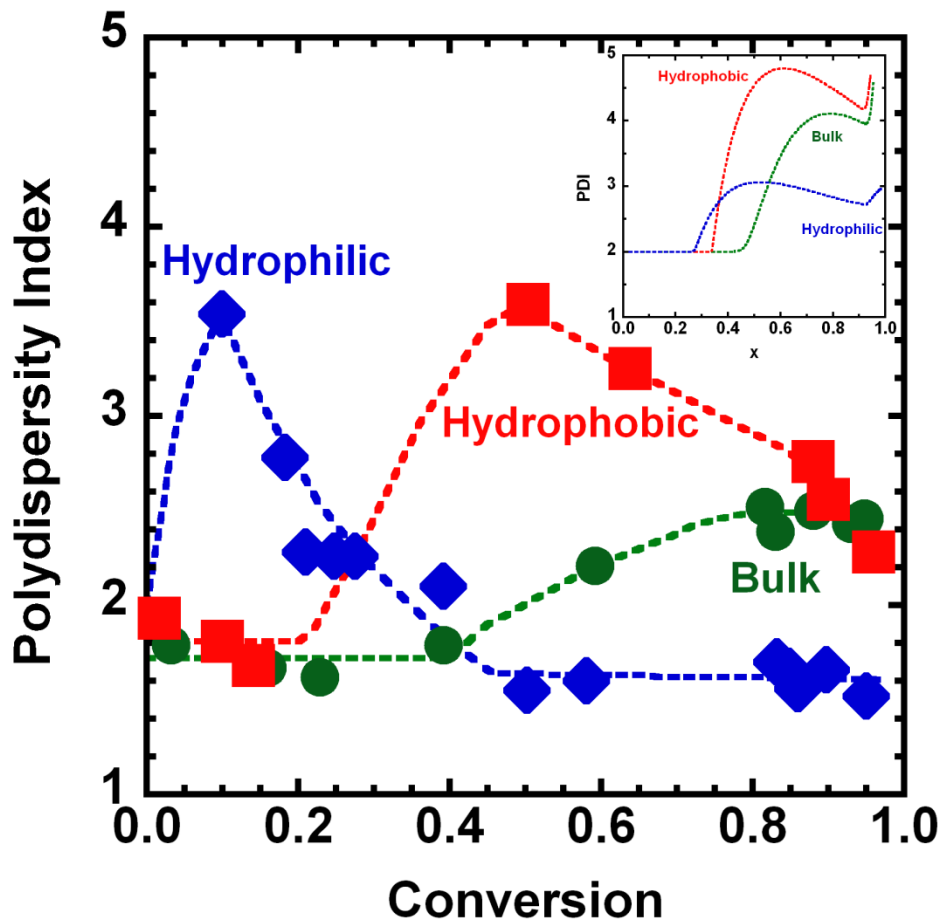


Figure 4.2. The polydispersity (PDI) versus conversion for hydrophobic/hydrophilic pores and bulk at 80 °C. Symbols represent the experimental data. The dashed line is the guide to the eye. The inset figure is the prediction from the previous modeling work [11,12].

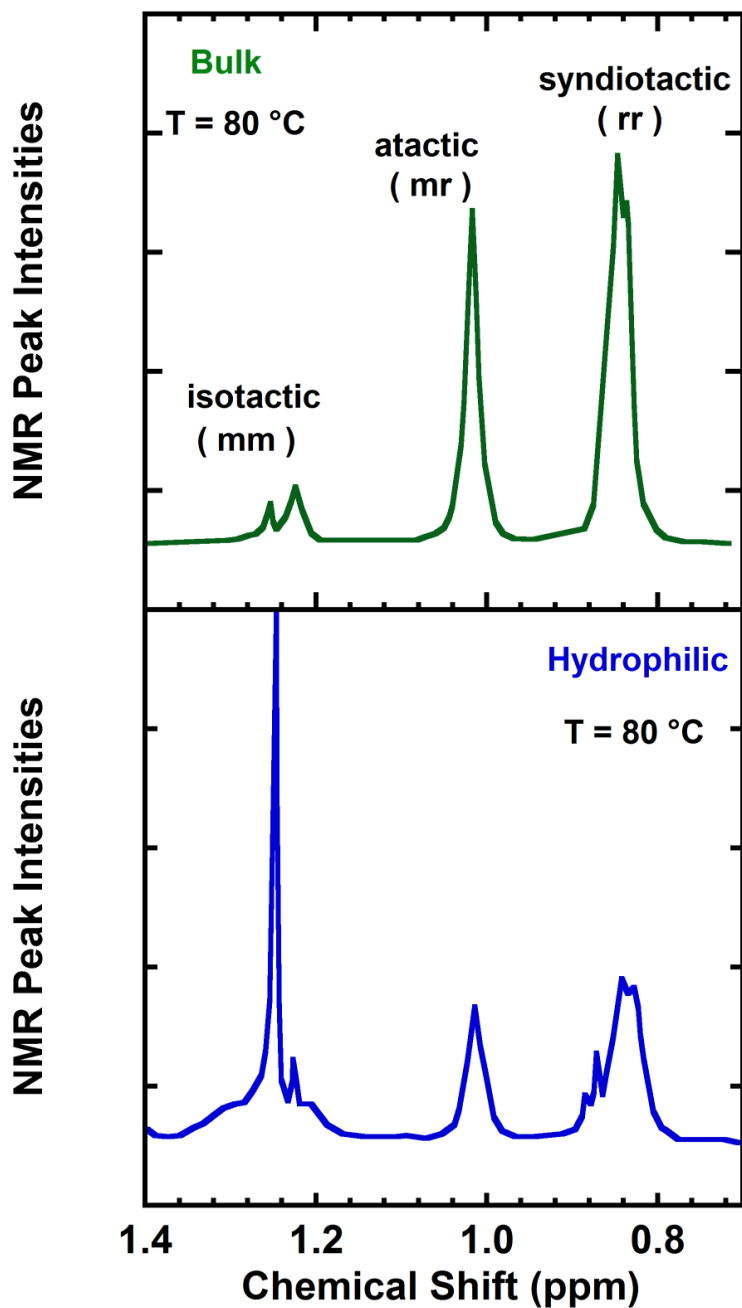


Figure 4.3. ^1H NMR spectra of α -CH₃ of PMMA in CDCl₃ for PMMA synthesized at 80 °C in bulk (top panel) or in hydrophilic 13 nm pores (bottom panel).

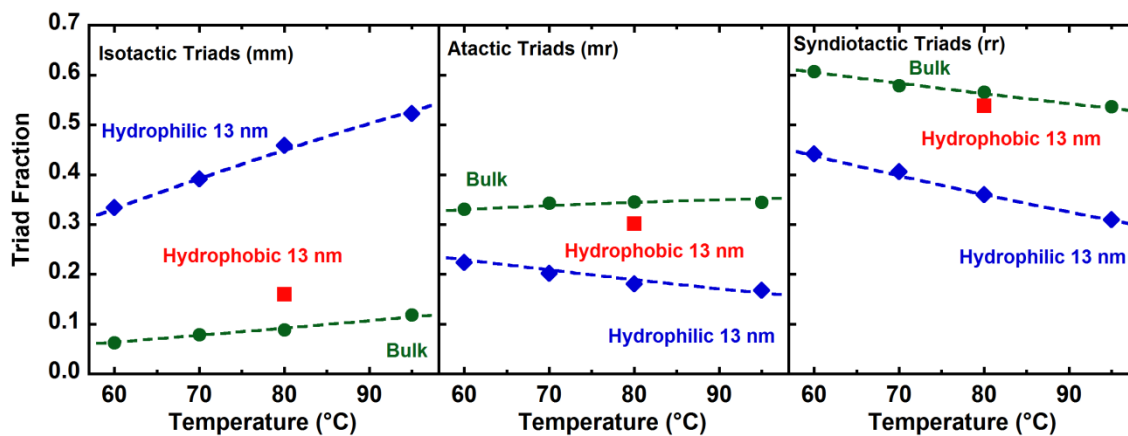


Figure 4.4. The dependence of isotactic triads, atactic triads, and syndiotactic triads on temperature for PMMA synthesized in nanopores and in bulk. The symbols represent NMR experimental data and lines are fitting results from first-order Markov model.

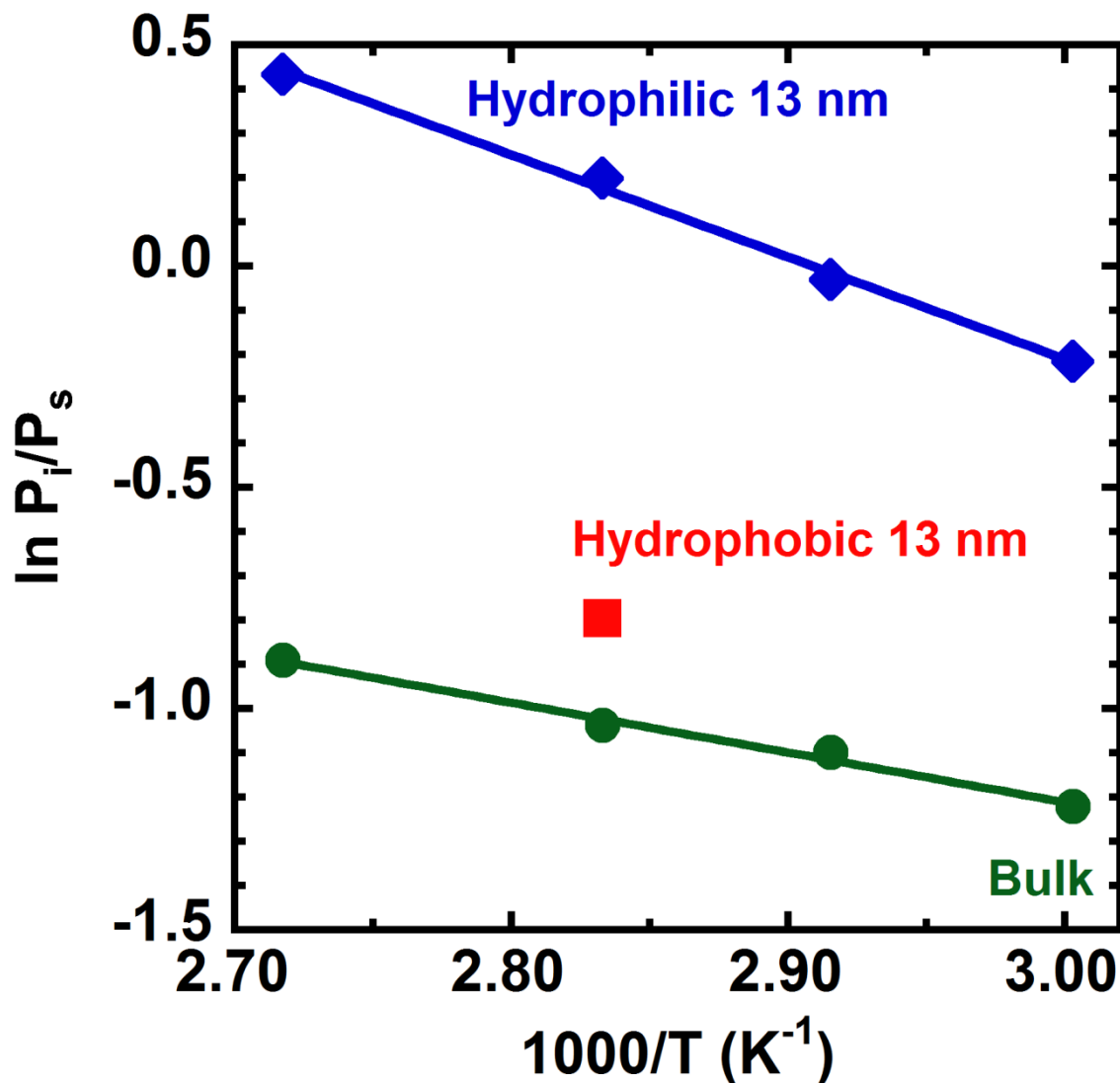


Figure 4.5. The dependence of isotactic to syndiotactic diad ratio (P_i/P_s) on temperature for PMMA synthesized in nanopores and in bulk. The symbols represent diads calculated from NMR experimental data and lines are a fit to equation (4.2).

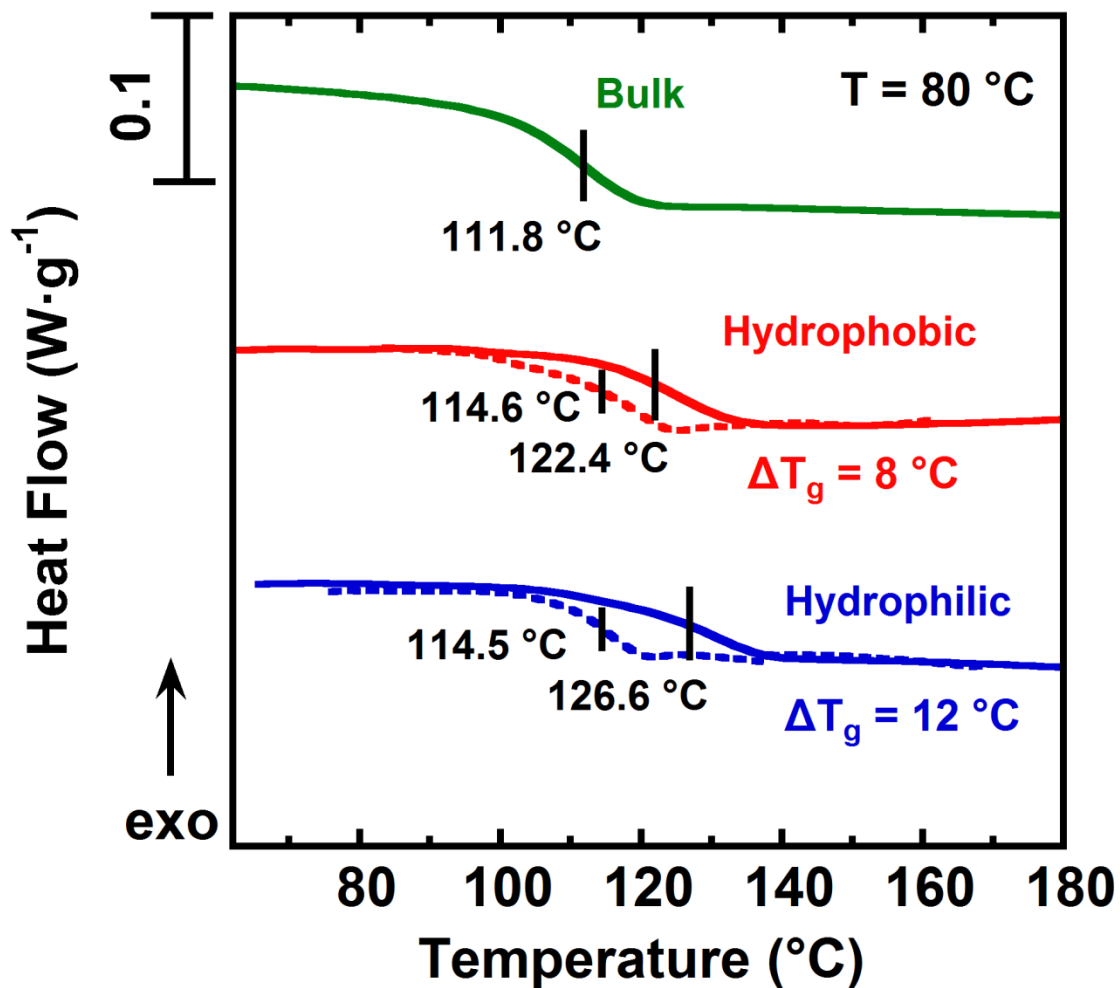


Figure 4.6. Heat flow versus temperature for PMMA polymerized in bulk and synthesized under nanoconfined conditions at 80 °C. The dashed lines and solid lines represent samples after extraction and after MMA removal, respectively. The vertical line indicates the glass transition temperature.

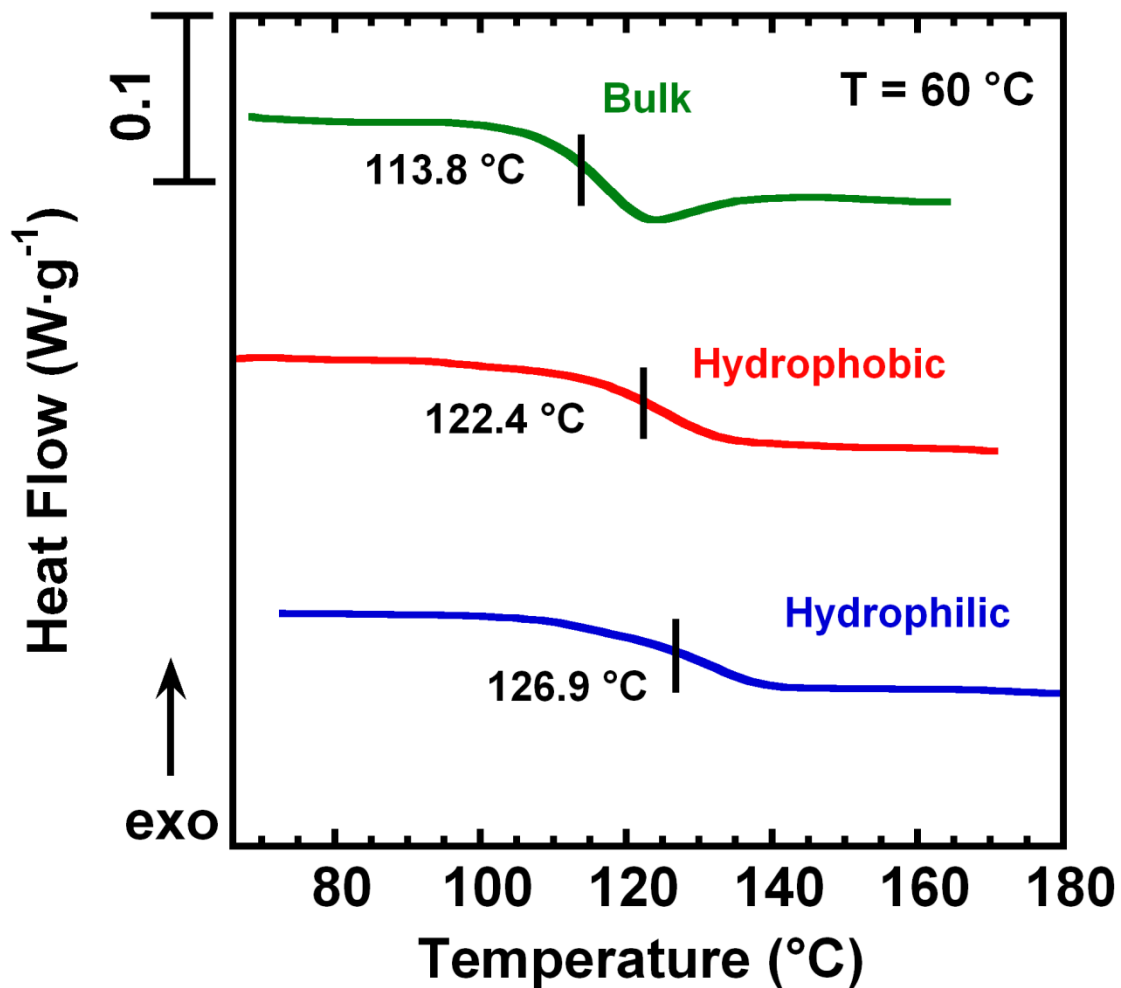


Figure 4.7a. Heat flow versus temperature for bulk and nanoconfined samples polymerized in pinhole at 60 °C. The solid line indicates the glass transition temperature.

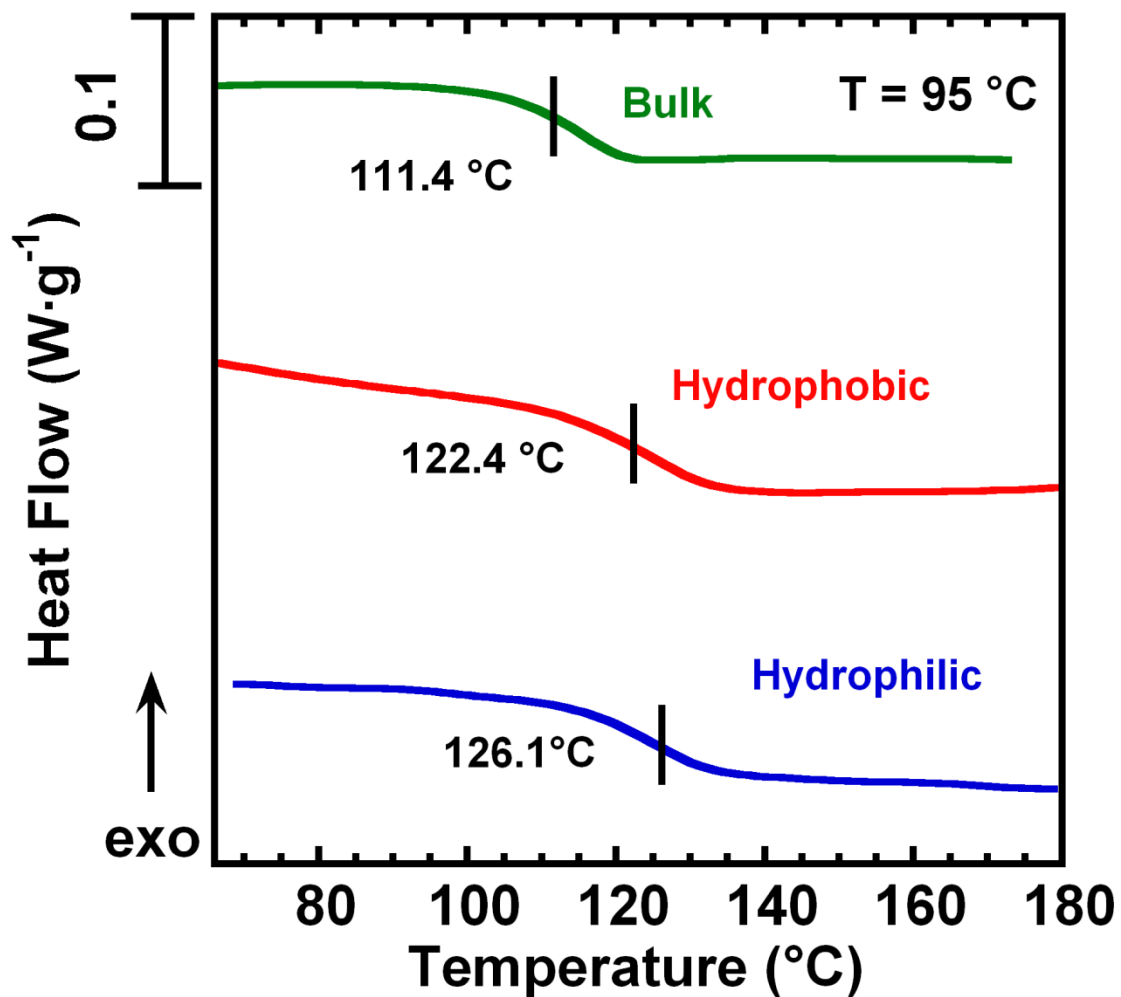


Figure 4.7b. Heat flow versus temperature for bulk and nanoconfined samples polymerized in pinhole at 95 °C. The solid line indicates the glass transition temperature.

CHAPTER 5

EQUILIBRIUM FREE- RADICAL POLYMERIZATION OF METHYL METHACRYLATE UNDER NANOCONFINEMENT

5.1 Introduction

The properties of polymers synthesized under nanoconfinement can be enhanced relative to bulk behavior, with observations of increased molecular weight, [1-8] increased tacticity, [7,9] and increased glass transition temperature [6,10-12]. In Chapter 3 and Chapter 4, we have investigated the reaction kinetics and properties of free radical polymerization of methyl methacrylate (MMA) in the nanopores of controlled pore glass (CPG) [13,14] and found that the onset of autoacceleration shifted to shorter times presumably due to the reduced diffusivity of the nanoconfined chains. In addition, in hydrophilic pores, the initial propagation rate was higher than that in either hydrophobic pores or the bulk system due to the catalysis by silanol groups on the CPG surface. [13] The enhanced reactivity was accompanied by increased molecular weight, increased isotacticity, and increased T_g . [14] However, previous experiments were carried out at relatively low temperatures ($< 95\text{ }^\circ\text{C}$); here we examine higher reaction temperatures where monomer/polymer equilibrium plays a role.

Neat polymerization of MMA can be divided into two regimes, depending on the temperature. When the reaction temperature is below the glass transition temperature of pure PMMA ($T_{g,p} \approx 111\text{ }^\circ\text{C}$), conversion will be limited by vitrification which occurs when the T_g of the system (polymer plus MMA as plasticizer) rises to

the reaction temperature. On the other hand, as the reaction temperature increases beyond $T_{g,p}$, complete polymerization becomes hard to achieve since the depolymerization gradually becomes important [15]. In other words, the competition between propagation and depropagation of MMA leads to a temperature-dependent equilibrium conversion.

Our interest in this chapter is the influence of nanoconfinement on the equilibrium conversion. Such studies have been performed for sulfur polymerization. [21,22] In that work, conversion decreases as the size of monolithic silica nanopores decreases from bulk to 2.5 nm, and the floor temperature (the lowest temperature where polymerization can occur since sulfur has a positive change in enthalpy and entropy upon polymerization) is shifted to higher temperatures indicating that $\Delta S_{p,conf}$ decreases due to nanoconfinement. Our modeling work [23] well describes the nanoconfinement effect on sulfur polymerization assuming scaling of $\Delta S_{polymer,conf} \sim -N^p D^{-m}$, where $p = 2$ represents strong confinement and m is 3.0 from self-consistent field theory [17] or 3.8 or 3.9 from blob scaling in semidilute solutions [19], both for spherical confinement. Similar to sulfur polymerization, polymerization of PMMA is expected be affected by nanoconfinement. However, in the case of MMA, the ceiling temperature is expected to decrease because the signs of ΔS_p and ΔH_p for MMA polymerization are negative.

One motivation of this work is to obtain information concerning the entropy change upon confining a chain to nanoscale dimensions, which is anticipated to depend on chain length [16-19], with greater confinement entropy associated with

longer chains. This is hypothesized to lead to a decrease in the change in the entropy of reaction, and a concomitant decrease in the equilibrium conversion, as shown schematically in Figure 5.1, where the solid and dashed lines represent the entropy for samples in bulk and in nanoconfined pores, respectively. Given that the entropy of polymer chains is reduced due to restricted chain configurations under confinement ($S_{\text{polymer,bulk}} > S_{\text{polymer,confined}}$), whereas the entropy of small molecules is not significantly influenced under confinement ($S_{\text{monomer,bulk}} \approx S_{\text{monomer,confined}}$); thus, it is anticipated that the change in the entropy of nanoconfined MMA polymerization on confinement ($\Delta S_{\text{confined rxn}}$) is a more negative value than the change in entropy for the bulk reaction ($\Delta S_{\text{bulk rxn}}$).

The thermodynamics of polymer chains in confined environment has been discussed by De Gennes [16] who suggested that the decrease in entropy due to confinement of an ideal chain ($\Delta S_{\text{polymer,conf}}$) in a tube or in a cylindrical pore is linearly proportional to the number of monomer units (N) and proportional to the square of the ratio of unperturbed size of the chains (R_0) to the tube or pore diameter (D): $\Delta S_{\text{polymer,conf}} \sim -(R_0/D)^2 \sim N/D^2$. On the other hand, Kong and Muthukumar reported that the free energy of a confined non-ideal chain in a nanopore is proportional to $-wN^2/D^3$, where w represents the excluded volume interaction. [17] Moreover, the scaling of the change in entropy on confinement has been hypothesized to depend on the strength of the confinement being proportional to N for the weak confinement regime and N^2 for the strong confinement regime. [18,19]

Based on the equilibrium propagation reaction in background part (see

equation (2.12)), the change in the entropy of propagation between the confined and bulk reactions will depend on the strength of the confinement regime. For weak confinement, no effect is anticipated: $\Delta S_{p,conf} - \Delta S_{p,bulk} \sim [(N+1)-N-1] \sim 0$. On the other hand, for the strong confinement environment, the difference in the entropy of propagation between confined and bulk reactions should be influenced by the chain length: $\Delta S_{p,conf} - \Delta S_{p,bulk} \sim [(N+1)^2 - N^2 - 1] \sim N^1$.

Here, to test these ideas, we polymerize MMA in nanopores and evaluate the effect of nanoconfinement on the polymer/monomer equilibrium using differential scanning calorimetry (DSC). The experimental data are modeled to investigate the changes in thermodynamic properties in a nanoconfined environment.

5.2 Methodology

5.2.1 Materials

The treatments of monomer, initiator and nanoconfined CPG follow the same procedures in Chapter 3 and Chapter 4.

5.2.2 Polymerization

The polymerization of MMA in bulk and in nanoporous confinement was carried out isothermally at temperatures ranging from 60 to 180 °C using a Mettler Toledo differential scanning calorimeter (DSC) as an oven. After a given isothermal reaction, dynamic scans at 10 K/min from room temperature to 200 °C were used to measure any residual heat of reaction. One to three replicate samples were used for

each reaction condition. For reaction temperatures above 100 °C, we were faced with a challenge because the temperature is higher than the boiling point of pure monomer ($T_{b,MMA} = 101$ °C). We initially tried to use pans with o-rings capable of withstanding 24 bars but were unsuccessful. Hence, in order to decrease the vapor pressure of reactant mixture, we partially converted the samples at low a temperature (80 °C) to $x \approx 10\sim 15$ % prior to the polymerization at higher temperature. Thus, two DSC programs were used depending on the reaction temperatures, which are described by one step and two step methods, respectively.

For the one step method shown in Figure 5.2a, a temperature ramp at 100 K/min was applied from room temperature to the specified temperature for polymerization, which ranged from 60 to 140 °C for bulk samples and from 60 to 130 °C for nanoconfined samples. For the two step method shown in Figure 5.2b, the monomer is first reacted at 80 °C for a prespecified time prior to the onset of autoacceleration to form a monomer/polymer mixture and then heated at 100 K/min to the specified temperature from 110 to 180 °C where the equilibrium polymerization is complete.

The conversion of isothermally polymerized MMA is related to heat flow (\dot{Q}) by the equation:

$$x = \frac{1}{\Delta H_p} \int_0^t \dot{Q} dt \quad (5.1)$$

where the average total heat of reaction ΔH_p is 560 J/g obtained from literature reports [20], and 563 ± 12 J/g based on a prior work on the same system, independent of confinement size and surface treatment [13]. The integration is performed over the

entire isothermal history. For polymerization temperatures ranging from 60 to 95 °C, complete polymerization was achieved since a residual heat of reaction was observed after isothermal polymerization for times less than three hours ($\Delta H_{\text{iso}} + \Delta H_{\text{res}} = 560 \pm 7$ J/g). However, we cannot observe any DSC signature for residual heat of reaction for reaction temperature above 100 °C so that we may assume the reaction stopped evolving during isothermal polymerization for times less than half hour. Thus, for polymerization temperature above 100 °C, the total conversion associated with one step method is calculated by the sum of heat of reaction for temperature ramp and isothermal reaction ($\Delta H_{\text{ramp}} + \Delta H_{\text{iso}}$). The conversions associated with two steps are calculated from the heat of reaction for the two isothermal steps ($\Delta H_1 + \Delta H_2$) using equation (5.1) plus the conversion associated with heat of reaction during the temperature ramp between the two steps (ΔH_{ramp}).

Although ΔH_{ramp} is obtained based on the experimental observation for both one and two step method, we can also integrate the following equation to examine the conversion x associated with ΔH_{ramp} for one step method:

$$\frac{dx}{dT} = \frac{k_{\text{eff}} M_0 (1-x)}{\beta} \quad (5.2)$$

where k_{eff} is the effective rate constant from previous work [13], M_0 is the bulk MMA initial concentration, and β is heating rate. Based on the measurements and equation (5.2), for one step method, ΔH_{ramp} is negligible (<1% of ΔH_{P}) for the samples at temperature below 100 °C and ΔH_{ramp} is less than 20 % of ΔH_{P} for all the samples at temperature ranging from 100 °C to 140 °C, and thus, below the onset of autoacceleration prior to reaching the specified polymerization temperature.

The uncertainties of the experiments are based on the weight loss during polymerization at high temperature, which are shown as the error bars for all the data. The weight loss increases as the reaction temperature increases, where the weight loss of bulk samples is lower than that of nanoconfined samples at the same temperature presumably due to the highly reactivity in nanopores. The heat of reaction is measured based on the average weight before and after polymerization. The largest weight loss of bulk is around 20 % at 180 °C, whereas the weight loss of nanoconfined sample is around 40 %. Although the larger weight loss at high temperature seems to cause larger errors, the heat of reaction at second isothermal step only accounts for the small percentage of the equilibrium conversion (i.e. $\Delta H_2 \approx 20\%$ of ΔH_P for bulk, and $\Delta H_2 \approx 1\%$ of ΔH_P for nanopores at $T > 150$ °C). Since we assume apparent increase in weight loss caused by autoacceleration, at high temperature, the error bars indicate the weight loss occurred during temperature ramp. Indium was used to calibrate the enthalpy and the DSC temperature at 10 K/min. For the isothermal condition used to react the samples, an isothermal calibration [24] was performed using indium at 0.1 K/min.

5.3 Results

The Arrhenius plot of equilibrium conversion is shown in Figure 5.3ab. The equilibrium conversion of samples synthesized in bulk decreases as the polymerization temperature increases indicating the depolymerization is favorable at higher temperature, whereas the samples synthesized under nanoconfinement follow the same trends but lower conversions are observed at the same reaction temperature compared

with bulk. Based on equation (2.16), the ΔH_p and ΔS_p can be obtained from slope and intercept by linear fit, where fitting parameters are shown in Table 5.1. The fitting parameters of samples synthesized in hydrophobic and hydrophilic pores are similar within errors suggesting that we may combine all the nanoconfined data to achieve one set of fitting parameters to describe the dependence of conversion on temperature under nanoconfinement, also as shown in Table 5.1. However, the results for best fit in Figure 5.3a show that ΔH_p decreases under nanoconfinement, which is inconsistent with our previous work [13] that heat of reaction for nanoconfined samples is independent of confinement size and approximately equals bulk value. Therefore, we performed another fit by fixing the slope of bulk value for both samples ($\Delta H_p = 56$ kJ/mol) in hydrophobic and hydrophilic pores, as shown in Figure 5.3b.

The dependence of conversion on isothermal temperatures is shown in Figure 5.4 for bulk samples, which are obtained from the one step method (represented by open symbols) and the two step method (represented by solid symbols). The conversions at low temperatures are less than 100 % due to the effect of vitrification. As the reaction temperature approaches the glass transition of neat polymer ($T_{g,p}$), the conversion reaches the max limit of 1.0 and then it decreases as the reaction temperature increases since depolymerization gradually becomes dominant at higher temperatures. In Figure 5.4, the dashed lines are the best fit of equation (2.16) based on bulk data in Figure 5.3a to obtain the $\Delta S_{p,bulk}$ assuming the bulk value of ΔH_p (560 J/g). The model prediction deviates from experimental data below $T_{g,p}$ due to the vitrification effect, which is not described in equation (2.16). The value of $\Delta S_p = -115$

$\pm 1 \text{ J/mol K}^{-1}$ is found to describe the bulk reaction, which is consistent with the value in the literature ($\Delta S_{p,\text{bulk}} = -117 \text{ J/mol K}^{-1}$) [20]. In addition, T_c for the bulk polymerization is $216 \pm 2 \text{ }^\circ\text{C}$, which is also consistent with the value reported in the literature ($T_{c,\text{MMA}} = 220 \text{ }^\circ\text{C}$) [20]. Based on the data and modeling predictions, both the one and two step methods give good results.

The dependence of equilibrium conversion on isothermal temperatures is shown in Figure 5.5 for both bulk and nanoconfined samples, where the open symbols refer to the one step method and the solid symbols refer to the two step method. Similar to the bulk case, the reaction at low temperatures is incomplete ($x < 1.0$) due to the influence of vitrification. In the vicinity of the glass transition of pure polymer, the conversion gradually reaches a maximum value of 1.0 and then it decreases with increasing polymerization temperature due to the effect of depolymerization at high temperature. However, for polymerization temperatures above $T_{g,p}$, the equilibrium conversion of nanoconfined samples is less than that of bulk samples at a given temperature. Although the equilibrium polymerization is performed in both hydrophobic and hydrophilic nanopores with different surface chemistries, we do not observe difference in equilibrium conversion between samples in hydrophilic and hydrophobic pores within the error of the measurements. Considering the bulk data quantitatively described by the model of constant $\Delta S_{p,\text{conf}}$, we first applied the same equation (2.16) to the nanoconfined case assuming the same ΔH_p as in the bulk case; the model (shown as black dashed line) only qualitatively describes the trend (with $\Delta S_{p,\text{conf}} = -124 \pm 1 \text{ J/mol K}^{-1}$).

To further examine the temperature dependence of $\Delta S_{p,conf}$, we note that the difference between the changes in entropy of propagation between confined and bulk polymerizations is simply related to the difference in the equilibrium conversion since the heat of reaction (ΔH_p) is a constant value, independent of various pore size or pore wall chemistry [13]:

$$\Delta S_{p,bulk} - \Delta S_{p,conf} = R \ln \frac{(1-x)_{conf}}{(1-x)_{bulk}} \quad (5.3)$$

Figure 5.6 shows the dependence of $\Delta S_{p,bulk} - \Delta S_{p,conf}$ versus temperature for both one step and two step methods above 110 °C. An exponential fit is assumed to describe the decrease in $\Delta S_{p,conf}$ with increasing temperature, as indicated by the dashed line.

The less negative value of $\Delta S_{p,conf}$ observed at high temperature is presumably due to the reduction of shorter chain lengths resulting in weaker confinement effects.

Considering the scaling of $\Delta S_{p,conf}$, we also plot the $\ln(\Delta S_{p,bulk} - \Delta S_{p,conf})$ against T^{-1} in inset figure of Figure 5.6 to investigate the relationship between $\Delta S_{p,conf}$ and the chain length. As we expected, $\ln(\Delta S_{p,bulk} - \Delta S_{p,conf})$ shows that $\ln \Delta S_{p,conf}$ linearly decreases with decreased reciprocal temperature.

The kinetic chain length (ν) as a function of the reciprocal temperature is shown in the Figure 5.7, which is based on the following equations:

$$R_p = k_p [M \cdot][M] - k_{dp} [M \cdot] \quad (5.4)$$

$$R_t = 2k_t [M \cdot]^2 \quad (5.5)$$

$$\nu = \int \frac{R_p}{R_t} dx = \frac{\frac{x_{eq}}{2} [M]_0 k_p}{2(f k_d k_t [I]_0)^{\frac{1}{2}}} \quad (5.6)$$

where k_p , k_d , k_t are the rate constants for the propagation, dissociation, and termination reactions, respectively, and f is the initiator efficiency. The above derivation assumes that diffusion control and autoacceleration are not important at high reaction temperatures due to the dramatically decreased viscosity (η), which results in a decrease in kinetic chain length. In Figure 5.7, the open symbols represent the experimental data for number-average molecular weight (M_n) of both bulk and nanoconfined samples obtained by GPC [14] divided by the molecular weight of the monomer, whereas the solid symbols are calculated results based on modeling the reaction kinetics [25,26]. The natural logarithm of the kinetic chain length ($\ln v$) linearly decreases as the reciprocal temperature decreases for all the samples as shown in Figure 5.7. However, at high temperature, kinetic chain lengths of samples synthesized in hydrophobic pores and in hydrophilic pores gradually merge, which may suggest that the effect of temperature is stronger than either the confinement effect or the influence of surface chemistry.

Using the temperature dependence for $\Delta S_{p,conf}$ shown in Figure 5.6, in equation (2.16), yields the solid line in Figure 5.5, which well describes the decrease in ceiling temperature in nanopores. The constraint of chain conformation under nanoconfinement results in larger negative $\Delta S_{p,conf}$ causing reduced T_c based on equation (2.17). Based on the fitting parameters shown in Table 5.2 for a nanoconfined model with constant ΔS_p or $\Delta S_p(T)$, the decrease in ceiling temperature is quantified.

5.4 Discussion

At first glance, we expect that both the equilibrium conversion and ceiling temperature undergo pronounced effects upon nanoconfinement in hydrophilic pores so that x_{eq} and T_c are significantly smaller than those values for samples in hydrophobic pores. Since it was reported that PMMA carbonyl group can interact with the silanol group on the hydrophilic pore surface [27] to induce a specific interaction constraining the movement of polymer chains so that the immobilized chain may result in higher magnitude of changes in $\Delta S_{\text{p,conf}}$. However, both experimental data and fitting results show no significant difference in x_{eq} and T_c between samples synthesized in hydrophobic and hydrophilic pores consistent with the strength of the specific interaction being reduced at high reaction temperatures relative to the $k_B T$ (k_B is the Boltzmann constant).

As we described, the $\Delta S_{\text{p,conf}}$ is dependent on chain length, which, in turn, depends on the reaction temperatures by equation (5.6). Since AIBN is small molecule, the decomposition of initiator should not be affected by confinement effect so that k_d is the same value for both samples in hydrophobic and hydrophilic pores. In addition, our previous work on the modeling of PMMA polymerization under nanopores [25,26] revealed that k_t is affected by equilibrium monomer concentration and k_p under nanoconfinement ($k_t = Ak_p[M]_{\text{eq}} + k_{t0}$) [28], where A is a constant number reduced with increasing temperature and k_{t0} is the rate constants of termination reaction in bulk. Thus, to account for the difference in chain length between samples in hydrophobic and hydrophilic pores, we only focus on the

difference in k_p upon various pore surfaces. According to our previous modeling work on reactivity of PMMA polymerization under nanoconfinement [25,26], we find that the difference between k_p of samples in hydrophilic pores and samples in hydrophobic pores ($k_{p,\text{hydrophilic}}^{-1} - k_{p,\text{hydrophobic}}^{-1} = k_{po}^{-1} (1+E/D)^{-1} - k_{po}^{-1}$) is due to the surface catalytic effect (E) by the interaction between PMMA and silanol groups. This surface catalytic effect is a constant that decreases as the reaction temperature increases so that k_p for both pore surfaces will be the same at high temperature where E equals zero, which can be attributed to the reduced strength of specific interaction via hydrogen bonding at high temperature. In general, at high temperature, the effect of nanoconfinement shows no significant difference in k_d , k_t , k_p based on the calculation so that the chain length is similar for samples in hydrophobic and hydrophilic pores.

5.5 Conclusion

The equilibrium polymerization of methyl methacrylate (MMA) synthesized in bulk and nanoscale controlled glass pores (CPG) is investigated by DSC. Both one and two step methods are performed to cover the reaction temperatures ranging from 60 to 180 °C. The equilibrium conversion decreases as the reaction temperature increases due to the effect of depolymerization, whereas nanoconfined samples have pronounced effect. There is no dramatic change for equilibrium conversion between hydrophobic and hydrophilic pores indicating that pore/surface chemistry shows no significant influence on the equilibrium conversion. The equilibrium conversion of bulk samples as a function of temperatures can be quantitatively described in the model by constant $\Delta S_{p,\text{bulk}}$ during chains propagation, which is insufficient to describe

the equilibrium conversion of nanoconfined samples. The discrepancy between bulk and nanoconfined samples is attributed to the reduced chain length with increasing temperature so that we can establish a temperature function to catch the changes in $\Delta S_{p,conf}$ and the corresponding model also quantitatively describe the data of samples synthesized under nanoconfinement. For both case, the ceiling temperature is found to decrease compared with bulk.

References

1. Li XC, King TA, Pallikari-Viras F. "Characteristics of composites based of PMMA modified gel silica glasses" *Journal of Non-Crystalline Solids* 1994;170:243-249.
2. Ng SM, Ogino S, Aida T, Koyano KA, Tatsumi T. "Free radical polymerization within mesoporous zeolite channels" *Macromolecular Rapid Communications* 1997;18:991-996.
3. Kageyama K, Ng SM, Ichikawa H, Aida T. "Macromolecular synthesis using mesoporous zeolites" *Macromolecular Symposia* 2000;157:137-142.
4. Ni XF, Shen ZQ, Yasuda H. "Polymerization of methyl methacrylate with samarocene complex supported on mesoporous silica" *Chinese Chemical Letters* 2001;12:821-822.
5. Kalogeras IM, Vassilikou-Dova A. "Dielectric probe of intermolecular interactions in poly (methyl methacrylate)(PMMA) and PMMA+ SiO₂ matrixes doped with luminescent organics" *Journal of Physical Chemistry B* 2001;105:7651-7662.
6. Kalogeras IM, Neagu ER. "Interplay of surface and confinement effects on the molecular relaxation dynamics of nanoconfined poly(methyl methacrylate) chains" *European Physical Journal E* 2004;14:193-204.
7. Uemura T, Ono Y, Kitagawa K, Kitagawa S. "Radical polymerization of vinyl monomers in porous coordination polymers: Nanochannel size effects on

- reactivity, molecular weight, and stereostructure" *Macromolecules* 2008;41:87-94.
8. Ikeda K, Kida M, Endo K. "Polymerization of methyl methacrylate with radical initiator immobilized on the inside wall of mesoporous silica" *Polymer Journal* 2009;41:672-678.
 9. Uemura T, Ono Y, Hijikata Y, Kitagawa S. "Functionalization of coordination nanochannels for controlling tacticity in radical vinyl polymerization" *Journal of the American Chemical Society* 2010;132:4917-4924.
 10. Zanotto A, Spinella A, Nasillo G, Caponetti E, Luyt AS. "Macro-micro relationship in nanostructured functional composites" *eXPRESS Polymer Letters* 2012;6:410–416.
 11. Ouad K, Djadoun S, Ferfera-Harrar H, Sbirrazzuoli N, Vincent L. "Synthesis and thermal behavior of poly(methyl methacrylate)/Maghnia bentonite nanocomposite prepared at room temperature via in situ polymerization initiated by a new Ni(II) α -benzoinoxime complex" *Journal of Applied Polymer Science* 2011;119:3227–3233.
 12. Moller K, Bein T, Fischer RX. "Entrapment of PMMA polymer strands in micro-and mesoporous materials" *Chemistry of Materials* 1998;10:1841-1852.
 13. Zhao HY, Simon SL. "Methyl methacrylate polymerization in nanoporous confinement" *Polymer* 2011;52:4093-4098.

14. Zhao HY, Yu ZN, Begum F, Hedden RC, Simon SL. "The effect of nanoconfinement on methyl methacrylate polymerization: T_g , molecular weight, and tacticity" *Polymer* 2014;55:4959-4965.
15. Horie K, Mita I, Kambe H. "Calorimetric investigation of polymerization reactions. I. Diffusion-controlled polymerization of methyl methacrylate and styrene" *Journal of Polymer Science Part A-1: Polymer Chemistry* 1968;6:2663-2676.
16. De Gennes PG. *Scaling Concepts in Polymer Physics*. Ithaca, NY: Cornell University Press; 1979.
17. Kong CY, Muthukumar MJ. "Polymer translocation through a nanopore. II. Excluded volume effect" *Journal of Chemical Physics* 2004;120:3460-3466.
18. Sakaue T, Raphael E. "Polymer chains in confined spaces and flow-injection problems: some remarks" *Macromolecules* 2006;39:2621-2628.
19. Cacciuto A, Luijten E. "Self-avoiding flexible polymers under spherical confinement" *Nano Letters* 2006;6:901–905.
20. Odian G. *Principles of Polymerization*. 3rd ed. New York: Wiley; 2004.
21. Kalampounias AG, Andrikopoulos KS, Yannopoulos SN. "'Rounding' of the sulfur living polymerization transition under spatial confinement" *Journal of Chemical Physics* 2003;119:7543-7553.
22. Andrikopoulos KS, Kalampounias AG, Yannopoulos SN. "Confinement effects on liquid–liquid transitions: pore size dependence of sulfur's living polymerization" *Soft Matter* 2011;7:3404–3411.

23. Begum F, Sarker RH, Simon SL. "Modeling Ring/Chain Equilibrium in Nanoconfined Sulfur" *Journal of Physical Chemistry B* 2013;117:3911-3916.
24. Simon SL, Sobieski JW, Plazek DJ. "Volume and enthalpy recovery of polystyrene" *Polymer* 2001;42:2555-2567.
25. Begum F, Zhao HY, Simon SL. "Modeling methyl methacrylate free radical polymerization: Reaction in hydrophilic nanopores" *Polymer* 2012;53:3238-3244.
26. Begum F, Zhao HY, Simon SL. "Modeling methyl methacrylate free radical polymerization: Reaction in hydrophobic nanopores" *Polymer* 2012;53:3261-3268.
27. Keddie JL, Jones RAL, Cory RA. "Interface and surface effects on the glass-transition temperature in thin polymer films" *Faraday Discussions* 1994;98:219-230.
28. Achilias DS, Kiparissides C. "Development of a general mathematical framework for modeling diffusion-controlled free-radical polymerization reactions" *Macromolecules* 1992;25:3739-3750.

Table 5.1. The fitting results for equilibrium conversion as function of inverse temperature for bulk and nanoconfined PMMA

	Bulk	Hydrophobic 13 nm	Hydrophilic 13 nm	Nanoconfined
Best Fit				
$-\Delta H_p$ ($\text{kJ}\cdot\text{mol}^{-1}$)	57.8 ± 8.1	34.3 ± 2.8	34.7 ± 6.6	34.1 ± 3.9
$-\Delta S_p$ ($\text{J}\cdot\text{mol}^{-1}\cdot\text{K}^{-1}$)	118.9 ± 19.3	72.9 ± 6.7	72.3 ± 15.6	71.4 ± 9.4
T_c (°C)	213 ± 12	197 ± 5	207 ± 6	203 ± 10
Constant ΔH_p Fit ($-\Delta H_p = 56 \text{ kJ}\cdot\text{mol}^{-1}$)				
$-\Delta S_p$ ($\text{J}\cdot\text{mol}^{-1}\cdot\text{K}^{-1}$)	114.6 ± 0.9	124.8 ± 1.0	122.7 ± 1.2	123.6 ± 0.8
T_c (°C)	216 ± 2	175 ± 2	183 ± 2	180 ± 1

Table 5.2. Values for ΔS_p assuming $\Delta H_p = -56$ kJ/mol; and a function of temperature ($\Delta S_p(T)$)

	Bulk	Nanoconfined $\Delta S_p = \text{constant}$	Nanoconfined $\Delta S_p = f(T)$
$-\Delta S_p$ ($\text{J}\cdot\text{mol}^{-1}\cdot\text{K}^{-1}$)	114.6 ± 0.9	123.7 ± 0.8	$-114.6 - 5.0 \cdot \exp(-72.6 \cdot T^{-1})$
T_c ($^{\circ}\text{C}$)	216 ± 2	180 ± 2	190 ± 7

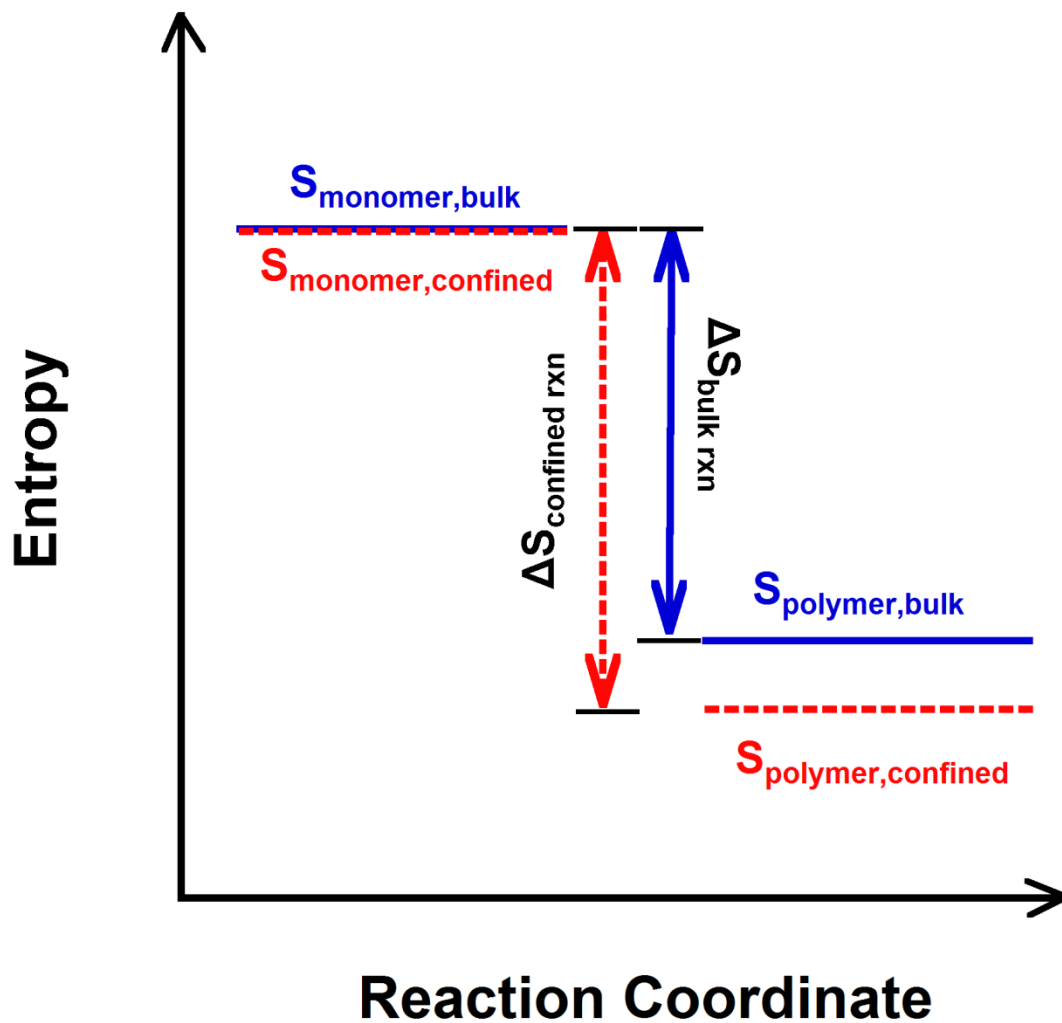


Figure 5.1. Schematic plot to show how entropy changes under nanoconfinement. Solid lines represent the entropy in bulk and the dashed lines represent the entropy in nanoconfined system.

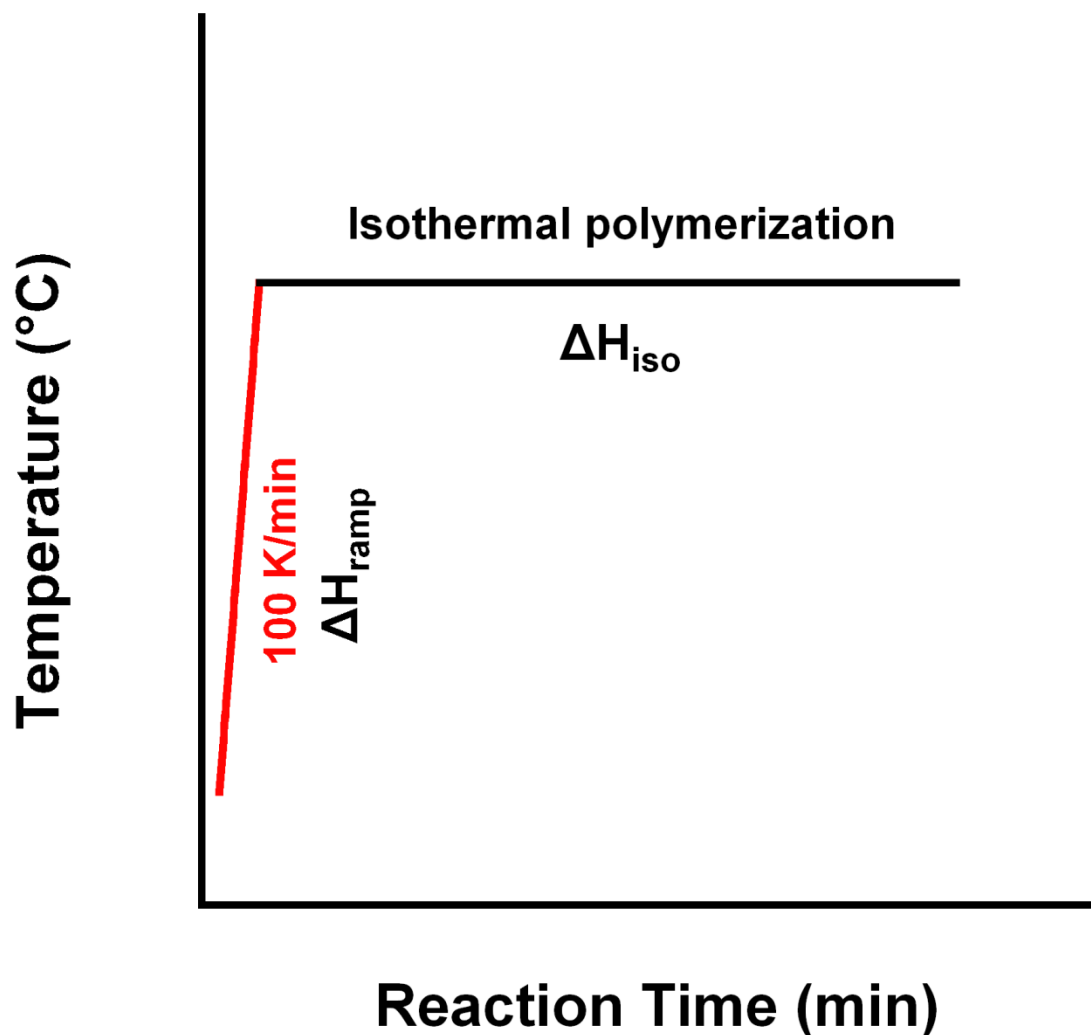


Figure 5.2a. Schematic of one step method to investigate the equilibrium reaction at temperatures from 60 to 140 °C for bulk polymerization and from 60 to 130 °C for nanoconfined polymerization.

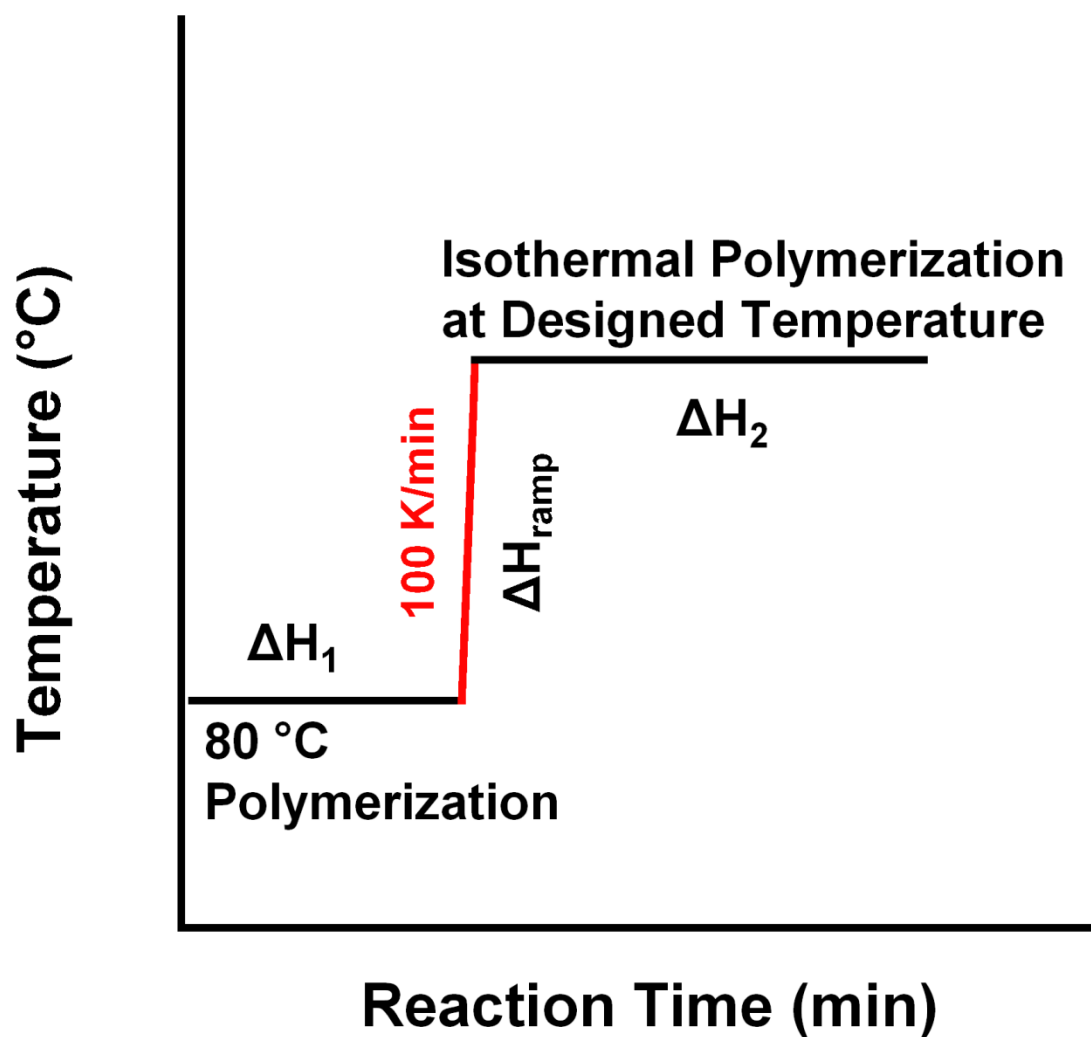


Figure 5.2b. Schematic of two step method to investigate the equilibrium reaction at higher temperature.

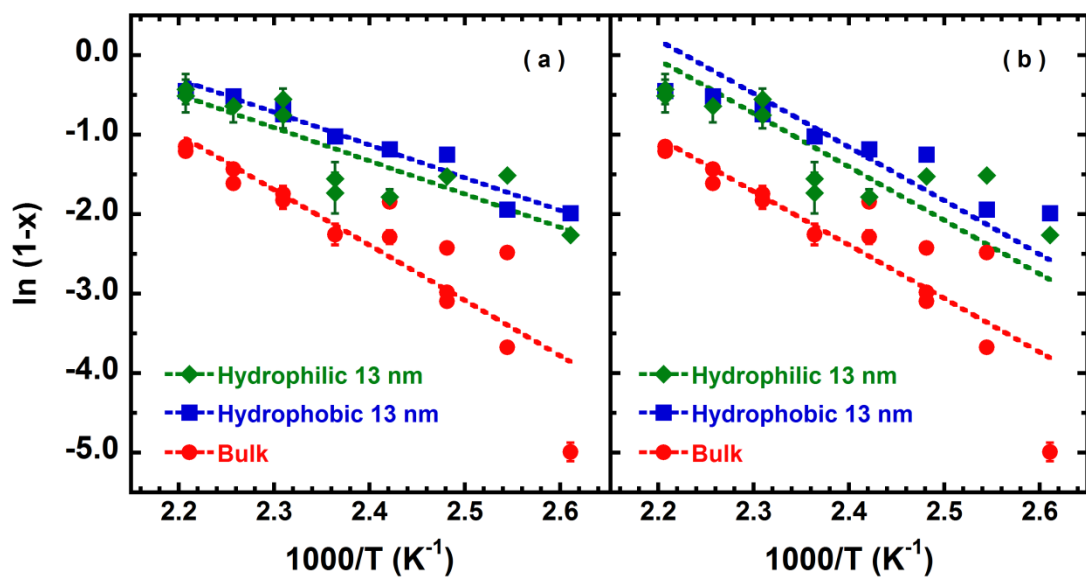


Figure 5.3ab. The equilibrium conversion as a function of the reciprocal of polymerization temperature. Dashed lines represent the linear fitting results, where Figure 5.3a is the best fit and Figure 5.3b is the fixed slope fit.

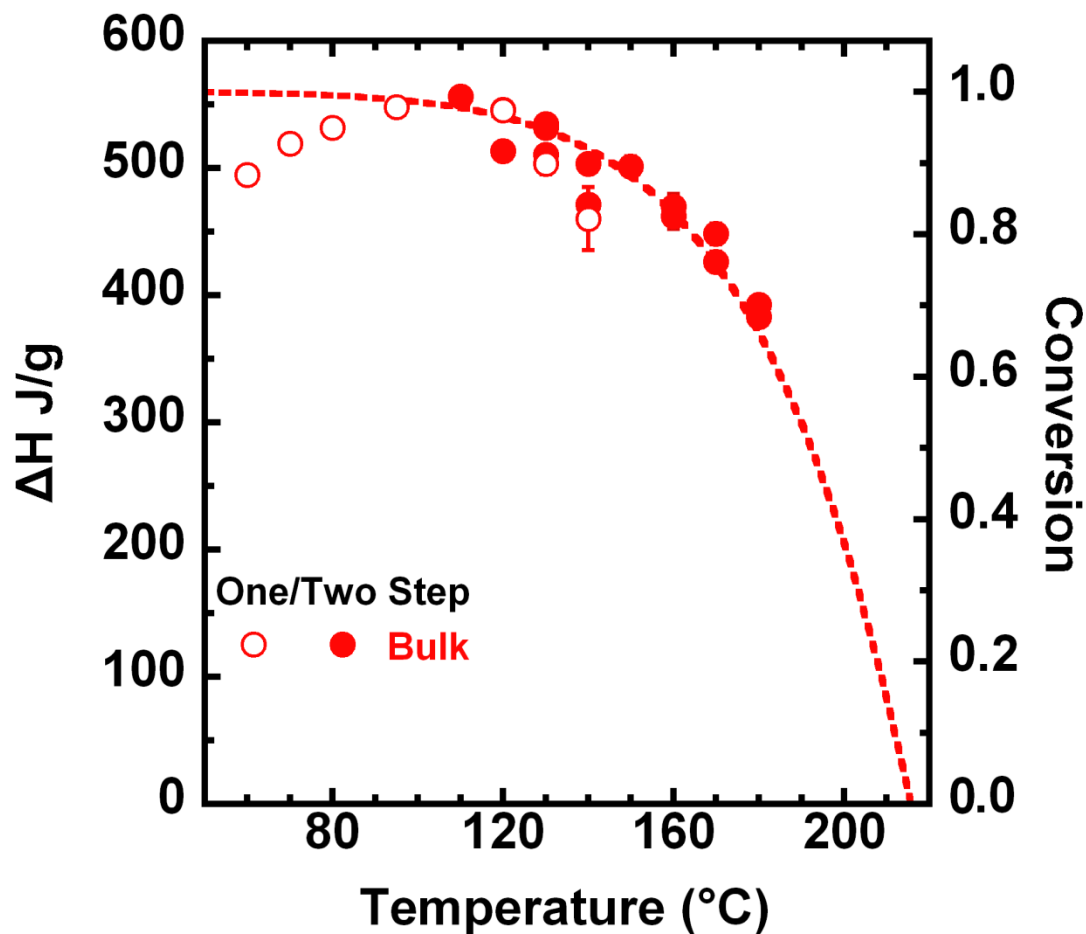


Figure 5.4. The heat of reaction and conversion as a function of isothermal temperature for bulk using one step (open symbols) and two step (solid symbols) methods. The dashed lines are based on the equation (2.16) using constant value of ΔH_p of bulk value (-56 kJ/mol).

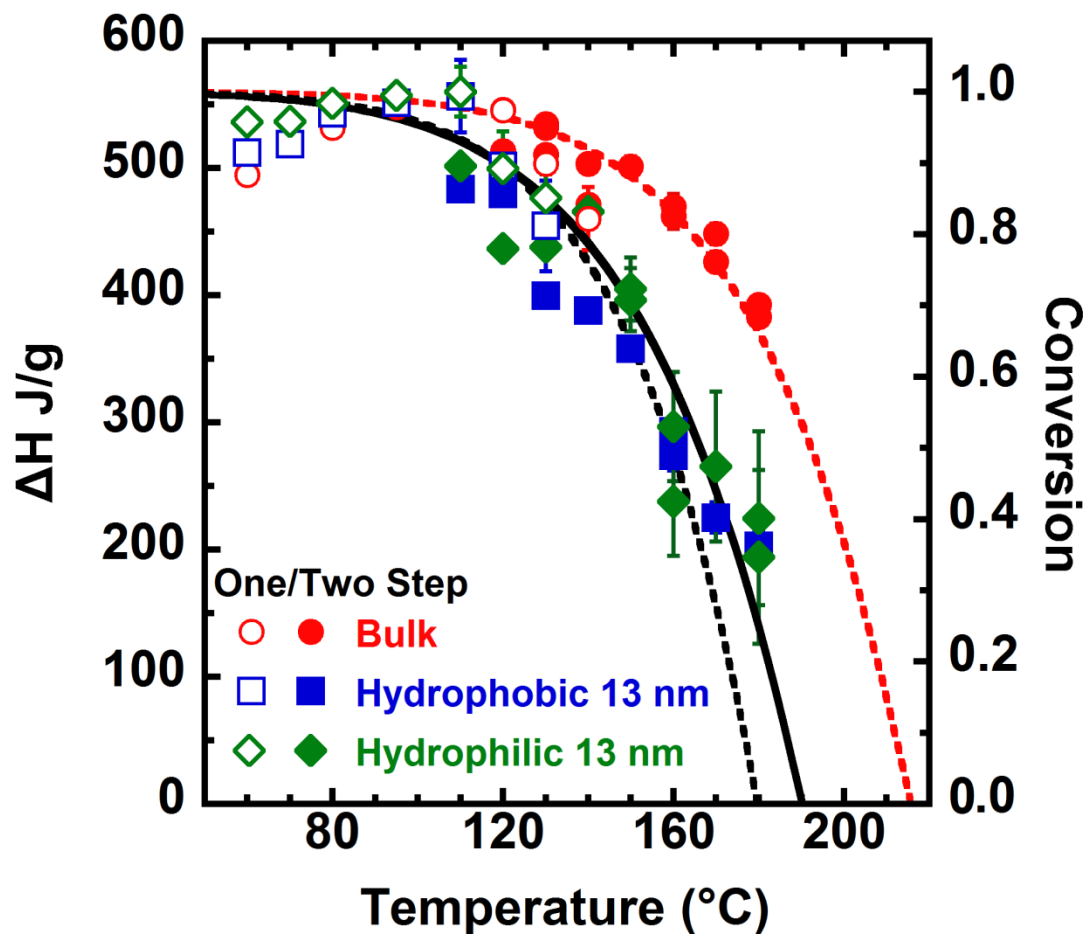


Figure 5.5. The heat of reaction and conversion as a function of isothermal temperature for both bulk and nanoconfined samples using one step (open symbols) and two step (solid symbols) methods. The dashed lines are based on the equation (2.16) using constant value of ΔH_p of bulk value (-56 kJ/mol) and the solid line is the exponential model using ΔS_p as function of temperature.

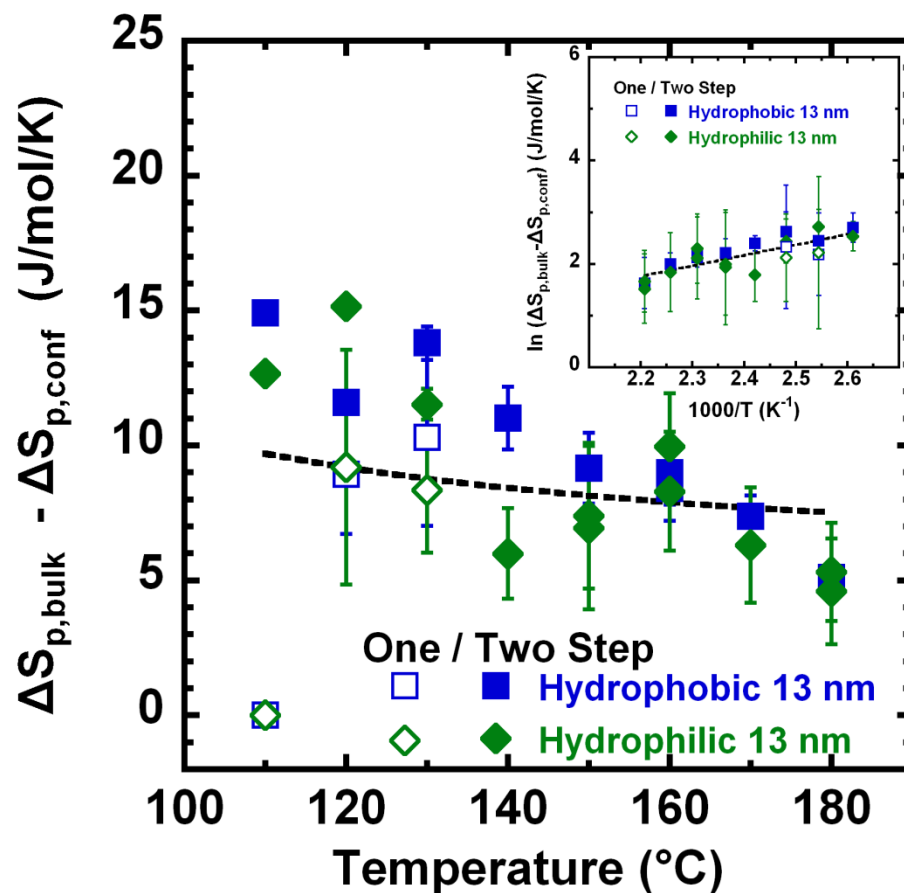


Figure 5.6. The difference between the entropy for the propagation reaction of bulk samples and nanoconfined samples as a function of polymerization temperature. Open symbols represent data from one step method above 110 °C and solid symbols represent data from two step method. Dashed line represents the exponential fitting results. The inset shows $[\ln(\Delta S_{p,bulk} - \Delta S_{p,conf})]$ against the reciprocal temperature. Dashed line represents the linear fitting results.

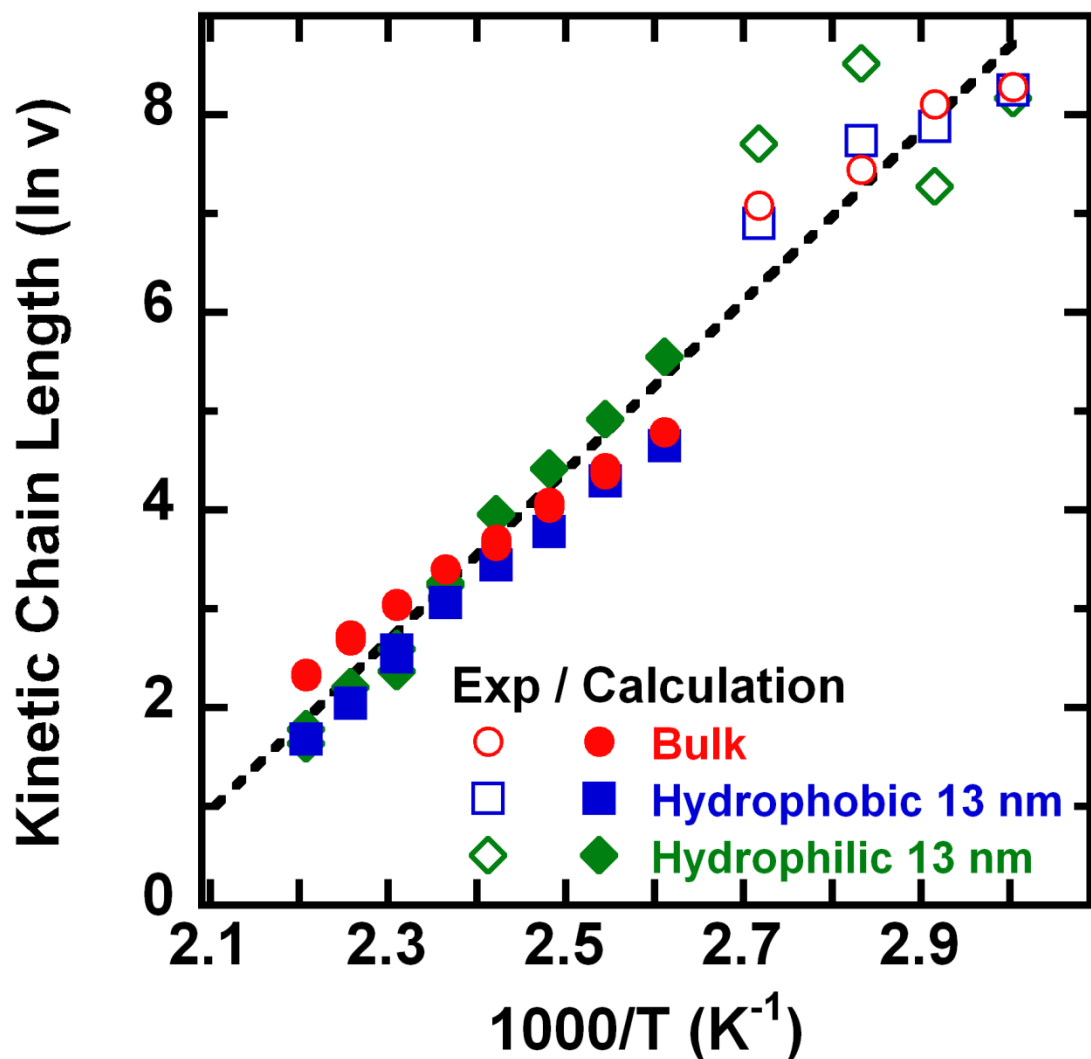


Figure 5.7. The kinetic chain length changes ($\ln v$) with the reciprocal temperatures based on equation (5.6). Open symbols represent chain length data from the experimental number average molecular weight by the ratio of M_n/M_0 [14]. Solid symbols represent chain length data from the calculated results based on the equations from previous work [25,26]. Dashed line represents the linear fitting results.

CHAPTER 6

THE KINETICS OF THE GLASS TRANSITION AND PHYSICAL AGING IN GERMANIUM SELENIDE GLASSES

6.1 Introduction

Binary alloys in the system Ge-Se have been considered in the literature as model materials for understanding the structure-property relationships in chalcogenide glasses. The Se atoms in these glasses are twofold coordinated, whereas the Ge atoms are tetrahedrally coordinated. Consequently the structure of Se-rich germanium selenide glasses is dominated by floppy Se-Se-Se chains with low glass transition temperatures T_g , whereas addition of Ge results in cross-linking of these chains and the formation of a rigid network of corner- and edge-shared GeSe_4 tetrahedra with high T_g . This topological diversity within a single glass forming system has made these glasses ideal for studying the influence of topological constraints on the compositional variation of various physical properties in covalently bonded amorphous materials. It has been argued in the literature that a wide range of physical properties of these glasses would be predominantly controlled by the degree of connectivity of the network as expressed by the average coordination number r_c . [1,2] It can be shown on the basis of the theory of constraint counting that in three dimensions there exists a critical value of $r_c = 2.4$, also known as the rigidity percolation threshold, where the network undergoes a floppy-to-rigid transition, since at this point the number of constraints per atom equals the number of degrees of freedom [1,2]. Ge-Se alloys satisfy this condition at the composition $\text{Ge}_{20}\text{Se}_{80}$ and

show the best glass forming ability near this composition, without significant defects [1-3].

Chalcogenide glasses have found wide ranging applications in photonics and remote sensing due to their low phonon energy, high refractive index, strong optical nonlinearity, and wide transparency range in the infrared range [4,5]. However, because these materials are glasses, they are thermodynamically unstable and changes in properties with physical aging must be considered in product design [5,6]. An exciting new development in this field has been proposed, the intermediate phase, which is associated with a stress-free self-organized system where the degrees of freedom approximately equal the number of constraints near $r_c = 2.4$. Glasses with compositions in the vicinity of the intermediate phase have been suggested to show physical stability at room temperature and a lack of physical aging [7-9] based on results from conventional [10-13] and temperature-modulated [9,14-16] differential scanning calorimetry (DSC and TMDSC, respectively). A related minimization in non-reversing heat flow is also observed on heating in TMDSC after melt quenching to the glassy state [9,17-23].

The lack of physical aging has been attributed to an absence in stress in the intermediate phase compositions [3,8, 24-26], but the interpretation of experimental results has also been criticized [6] due to the use of TMDSC with relatively short aging times. In addition, Elabbar et al. [27] and Golovchak et al. [12,16] reported that significant physical aging occurs after 19+ years at room temperature for arsenic selenide glasses including for compositions near $r_c = 2.4$ and, thus challenged the

existence of the intermediate phase. More recently, Golovchak et al. [28] reported aging on a timescale of days when the aging temperature is within approximately 90 °C of the glass transition temperature for $\text{As}_{40}\text{Se}_{60}$ ($r_c = 2.4$). Yang et al. [29] also concluded that the intermediate phase did not exist based on observed extrema in density, moduli, and Poisson's ratio near $r_c = 2.4$ for $\text{As}_x\text{Se}_{100-x}$ glasses. Furthermore, TMDSC, which was used in some studies postulating the existence of an intermediate, has limitations for measuring the enthalpy recovery associated with physical aging [30-33].

It is well known that the time scale to investigate physical aging depends on the distance from T_g , as has been shown, for example, in DSC and dilatometric work on amorphous selenium. [34-36] Since the T_g of chalcogenide glasses changes with composition, measuring physical aging at a single temperature, as was done in previous works [9,12-15], is hypothesized by us to lead to problems in interpreting the data. Hence, in this work, we examine the T_g and enthalpy recovery of Ge-Se chalcogenide glasses as a function of composition using aging temperatures that are at a fixed absolute distance below T_g ; we use a fixed distance since the "universal" Williams-Landel-Ferry (WLF) equation [37] suggests that relaxation times should vary with the quantity $T-T_g$. We show that, in fact, all of the chalcogenide glasses studied here, physically age as might be expected. The implication for the existence of the Boolchand intermediate phase is discussed.

6.2 Methodology

6.2.1 Materials Preparation

$\text{Ge}_x\text{Se}_{100-x}$ glasses with $5 \leq x \leq 30$ were synthesized in 10 to 20 g batches by melting mixtures of the constituent elements Ge and Se with $\geq 99.995\%$ purity (metals basis) in evacuated (10^{-6} torr) and flame sealed fused silica ampoules (8 mm I.D., 11 mm O.D.) at temperatures ranging between 1000 and 1200 K for 24 to 48 h in a rocking furnace. The synthesis of Ge-Se glasses are collaborative work performed by Professor Sabyasachi Sen's group from UC Davis. The ampoules were quenched in water and subsequently annealed for 1 h at the respective glass transition temperatures. We have also studied amorphous selenium that was purchased from Sigma-Aldrich (purity $\geq 99.999\%$). The average coordination numbers r_c of these chalcogenide glasses are calculated using the following equation:

$$r_c = \frac{4x + 2(100 - x)}{100} = 2(1 + x/100) \quad (6.1)$$

where x is the atom percent germanium in the $\text{Ge}_x\text{Se}_{100-x}$ alloy. For our samples, r_c ranges from 2.0 for amorphous selenium to 2.6 for $\text{Ge}_{30}\text{Se}_{70}$ glass, as shown in Table 6.1.

6.2.2 DSC Measurements

A Perkin-Elmer Pyris 1 differential scanning calorimetry (DSC) with an ethylene glycol cooling system and nitrogen purge gas was employed to measure the absolute heat capacity, the kinetics associated with the glass transition, and the enthalpy recovery during physical aging. Sample size ranged from 5 to 25 mg. The

sample weight was checked before and after the DSC runs and no obvious weight loss (< 3%) was found for the work reported here. Temperature calibration on the heating step was checked using indium on heating at 10 and 0.1 K/min.

Three types of experiments were performed. In the first, the step-scan method was used to measure the absolute heat capacity and consisted of multiple temperature ramp/isothermal steps. Step sizes were 2 K, holds were 0.8 min at each temperature, and a 10 K/min heating rate was used between sequential isothermal hold temperatures. Measurements were performed on heating after first cooling the samples from $T_g + 30$ K to below T_g at 30 K/min, except for the selenium sample which was cooled from 503 K (229.8 °C), above its melting point (~ 490 K); the relatively high cooling rate of 30 K/min was used to minimize enthalpy overshoots on the subsequent heating scan. The absolute heat capacity is obtained from the heat flow rate (\dot{Q}) observed during the isothermal hold:

$$C_p = k \frac{\int \dot{Q} dt}{m \Delta T} \quad (6.2)$$

where k is the calibration constant, m is the mass of the sample, and ΔT is the temperature step of 2 K between isothermal hold temperatures. The calibration constant was obtained using the step-scan method for two runs, one for sapphire and the other using empty sample pans; in all runs, the sample and reference pans are identical in weight (within 0.01 mg). The standard deviation for multiple runs for selenium is less than ± 2.0 %. The value of T_g was obtained from the absolute C_p versus temperature data using the half-height method, i.e., at the temperature at which C_p attains a value halfway between the extrapolated liquid and glassy C_p lines, the

latter of which are shown later. The absolute heat capacity measurements are performed by Dr. Yung Koh.

In the second type of experiment, the limiting fictive temperature (T_f') was obtained from heating scans at 10 K/min after cooling at a specified rate using Moynihan's method [38]:

$$\int_{T_f'}^{T_g} (C_{pl} - C_{pg}) dT = \int_{T_g}^{T_g} (C_p - C_{pg}) dT \quad (6.3)$$

T_f' is only a function of cooling rate, and it is equivalent within 1 K to the glass transition temperature (T_g) that would be measured on cooling at the same rate [39,40]; hence, in the text, we often refer to T_f' as T_g .

Finally, the enthalpy change after isothermal physical aging was determined as a function of aging time. A schematic of the temperature history is shown in Figure 6.1. Samples were held at a temperature 40 K above T_g for several minutes to eliminate the effect of prior thermal history and then cooled at 10 K/min to the aging temperature T_a , which was nominally 5, 10, and 15 K below T_g ; exact values are listed in Table 6.2. The samples were maintained at the aging temperature for prespecified aging times ranging from 3 to 10,000 minutes, and after aging, samples were cooled at 10 K/min to 80 K below T_g . A subsequent heating scan at 10 K/min to 40 K above T_g provides the data for the aged samples. After every aged scan, the samples were cooled at 10 K/min and then a heating scan was performed at 10 K/min to obtain an unaged scan. The change in enthalpy that occurred during aging, ΔH_a , is obtained by comparing aged and unaged scans following the method of Petrie [41]. It is assumed in this method that the amount of relaxation that occurs during the cooling step from

T_a to 80 K below T_g is the same, independent of the degree of aging. All unaged curves superpose, indicating the absence of any chemical changes over the course of the experiments. Two to four replicate runs were made and the average with standard deviation is shown in the results.

6.3 Results

The absolute heat capacity versus temperature behavior for the germanium selenide glasses is shown in Figure 6.2. The glass transition shifts to higher temperatures as the germanium content increases, consistent with the increase in branchpoint density and network structure as the average coordination number increases. Both glass and liquid lines change approximately linearly with temperature, as shown by the dashed lines, with the glass heat capacity increasing with increasing temperature and the liquid heat capacity decreasing with increasing temperature. The increase in absolute heat capacity as a function of temperature along the glass line for selenium has been attributed to the increase of skeletal and group vibrations and free volume as the temperature increases [42,43]. On the other hand, the decrease in the absolute heat capacity in the liquid state is attributed to the normal decrease of the hole contribution with temperature which cannot be compensated, in these materials, by the increasing heat capacity associated with skeletal vibrations [43]. It had been suggested that the ring/chain equilibrium in selenium plays a role in the decrease in C_p with increasing temperature in the liquid state [42]. However, this scenario is not tenable since selenium rings are not expected in germanium selenides as germanium

content increases, and furthermore, several groups including one of us have reported data suggesting few if any rings exist in amorphous selenium [44-46].

In addition to the increase in T_g with germanium content, the value of the step change in heat capacity at the glass transition (ΔC_p) decreases as the average coordination number increases as shown in Figure 6.2. There is no evidence that the value of ΔC_p goes through a minimum near a coordination number of 2.4 as has been reported in the literature [8,20,21], especially since the liquid and glass heat capacities seem to be independent of germanium content within the error of our measurements such that the difference between the two decreases with increasing temperature. On the other hand, the glass transition becomes broader as germanium content increases to $r_c = 2.45$ and then the breadth (as quantified by the difference between transition onset and end points [47]) narrows at higher coordination numbers. The broadening is attributed to an increase in the distribution of relaxation times from those only associated with selenium chains at $r_c = 2.0$ to those associated with a range of selenium chain lengths between the germanium branching or crosslinking points. As germanium content increases, the distribution of selenium chain lengths between germanium atoms increases and then decreases, and the breadth in the glass transition follows.

With respect to the data shown in Figure 6.2, our C_p data measured for selenium are 10 % lower than the suggested C_p values compiled by Gaur et al. [42]. The reason for the discrepancy is not clear, but we note that there are several sets of data in the literature which give values within 3% of ours [48-50].

The absolute heat capacity data shown in Figure 6.2 give information concerning T_g as a function of glass composition, but they do not provide information concerning the kinetics associated with the glass transition. We obtain this information from DSC heating scans made after cooling at various rates. Such scans are shown in Figure 6.3 for all samples after cooling at 10 and 0.1 K/min. To facilitate comparison, we plot the normalized heat capacity (C_{pN}) defined as

$$C_{pN} = \frac{C_p - C_{pg}}{C_{pl} - C_{pg}} \quad (6.4)$$

where C_{pg} and C_{pl} are the heat capacities in the glassy and liquid states, respectively. For a given glass composition, the height of the enthalpy overshoot increases as the cooling rate decreases, as is expected [51]. Slower cooling results in lower volume, enthalpy, and mobility in the glassy state at a given temperature, and consequently, the slowly cooled samples must be heated to a higher temperatures before their mobility increases enough to allow the material to recover its equilibrium liquid density; the result is a shift in the enthalpy overshoot to higher temperatures and an increase in the area under the overshoot with decreasing cooling rate. As germanium content increases from $r_c = 2.0$ to 2.45, the glass transition temperature and breadth increase, consistent with the absolute heat capacity results shown in Figure 6.2, and in addition, the height of the overshoot correspondingly decreases. A slight narrowing may occur from $r_c = 2.45$ to 2.60.

The glass transition temperature and change in heat capacity at the transition (ΔC_p) are plotted as a function of r_c in Figure 6.4, where the open symbols are from the step scan results and the filled symbols are from the conventional DSC data for a

cooling rate of 10 K/min. T_g increases with increasing germanium composition and ranges from 308.2 K (35.0 °C) for pure selenium ($r_c = 2.0$) to 577.6 K (304.4 °C) for $\text{Ge}_{30}\text{Se}_{70}$ ($r_c = 2.6$) reflecting the increase in branchpoints and network structure. A relationship between T_g and the crosslink density X was developed by DiMarzio [52]:

$$T_g = T_{g0}/(1 - KX) \quad (6.5)$$

where T_{g0} is the glass transition temperature of the linear chain, i.e., pure selenium in our case, and the constant K incorporates the effects of crosslinks. Sreeram and coworkers [53] recognized that the crosslink density is simply related to the germanium content, giving T_g as a function of average coordination number:

$$T_g(r) = T_{g0}/[1 - K(r^c/2 - 1)] \quad (6.6)$$

For our data, the fitting parameter K is 1.56 ± 0.01 , which is consistent with the value of 1.5 from Sreeram's work [53]. The expression well describes the data, as shown in Figure 6.4, and is more appropriate than assuming that T_g linearly depends on coordination number with a dependence that varies with composition [54]. On the other hand as is also shown in Figure 6.4, ΔC_p decreases as the average coordination number increases such that the more rigid structure has smaller ΔC_p . Assuming that ΔC_p is linearly related to T_g since to a first approximation, the liquid and glassy lines for the various germanium-selenide materials are independent of composition (as shown in Figure 6.2), we can relate ΔC_p to r_c :

$$\begin{aligned} \Delta C_p &= \Delta C_{p0} + b(T_g - T_{g0}) \\ &= \Delta C_{p0} + bT_{g0} \left(\frac{K(\frac{r_c}{2} - 1)}{1 - K(\frac{r_c}{2} - 1)} \right) \end{aligned} \quad (6.7)$$

where ΔC_{p0} is the change in heat capacity at T_{g0} for pure selenium. The fitting parameter b has a value of 0.00025, consistent with the value of $d\Delta C_p/dT$ from Figure 6.2. Within the scatter of data, the change of heat capacity monotonically decreases as the germanium content increases, and the data are well described by equation (6.7). No minimum in ΔC_p versus r_c is observed.

As shown in Figure 6.3, the kinetics associated with the glass transition, and in particular the enthalpy overshoots at T_g , change as germanium content increases. We quantify this effect by plotting the limiting fictive temperature (T_f' , which is equivalent to T_g for a given cooling rate [39,40]) as a function of the logarithm of the cooling rate q in Figure 6.5. For ease of comparison, we plot the difference in the T_f' value relative to the reference value that is obtained after cooling at 10 K/min. The slope $dT_f'/d\log q$ increases with increasing average coordination number going from approximately 3.3 K/decade for amorphous Se ($r_c = 2.0$) to 11.3 K/decade for $\text{Ge}_{30}\text{Se}_{70}$ ($r_c = 2.6$). From the slope of the limiting fictive temperature versus logarithmic cooling rate, the fragility (m) [55] can be obtained using the following relation:

$$m = \frac{d\log \tau}{d(T_g/T)} = T_{f\text{ref}}' \left(\frac{d\log q}{dT_f'} \right) \quad (6.8)$$

where τ is the relaxation time, and $T_{f\text{ref}}'$ is the reference fictive temperature at a cooling rate of 10 K/min. The apparent normalized activation energy $\Delta h/R$ can also be related to the cooling rate dependence of T_f' :

$$\frac{\Delta h}{R} = - \frac{d\ln q}{d(1/T_f')} = 2.303 T_{f\text{ref}}'^2 \left(\frac{d\log q}{dT_f'} \right) \quad (6.9)$$

The values for m and $\Delta h/R$ are listed in Table 6.1 and indicate that the Ge-Se glasses become stronger, in the Angell sense [55], as germanium content increases. Both m and $\Delta h/R$ show a minimum as a function of germanium content near $r_c = 2.4$.

However, we do not believe that these minima are reflective of any special aging or relaxation behavior near $r_c = 2.4$. Rather, the minima simply arise from competition between $T_{f' \text{ref}}$ monotonically increasing and $d \log q / dT_f'$ monotonically decreasing as the average coordination number r_c increases.

Representative DSC heating scans as a function of aging time for an aging temperature nominally 15 K below T_g are shown in Figure 6.6 for samples of different composition. The enthalpy overshoot peaks grow and shift to higher temperatures as aging time increases, similar to the results in Figure 6.3 with decreasing cooling rate. Thus, the enthalpy loss that occurs during aging increases until the equilibrium is reached; at equilibrium the heating scans stop evolving, as nominally shown by the two scans at longest times for each sample. It is also important to observe the effect of the breadth of the transition on the DSC scans after aging: as T_g broadens with increasing r_c , the enthalpy overshoot peak height decreases and the difference between aged and unaged ($t=0$) curves occurs over a wider temperature range.

The enthalpy loss on aging (ΔH_a) as a function of the logarithm of the isothermal aging time is shown in Figure 6.7 for aging temperatures nominally 5, 10, and 15 K below T_g based on data similar to that shown in Figure 6.6. The enthalpy loss on aging increases with increasing aging time and levels off once equilibrium is reached at a value termed $\Delta H_{a\infty}$. As aging temperatures decrease from the top to

bottom panels, the time required to reach equilibrium increases. The time scale will be quantified later but seems to also increase with decreasing germanium content at the lowest aging temperatures.

The equilibrium change in enthalpy is a function of the distance between the aging temperature and glass transition temperatures. To a first approximation,

$$\Delta H_{a\infty} = \Delta C_p (T_{f,\text{unaged}} - T_a) \quad (6.10)$$

where ΔC_p is the step in the heat capacity jump between glassy and liquid states at T_g , $T_{f,\text{unaged}}$ is the fictive temperature of unaged samples (equal to T_g obtained on cooling at 10 K/min), and T_a is the isothermal aging temperature. We note that the values of ΔC_p are small for the chalcogenide glasses, ranging from approximately 0.16 to 0.09 J g⁻¹K⁻¹ for pure selenium and Ge₃₀Se₇₀ glasses, respectively. These values of ΔC_p , which are three to four times smaller than ΔC_p in organic glass-formers, result in decreased sensitivity in enthalpy recovery measurements for the Ge-Se alloys studied. In addition, the breadth of the transition at high germanium content also introduces error into the measurements. Nonetheless, there is no evidence that any of the Ge-Se compositions studied show a lack of physical aging. Rather, the evolution of the enthalpy shown in Figure 6.7 indicates that all of the Ge-Se glasses show the expected aging response.

Interestingly $\Delta H_{a\infty}$ values from Figure 6.7 are less than that predicted by equation (6.10), as shown in Figure 6.8 where $\Delta H_{a\infty}/\Delta C_p$ is plotted as a function of the difference between reference fictive temperature and aging temperature. It should be noted that equation (6.10) is an approximation in that it does not account for relaxation

on cooling through the transition [56], but this should primarily affect $\Delta H_{a\infty}$ at the highest aging temperatures. In contrast, at the lowest two aging temperatures, we observe that data deviate from the expectation with the observed $\Delta H_{a\infty}$ being less than that predicted by equation (6.10). In fictive temperature terms, equilibrium appears to have been reached when the fictive temperature T_f is 1-4 K above T_a for $T_a = T_g - 10$ K and when T_f is 2-6 K above T_a when $T_a = T_g - 15$ K. Although this observation is consistent with the liquid line not being reached at equilibrium [57-60], we and others have provided evidence arguing against this interpretation [56,61]. Whether the problem is related to the difficulty in measuring physical aging in these systems (due to the small ΔC_p values and broad transitions at high germanium content) is not clear. We did also calculate T_f of the aged curves using Moynihan's method and then obtained $\Delta H_{a\infty}/\Delta C_p = T_f - T_a$; the results are up to 3 K higher than using Petrie's method but still fall below the line predicted by equation (6.10) for the two lower aging temperature samples.

In order to quantify the kinetics associated with physical aging, the enthalpy change data are fit to the Kohlrausch-William-Watts (KWW) [62,63] function:

$$\Delta H_a(t) = \Delta H_{a\infty} \left(1 - \exp \left\{ - \left(\frac{t}{\tau} \right)^\beta \right\} \right) \quad (6.11)$$

where t is the aging time during the isothermal aging process, τ is a fitting parameter which accounts for characteristic relaxation time, and β is a fitting parameter which accounts for nonexponential and nonlinear relaxation. This equation is empirical and does not account for the change of τ during aging. Nevertheless, it has been shown to allow quantification of the time required to reach equilibrium [64] and to well describe

the data, as shown by the dashed lines in Figure 6.7. We note that although the TNM model [65-67] is based on a more physically reasonable picture, it is unable to describe the data in Figure 6.7 using ΔC_p from experiments due to the fact that equation (6.10) does not adequately reflect the experimental results.

The kinetics of physical aging can be characterized by both the time required to reach equilibrium and by the rate of aging. The latter is obtained from the slope of the linear region in enthalpy versus logarithmic time data, as in previous research [68,69]:

$$R_a = d\Delta H_a / d\log t \quad (6.12)$$

The aging rate R_a is plotted in Figure 6.9 as a function of the average coordination number r_c . The rate of aging decreases slightly within increasing germanium content, and for the temperature range examined, it increases with decreasing aging temperature, as shown in the inset in Figure 6.9. We note that in the vicinity of glass transition temperature, the aging rate does not necessarily reflect the relaxation time. For example, very near T_g , the low aging rate is indicative of the fact that the glass is close to equilibrium resulting in a smaller driving force; in addition, the fast relaxation at aging temperatures very near T_g makes it difficult to capture the linear region of the ΔH_a versus $\log t$ curve.

The dependence of the time required to reach equilibrium t_∞ on the germanium content in these glasses is plotted in Figure 6.10. The kinetics of enthalpy recovery is strongly influenced by the aging temperature such that at lower aging temperatures, longer times are required for the glasses to evolve to equilibrium. This should be

contrasted with the fact that the aging rates increase as aging temperature decreases. The time required to reach equilibrium is also found to decrease within increasing germanium content and this observation can be explained by the change in fragility with composition. The inset shows a schematic of the Angell plot [55] and a modest extrapolation of the equilibrium relaxation time at temperatures below T_g at the far right. For $T_g/T \geq 1$, the more fragile compositions are expected to have longer relaxation times, in agreement with the experimental observation. Consistent with this explanation is the data of Figure 6.5, which show T_f' versus the logarithm of the cooling rate ($\log q$), the latter of which is inversely proportion to $-\log \tau$; for example, to obtain T_f' 10 K below $T_{f'_{ref}}$ requires a higher cooling rate as r_c increases indicating that the relaxation time decreases with increasing Ge content and as fragility decreases.

6.4 Discussion

The glassy state is a thermodynamic unstable state such that glasses spontaneously evolve towards equilibrium. The driving force for this process is proportional to the distance between T_a and T_g , and the time required to reach equilibrium exponentially increases with increasing value of $T_g - T_a$ such that, for sufficiently fragile compositions, the time required to reach equilibrium can extend to millennia if $T_g - T_a \geq 30$ K [70]. For pure selenium [34] and low germanium content Ge-Se alloys [71], equilibrium is only observed on normal laboratory time scales when T_a is less than 10 K below T_g . Here, we showed that for stronger glasses, in the Angell sense, with higher germanium content, equilibrium seems to be achieved in

one week even at aging temperatures 15 K below T_g . However, all of our germanium selenide glasses age and the results are consistent with the theoretical expectation.

The non-aging ability described by Boolchand and coworkers depicts the picture that glasses do not undergo aging in the thermally reversing window near an average coordination number of 2.4. Their ideas are based primarily on short term and long term aging at room temperature, which for samples with high average coordination numbers is far from their glass transition temperatures.[9,11-15] Other evidence for the Boolchand non-aging intermediate phase is a minimum in the amount of relaxation that occurs during quenching from the liquid state [8,17,54,72-74]. Since the amount of relaxation is directly related to the cooling rate and the breadth of the transition over which relaxation occurs, one might anticipate more relaxation on quenching for low T_g materials since at low temperatures, the rate of free cooling will be lower. Similarly for materials with broad transitions, such as those showing large values of $dT_f'/d\log q$, one expects more relaxation during the quench through T_g . Consequently, a minimum in the amount of relaxation during a quench from the liquid as a function of average coordination number is not inconsistent with the fact that all of these materials age.

Our data clearly show that it is problematic to interpret physical aging experiments performed at room temperature for materials with widely differing T_g values since the aging rate and associated kinetics depends on the distance $T_g - T_a$. We suggest that the literature reports of a lack of aging at room temperature for high T_g chalcogenide glasses [7-24] can be directly attributed to the large distance between the

aging temperature and the glass transition temperature and not to the existence of a stable, “non-aging” intermediate phase. Our results also provide an explanation for the problems of interpreting relaxation during a free quench since the degree of relaxation will depend on both the cooling rate through T_g and the breadth of the transition.

6.5 Conclusion

The glass transition temperature and enthalpy recovery of a series of germanium selenide glasses is investigated using conventional DSC. T_g increases with increasing germanium content, whereas ΔC_p monotonically decreases. Isothermal physical aging is performed at a fixed absolute distance below T_g , and the evolution of enthalpy for all samples confirms that the expected physical aging response occurs. The time required to reach equilibrium increases with decreasing temperature. At a given distance from T_g , the time required to reach equilibrium decreases as germanium content increases and fragility decreases. No evidence for a Boolchand intermediate phase characterized by high stability and absence of physical aging is found. The results presented in this study indicate that the lack of aging observed by other researchers is due to performing aging at room temperature for samples with widely differing T_g s.

References

1. Phillips JC. "Topology of Covalent Non-crystalline Solids I: Short-range Order in Chalcogenide Alloys" *Journal of Non-Crystalline Solids* 1979;34:153-181.
2. Thorpe MF. "Continuous deformations in random networks" *Journal of Non-Crystalline Solids* 1983;57:355-370.
3. Lucovsky G, Phillips JC. "Intermediate phases in binary and ternary alloys: a new perspective on semi-empirical bond constraint theory" *Journal of Physics: Condensed Matter* 2007;19:455218(1-20).
4. Zakery A. "Pulsed Laser Deposition of Chalcogenide Films for Nonlinear Photonic Applications" *Journal of Optoelectronics and Advanced Materials* 2005;7:1143-1155.
5. Golovchak R, Shpotyuk O, Kozdras A, Bureau B, Vlček M, Ganjoo A, Jain H. "Atomistic Model of Physical Ageing in Se-rich As–Se Glasses" *Philosophical Magazine* 2007;87:4323-4334.
6. Shpotyuk O, Hyla M, Boyko V, Golovchak R. "Reversibility windows in selenide-based chalcogenide glasses" *Physica B: Condensed Matter* 2008;403:3830-3837.
7. Thorpe MF, Jacobs DJ, Chubynsky MV, Phillips JC. "Self-organization in Network Glasses" *Journal of Non-Crystalline Solids* 2000;266-269:859-866.
8. Wang Y, Boolchand P, Micoulaut M. "Glass Structure, Rigidity Transitions and the Intermediate Phase in the Ge–As–Se Ternary" *Europhysics Letters* 2000;52:633-639.

9. Chen P, Boolchand P, Georgiev DG. "Long term aging of selenide glasses: evidence of sub- T_g endotherms and pre- T_g exotherms" *Journal of Physics: Condensed Matter* 2010;22:065104(1-16).
10. Kozdras A, Golovchak R, Shpotyuk O, Szymura S, Saiter A, Saiter JM. "Light-assisted physical aging in chalcogenide glasses: Dependence on the wavelength of incident photons" *Journal of Materials Research* 2011;26:2420-2427.
11. Golovchak R, Shpotyuk O, Kozdras A. "On the reversibility window in binary As-Se glasses" *Physics Letters A* 2007;370:504-508.
12. Golovchak R, Gorecki Cz, Kozdras A, Shpotyuk O. "Physical ageing effects in vitreous arsenic selenides" *Solid State Communications* 2006;137:67-69.
13. Golovchak R, Kozdras A, Shpotyuk O, Kozyukhin S, Saiter JM. "Long-term ageing behaviour in Ge-Se glasses" *Journal of Materials Science* 2009;44:3962-3967.
14. Chakravarty S, Georgiev DG, Boolchand P, Micoulaut M. "Ageing, fragility and the reversibility window in bulk alloy glasses" *Journal of Physics: Condensed Matter* 2005;17:L1-L7.
15. Qu T, Boolchand P. "Shift in elastic phase boundaries due to nanoscale phase separation in network glasses: the case of $Ge_xAs_xS_{1-2x}$ " *Philosophical Magazine* 2005;85:875-884.
16. Golovchak R, Jain H, Shpotyuk O, Kozdras A, Saiter A, Saiter JM. "Experimental verification of the reversibility window concept in binary As-Se

- glasses subjected to a long-term physical aging" *Physical Review B* 2008;78:014202 (1-6).
17. Georgiev DG, Boolchand P, Micoulaut M. "Rigidity transitions and molecular structure of As_xSe_{1-x} glasses" *Physical Review B* 2000;62:R9228-R9231.
 18. Boolchand P, Georgiev DG, Micoulaut M. "Nature of glass transition in chalcogenides" *Journal of Optoelectronics and Advanced Materials* 2002;4:823-836.
 19. Pattanayak P, Asokan S. "A sharp thermally reversing window in $As_{45}Te_{55-x}I_x$ chalcogenide glasses revealed by alternating differential scanning calorimetry and photo thermal deflection studies" *Journal of Non-Crystalline Solids* 2008;354:3824-3827.
 20. Anbarasu M, Singh KK, Asokan S. "Evidence for a thermally reversing window in bulk Ge–Te–Si glasses revealed by alternating differential scanning calorimetry" *Philosophical Magazine* 2008;88:599-605.
 21. Madhu BJ, Jayanna HS, Asokan S. "Evidence of an intermediate phase in ternary $Ge_7Se_{93-x}Sb_x$ glasses" *European Physical Journal B* 2009;71:21-25.
 22. Feng XW, Bresser WJ, Boolchand P. "Direct evidence for stiffness threshold in Chalcogenide glasses" *Physical Review Letters* 1997;78:4422-4425.
 23. Selvanathan D, Bresser WJ, Boolchand P. "Stiffness transitions in Si_xSe_{1-x} glasses from Raman scattering and temperature-modulated differential scanning calorimetry" *Physical Review B* 2000;61:15061-15076.

24. Micoulaut M. "Simple clues and rules for self-organized rigidity in glasses"
Journal of Optoelectronics and Advanced Materials 2007;9:3235-3240.
25. Inam F, Shatnawi MT, Tafen D, Billinge SJL, Chen P, Drabold DA. "An intermediate phase in $\text{Ge}_x\text{Se}_{1-x}$ glasses: experiment and simulation" Journal of Physics: Condensed Matter 2007;19:455206(1-10).
26. Petkov K, Popescu M, Lörinczi A, Sava F, Zamfira S, Leonovici M.
"Structural transition and intermediate (Borland) phase in amorphous thin films of the As_2S_3 - GeS_2 system" Journal of Optoelectronics and Advanced Materials 2007;9:3088-3092.
27. Elabbar AA, Abu-Sehly AA. "Structural relaxation and rigidity transition in aged and rejuvenated $\text{As}_x\text{Se}_{100-x}$ glasses" Physica B: Condensed Matter 2011;406:4261-4265.
28. Golovchak R, Kozdras A, Shpotyuk O, Gorecki Cz, Kovalskiy A, Jain H.
"Temperature-dependent structural relaxation in $\text{As}_{40}\text{Se}_{60}$ glass" Physics Letters A 2011;375:3032–3036.
29. Yang G, Bureau B, Rouxel T, Gueguen Y, Gulbitten O, Roiland C, Soignard E, Yarger JL, Troles J, Sangleboeuf JC, Lucas P. "Correlation between structure and physical properties of chalcogenide glasses in the $\text{As}_x\text{Se}_{1-x}$ system" Physical Review B 2010;82:195206 (1-8).
30. Lucas P, King EA, Gulbitten O, Yarger JL, Soignard E, Bureau B. "Bimodal phase percolation model for the structure of Ge-Se glasses and the existence of the intermediate phase" Physical Review B 2009;80:214114 (1-8).

31. Simon SL, McKenna GB. "Quantitative analysis of errors in TMDSC in the glass transition region" *Thermochimica Acta* 2000;348:77-89.
32. Simon SL, McKenna GB. "The effects of structural recovery and thermal lag in temperature-modulated DSC measurements" *Thermochimica Acta* 1997;307:1-10.
33. Hutchinson JM, Tong AB, Jiang Z. "Aging of polycarbonate studied by temperature modulated differential scanning calorimetry" *Thermochimica Acta* 1999;335:27-42.
34. Echeverria I, Kolek PL, Plazek DJ, Simon SL. "Enthalpy recovery, creep and creep-recovery measurements during physical aging of amorphous selenium" *Journal of Non-Crystalline Solids* 2003;324:242-255.
35. Svoboda R, Pustkova P, Malek J. "Relaxation behavior of glassy selenium" *Journal of Physics and Chemistry of Solids* 2007;68:850-854.
36. Malek J, Svoboda R, Pustkova P, Cicmanec P. "Volume and enthalpy relaxation of a-Se in the glass transition region" *Journal of Non-Crystalline Solids* 2009;355:264-272.
37. Williams ML, Landel RF, Ferry JD. "The temperature dependence of relaxation mechanisms in amorphous polymers and other glass-forming liquids" *Journal of the American Chemical Society* 1955;77:3701-3707.
38. Moynihan CT, Lee SK, Tatsumisago M, Minami T. "Estimation of activation energies for structural relaxation and viscous flow from DTA and DSC experiments" *Thermochimica Acta* 1996;280:153-162.

39. Plazek DJ, Frund ZN. "Epoxy resins (DGEBA): the curing and physical aging process" *Journal of Polymer Science Part B Polymer Physics* 1990;28:431-448.
40. Badrinarayanan P, Zheng W, Li QX, Simon SL. "The glass transition temperature versus the fictive temperature" *Journal of Non-Crystalline Solids* 2007;353:2603-2612.
41. Petrie SEB. "Thermal behavior of annealed organic glasses" *Journal of Polymer Science Part A-2: Polymer Physics* 1972;10:1255-1272.
42. Gaur U, Shu HC, Mehta A, Wunderlich B. "Heat capacity and other thermodynamic properties of linear macromolecules. I. Selenium" *Journal of Physical and Chemical Reference Data* 1981;10:89-118.
43. Shu HC, Gaur U, Wunderlich B. "Heat capacity and chemical equilibria of liquid selenium" *Journal of Polymer Science Polymer Physics Edition* 1980;18:449-456.
44. Faivre G, Gardissat JL. "Viscoelastic properties and molecular structure of amorphous selenium" *Macromolecules* 1986;19:1988-1996.
45. Stephens RB. "The viscosity and structural relaxation rate of evaporated amorphous selenium" *Journal of Applied Physics* 1978;49:5855-5864.
46. Bernatz KM, Echeverria I, Simon SL, Plazak DJ. "Characterization of the molecular structure of amorphous selenium using recoverable creep compliance measurements" *Journal of Non-Crystalline Solids* 2002;307-310:790-801.

47. Moynihan CT, Easteal AJ, Wilder J, Tucker J. "Dependence of the glass transition temperature on heating and cooling rate" *Journal of Physical Chemistry* 1974;78:2673-2677.
48. Moynihan CT, Schnaus UE. "Heat Capacity and Equilibrium Polymerization of Vitreous Se" *Journal of the American Ceramic Society* 1971;54:136-140.
49. Tammann G, Gronow HEV. "Die spezifische Wärme, die Temperaturleitfähigkeit und die adiabatischen Temperaturänderungen im Erweichungsintervall der Gläser" *Zeitschrift für anorganische und allgemeine Chemie* 1930;192:193-209.
50. Moynihan CT, Schnaus UE. "Heat capacity above 320 K and heat of fusion of hexagonal selenium" *Materials Science and Engineering* 1970;6:227-278.
51. Angell CA, Ngai KL, McKenna GB, McMillan PF, Martin SW. "Relaxation in glassforming liquids and amorphous solids" *Journal of Applied Physics* 2000;88:3113-3157.
52. DiMarzio EA. "On the second-order transition of a rubber" *Journal of Research of the National Bureau of Standards* 1964;68A:611-617.
53. Sreeram AN, Swiler DR, Varshneya AK. "Gibbs-DiMarzio equation to describe the glass transition temperature trends in multicomponent chalcogenide glasses" *Journal of Non-Crystalline Solids* 1991;127:287-297.
54. Feng XW, Bresser WJ, Boolchand P. "Rigidity transitions in binary Ge–Se glasses and the intermediate phase" *Journal of Non-Crystalline Solids* 2001;293-295:348-356.

55. Angell CA. "Relaxation in liquids, polymers and plastic crystals—strong/fragile patterns and problems" *Journal of Non-Crystalline Solids* 1991;131-133:13-31.
56. Li QX, Simon SL. "Enthalpy recovery of polymeric glasses: Is the theoretical limiting liquid line reached?" *Polymer* 2006;47:4781-4788.
57. Cowie JMG, Ferguson R. "Physical ageing of poly (methyl methacrylate) from enthalpy relaxation measurements" *Polymer* 1993;34:2135–2141.
58. Cowie JMG, Harris S, McEwen IJ. "Physical ageing in poly(vinyl acetate) 1. Enthalpy relaxation" *Journal of Polymer Science Part B: Polymer Physics* 1997;35:1107–1116.
59. Cameron NR, Cowie JMG, Ferguson R, McEwan I. "Enthalpy relaxation of styrene–maleic anhydride (SMA) copolymers Part 1. Single component systems" *Polymer* 2000;41:7255–7262.
60. Boucher VM, Cangialosi D, Alegria A, Colmenero J. "Enthalpy recovery of glassy polymers: Dramatic deviations from the extrapolated liquidlike behavior" *Macromolecules* 2011;44:8333-8342.
61. Hutchinson JM, Kumar P. "Enthalpy relaxation in polyvinyl acetate" *Thermochimica Acta* 2002;391:197-217.
62. Kohlrausch R. "Theorie des elektrischen Rückstandes in der Leidener Flasche" *Annalen der Physik* 1854;167:179-214.

63. Willams G, Watts DC. "Non-symmetrical dielectric relaxation behaviour arising from a simple empirical decay function" *Transactions of the Faraday Society* 1970;66:80-85.
64. Simon SL, Sobieski JW, Plazek DJ. "Volume and enthalpy recovery of polystyrene" *Polymer* 2001;42:2555-2567.
65. Tool AQ. "Relation Between Inelastic Deformability and Thermal Expansion of Glass in its Annealing Range" *Journal of the American Ceramic Society* 1946;29:240-253.
66. Narayanaswamy OS. "A model of structural relaxation in glass" *Journal of the American Ceramic Society* 1971;54:491-498.
67. Moynihan CT et al. "Structural relaxation in vitreous materials" *Annals of the New York Academy of Sciences* 1976;279:15-35.
68. Greiner R, Schwarzl FR. "Thermal contraction and volume relaxation of amorphous polymers" *Rheologica Acta* 1984;23:378-395.
69. Koh YP, Simon SL. "Structural relaxation of stacked ultrathin polystyrene films" *Journal of Polymer Science Part B: Polymer Physics* 2008;46:2741–2753.
70. Struik LCE, *Physical Aging in Amorphous Polymers and Other Materials*. New York: Elsevier; 1978.
71. Cortes P, Montserrat S, Ledru J, Saiter JM. "Enthalpy relaxation in $\text{Ge}_x\text{Se}_{1-x}$ chalcogenide glasses" *Journal of Non-Crystalline Solids* 1998;235-237:522-526.

72. Selvanathan D, Bresser WJ, Boolchand P, Goodman B. "Thermally reversing window and stiffness transitions in chalcogenide glasses" *Solid State Communications* 1999;111:619-624.
73. Pattanayak P, Asokan S. "Electrical switching and thermal studies on $\text{Ge}_{22}\text{Te}_{78-x}\text{I}_x$ chalcogenide glasses: The effect of iodine on network-topology" *Solid State Communications* 2007;142:698–701.
74. Mitkova M, Wang Y, Boolchand P. "Dual chemical role of Ag as an additive in chalcogenide glasses" *Physical Review Letters* 1999;83:3848-3851.

Table 6.1. Parameters characterizing relaxation in the glass transition region for various Ge-Se glasses

Sample	r_c	T_f' after cooling at 10 K/min (K)	$dT_f'/d(\log q)$	m	$\Delta h/R$ (kK)
Se*	2.00	308.2 ± 0.6 (35.0 °C)	3.3 ± 0.5	93.4 ± 14.3	66.3 ± 10.3
Ge ₅ Se ₉₅	2.10	334.6 ± 0.4 (61.4 °C)	3.6 ± 0.2	93.0 ± 5.3	71.6 ± 4.1
Ge ₁₀ Se ₉₀	2.20	366.9 ± 0.2 (93.7 °C)	7.1 ± 0.3	51.7 ± 2.2	43.7 ± 1.9
Ge ₁₇ Se ₈₃	2.35	406.0 ± 3.5 (132.8 °C)	7.9 ± 0.3	51.4 ± 2.4	48.0 ± 2.7
Ge ₂₀ Se ₈₀	2.40	448.9 ± 0.8 (175.7 °C)	10.2 ± 0.8	44.0 ± 3.5	45.5 ± 3.7
Ge ₂₃ Se ₇₇	2.45	470.2 ± 1.1 (197.0 °C)	10.7 ± 1.1	43.9 ± 4.6	47.6 ± 5.1
Ge ₃₀ Se ₇₀	2.60	577.6 ± 3.1 (304.4 °C)	11.3 ± 0.5	51.1 ± 2.5	68.0 ± 3.7

* Pure selenium data are obtained from ref [34]

Table 6.2. Aging temperatures used for different glass compositions

Sample	Aging Temperatures, T_a (°C)
Se*	30.0, 25.0, 20.0
Ge ₅ Se ₉₅	55.4, 50.3, 45.3
Ge ₁₀ Se ₉₀	88.9, 83.9, 78.8
Ge ₁₇ Se ₈₃	128.2, 123.1, 118.0
Ge ₂₀ Se ₈₀	170.5, 165.5, 160.3
Ge ₂₃ Se ₇₇	192.7, 187.8, 182.5

* Pure selenium data are obtained from ref [34]

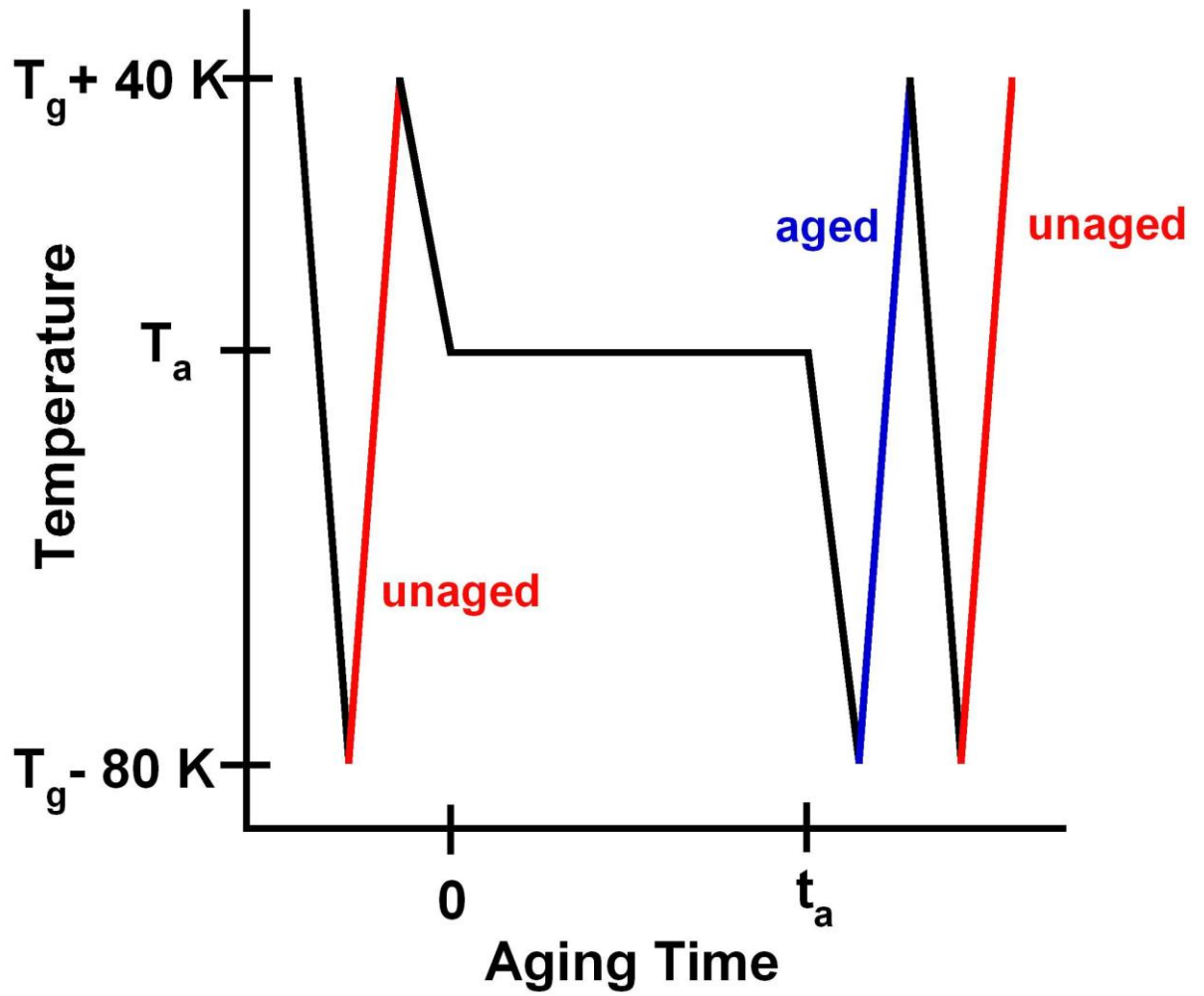


Figure 6.1. Schematic for DSC experiment of aging response

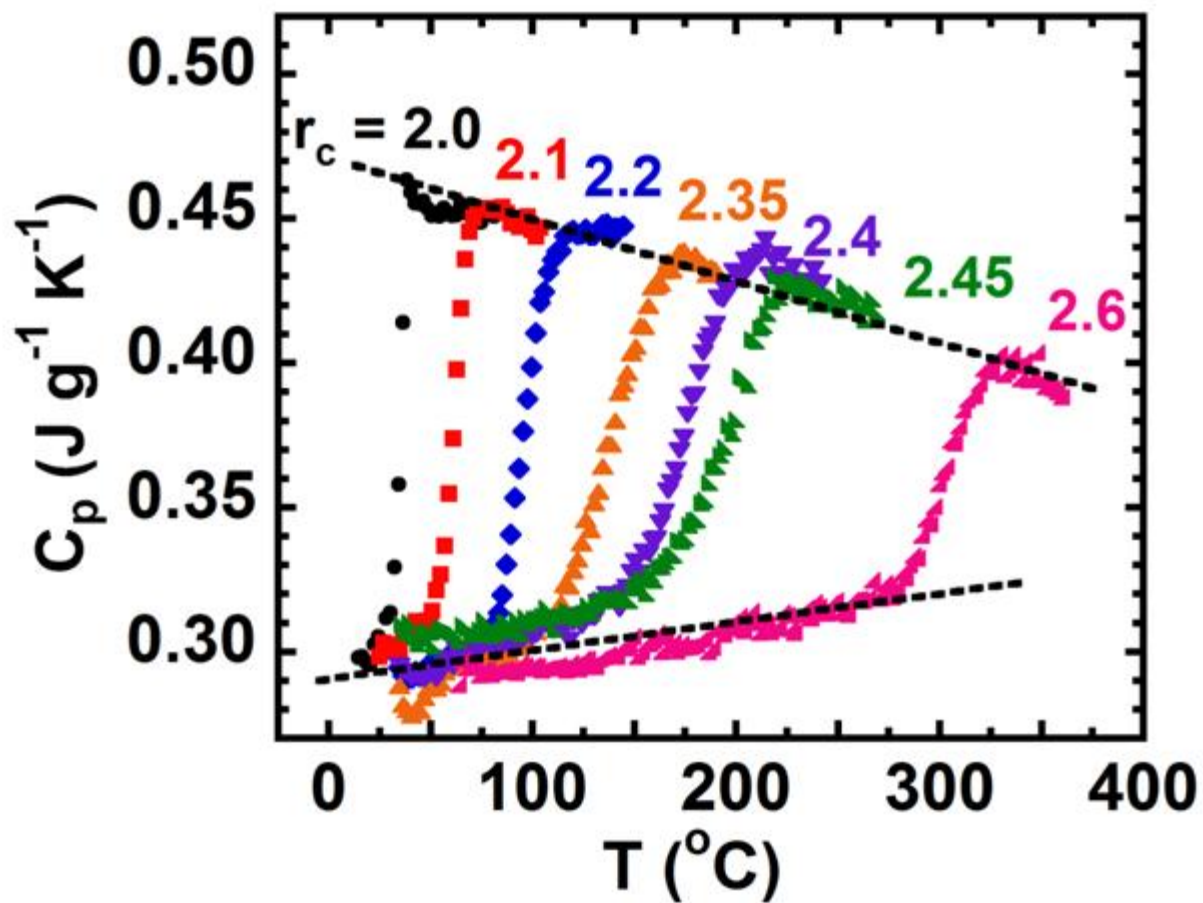


Figure 6.2. Absolute heat capacity versus temperature for average coordination number ranging from 2.0 (Se) to 2.6 ($\text{Ge}_{30}\text{Se}_{70}$). The dashed line is a guide to the eye.

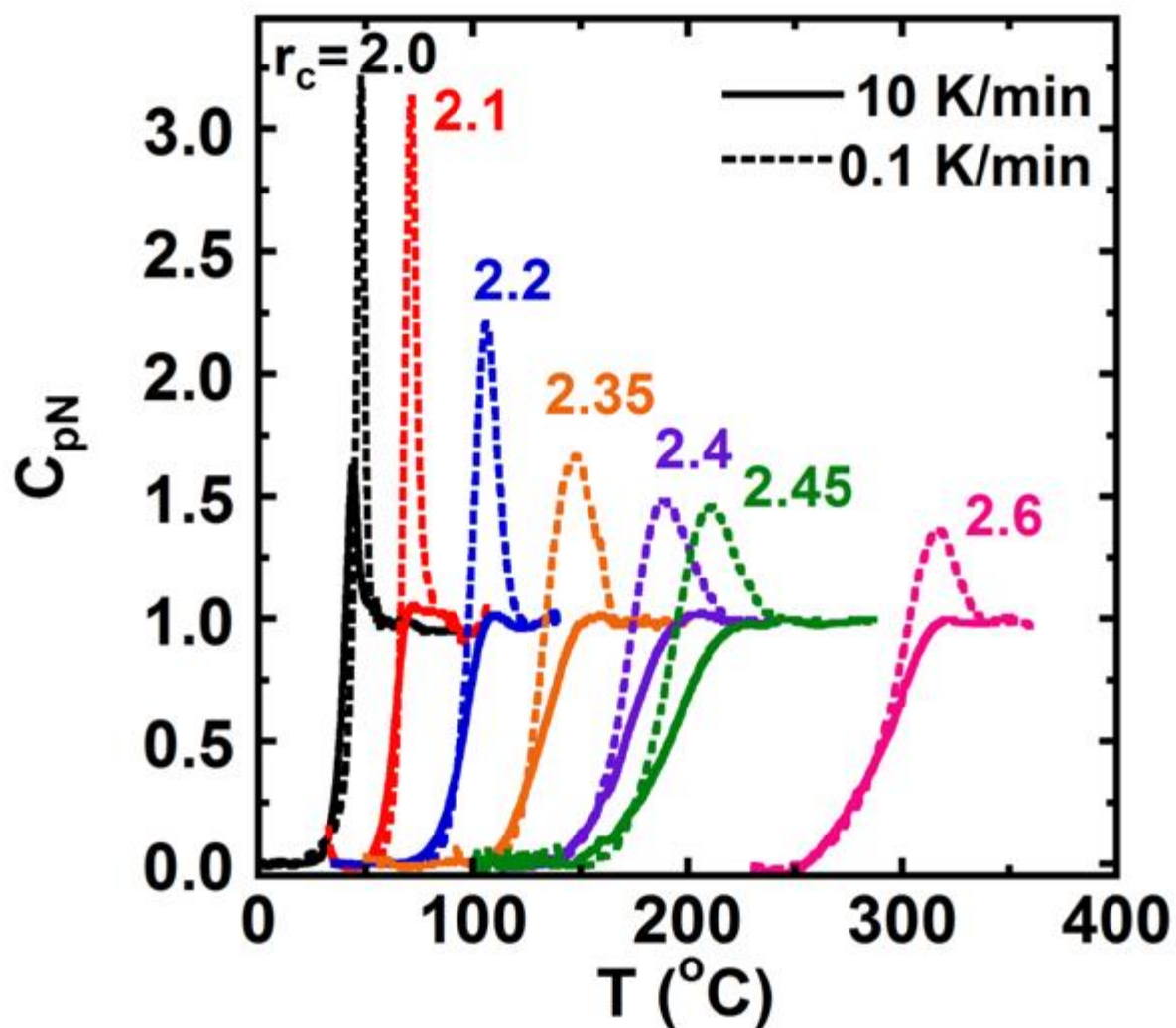


Figure 6.3. Normalized heat capacity versus temperature for different composition Ge-Se alloys for heating rates of 10 K/min (solid line) and 0.1 K/min (dashed line).

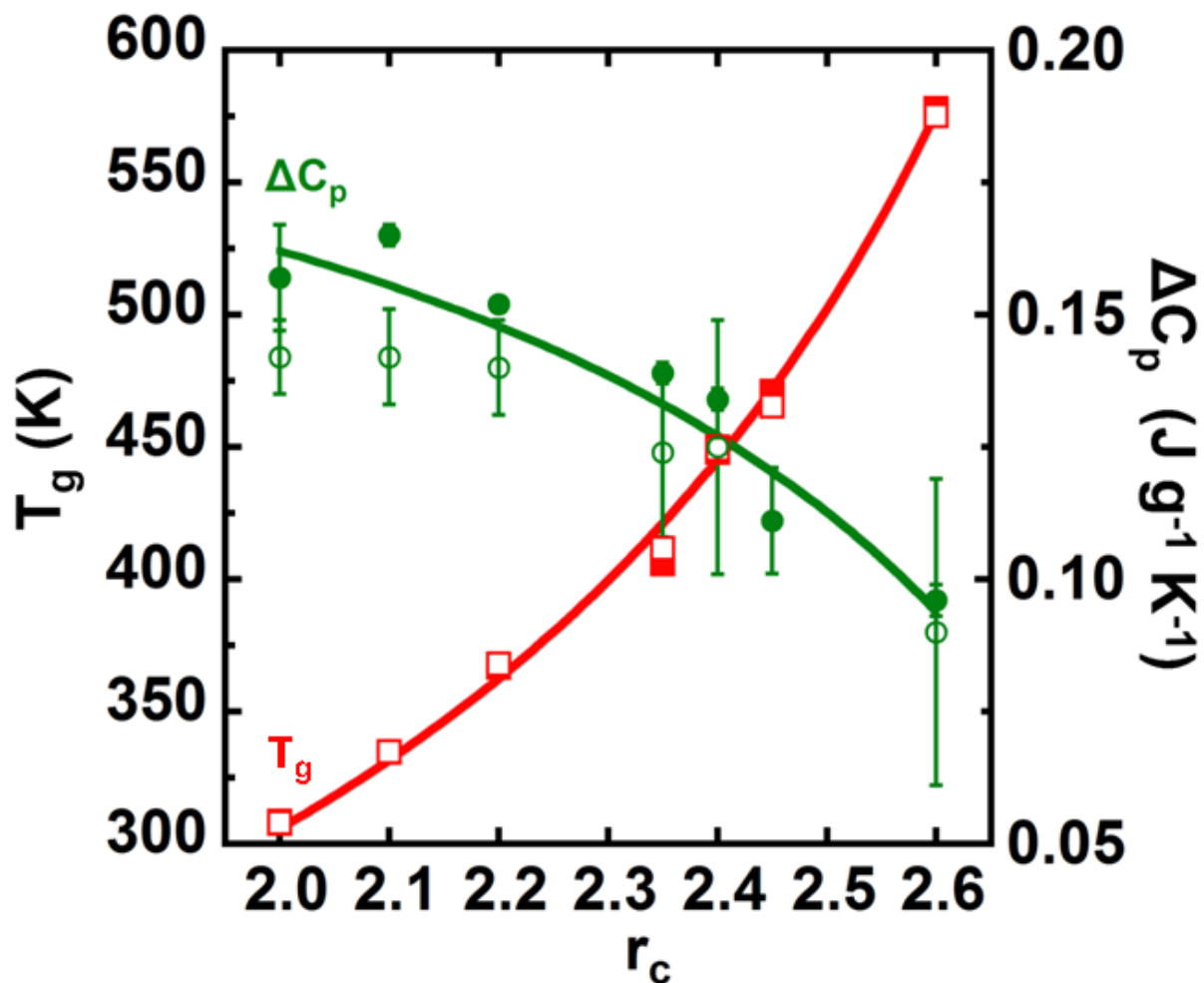


Figure 6.4. T_g and ΔC_p as a function of average coordination number. Squares and circles refer to T_g and ΔC_p , respectively. The solid symbols indicate data obtained from conventional DSC after cooling at 10 K/min. The open symbols are from the step scan technique. The red line is the fit to equation (6.6) and the green line is the fit to equation (6.7).

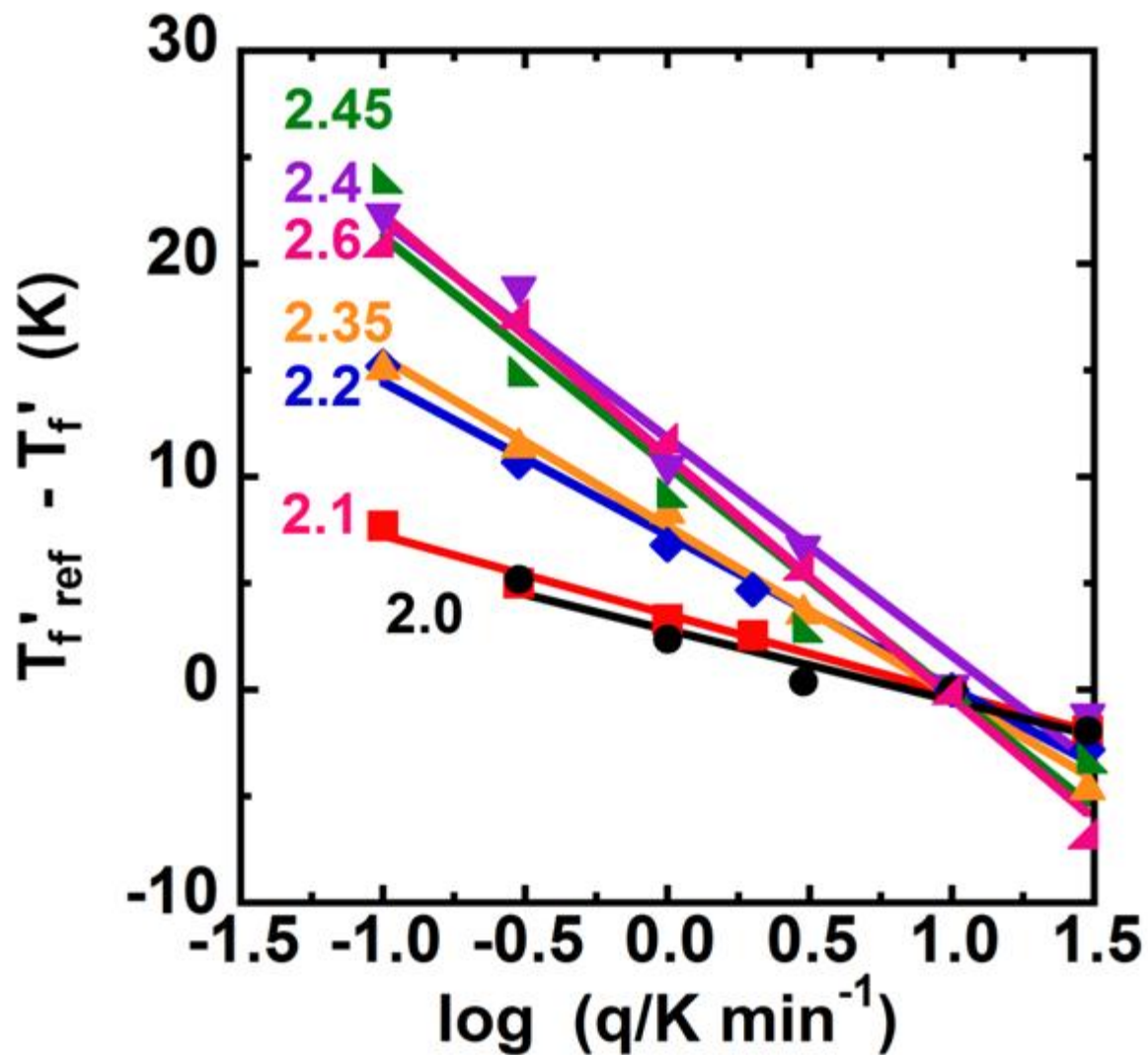


Figure 6.5. The dependence of fictive temperature on cooling rate for $\text{Ge}_x\text{Se}_{100-x}$ samples with the fictive temperature obtained on cooling at 10 K/min serving as reference. The $r_c = 2.0$ data are taken from reference [34].

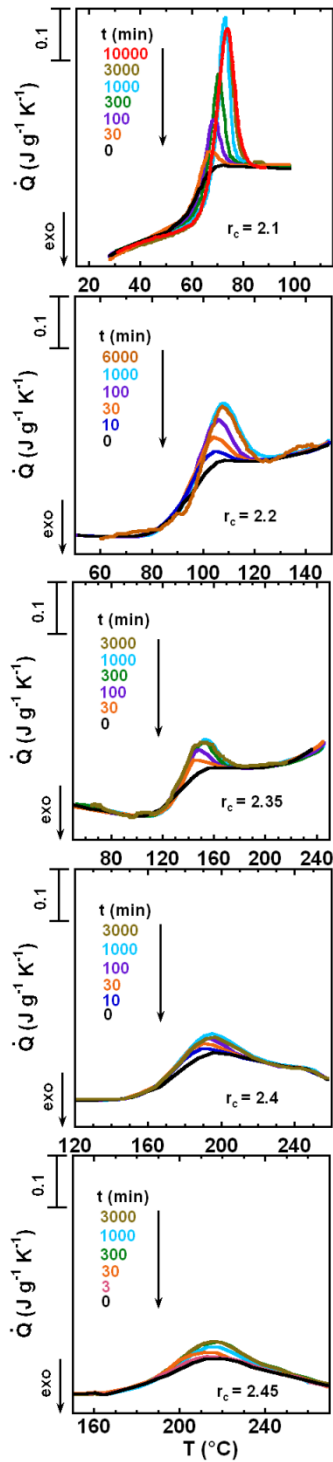


Figure 6.6. Representative DSC heat flow curves as a function of the aging time t for an aging temperature $T_a \approx T_g - 15 \text{ K}$ for various composition glasses.

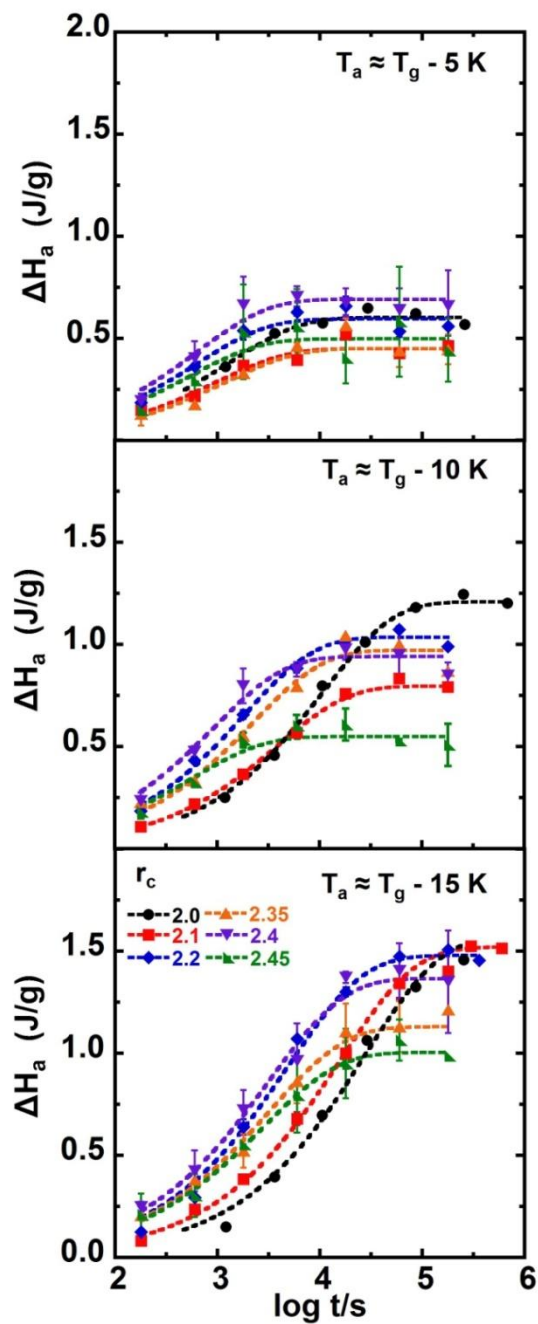


Figure 6.7. The enthalpy loss on aging (ΔH_a) as a function of the logarithm of the isothermal aging time for the aging temperatures nominally 5 K, 10 K, and 15 K below T_g . The dashed lines are fits using the KWW function. Data for pure selenium, $r_c = 2.0$, are taken from reference [34].

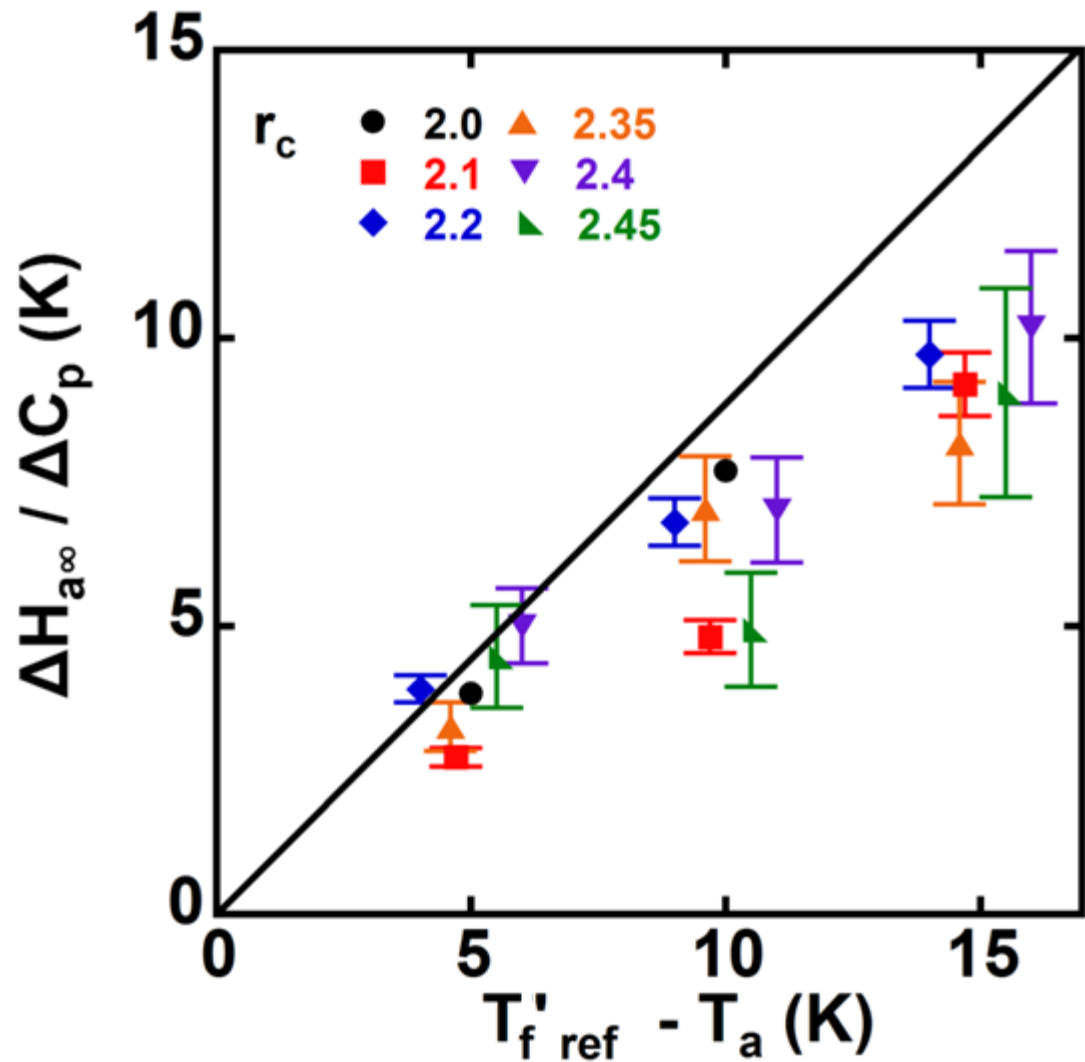


Figure 6.8. $\Delta H_{a\infty} / \Delta C_p$ as a function of the difference between the reference fictive temperature and the aging temperature for various compositions. The line represents the expectation from equation (6.10). Data for pure selenium, $r_c = 2.0$, are taken from reference [34].

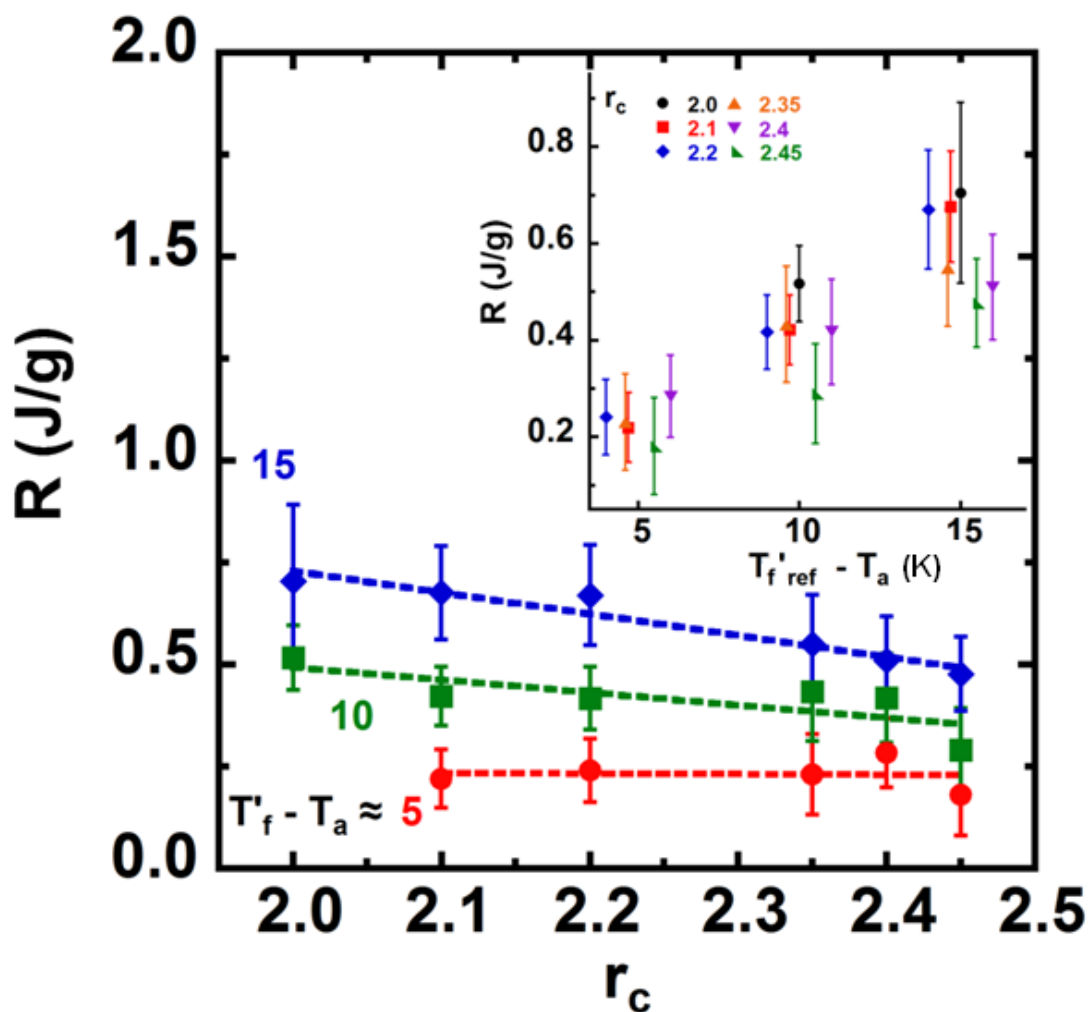


Figure 6.9. The dependence of the aging rate on the average coordination number. The inset shows aging rate versus aging temperature plotted as distance from the reference fictive temperature. The $r_c = 2.0$ data are taken from reference [34].

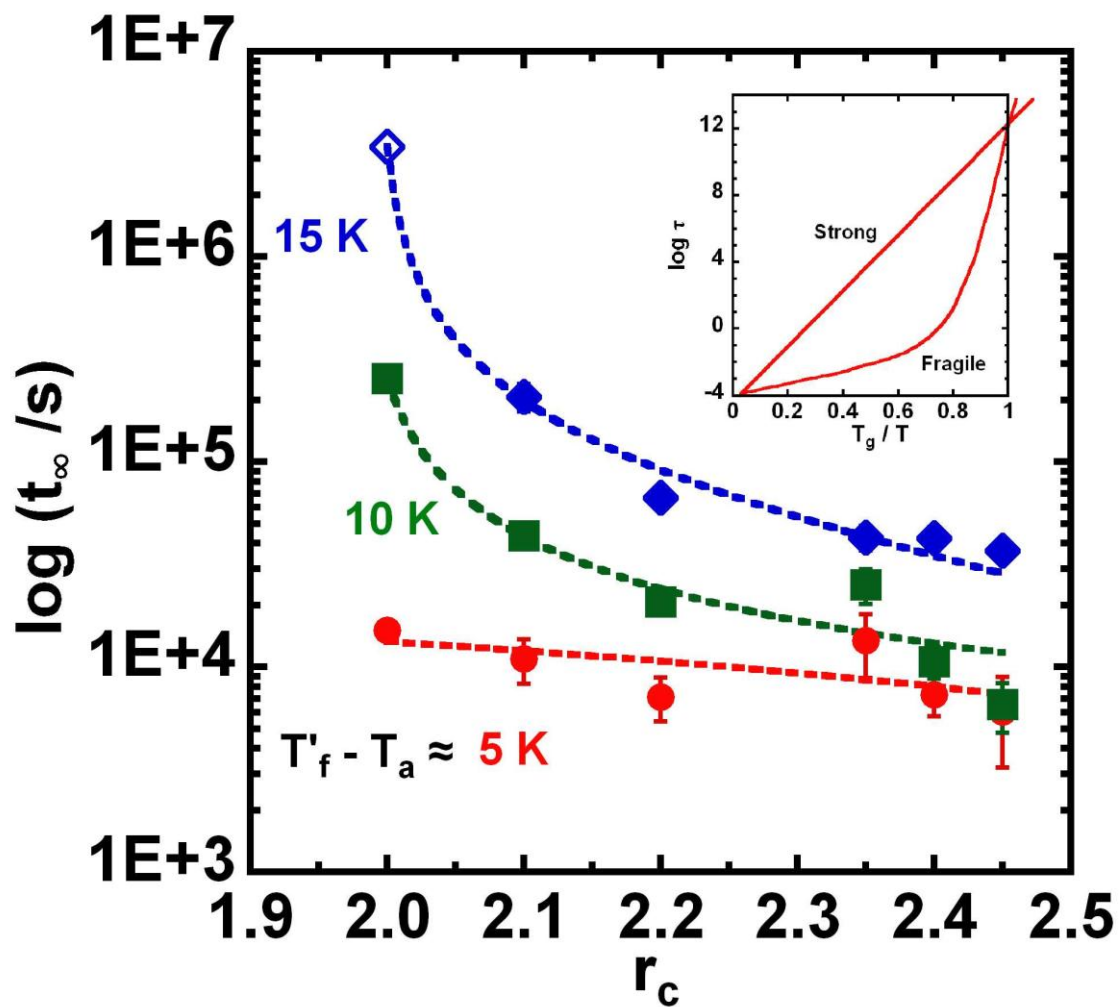


Figure 6.10. The time required to reach equilibrium (t_∞) as a function of average coordination number for different aging temperatures. The dashed line is a guide to the eye. The $r_c = 2.0$ data is taken from reference [34] and the open symbols represent extrapolated values. The inset is a schematic Angell plot [55] showing the logarithm of the relaxation time versus T_g/T for strong and fragile glass formers.

CHAPTER 7

CONCLUSION

The effect of nanoconfinement on the free radical polymerization of methyl methacrylate (MMA) has been investigated. Motivated by our previous modeling work [1] that the reactivity is enhanced under nanoconfined environment, we performed a series of isothermal polymerizations of MMA in controlled pore glass (CPG) following the similar thermal analysis procedure in literature [2] for the reaction temperatures ranging from 60 to 95 °C. When the polymerization temperature is extended to high above the glass transition temperature for pure polymer ($T_{g,p}$), the nanoconfinement effects upon the thermodynamics of PMMA were also examined. The increased reactivity of PMMA in nanopores is able to be quantitatively described by the modification [3,4] of the model of Verros et al. [5] and the properties of the corresponding polymers are found to be improved. Three publications [6-8] have resulted and the major findings are shown:

- The reactivity of MMA to form PMMA is obviously enhanced under nanoconfined environment which is consistent with the previous modeling prediction [1]. The initial rate is considerably faster in hydrophilic pores compared to that in bulk and hydrophobic pores, and the rate increases approximately linearly with reciprocal pore size. The onset of autoacceleration decreases with decreasing pore size in nanopores, and the effect is more dramatic in hydrophilic pores. The increased

autoacceleration effect is attributed to the reduced chain diffusivity resulting in a decrease in the rate of termination of free radicals.

- Both number and weight-average molecular weight increase and PDI decrease in nanopores due to the shorter time to reach autoacceleration and the previous model used to describe the reaction kinetics can reasonably predict these trends without adjustable parameters [3,4]; on the other hand, the isotactic triads are found to dramatically increase in hydrophilic pores. All of these experimental observations are qualitatively consistent with literature findings [9-17]. The enhancement in isotacticity and T_g in hydrophilic pores are associated with the specific interaction between carbonyl and surface silanol groups.
- The extent of MMA polymerization as a function of temperature for both bulk and nanoconfined samples is investigated using DSC. It found that the equilibrium conversion decreases with the polymerization temperature increases. The ceiling temperature shifts to lower temperatures presumably due to the larger negative value of entropy for propagation in nanopores, but this effect is independent of the pore surface chemistry. The changes in confined entropy appear to be related to the chain length, as suggested in the literature [18-21].

The kinetics associated with glass transition temperature of binary chalcogenide glasses (Ge-Se) was investigated using DSC for Ge content ranging from 0 to 30 atom%. Based on the observation of structural recovery, no evidence is found

for an intermediate phase characterized by high stability and absence of physical aging.

One paper [22] was published and the major findings are listed below:

- As Ge content increases, the structure of glasses becomes more rigid and T_g is found to increase, whereas ΔC_p monotonically decreases. The aging experiments are performed at a fixed absolute distance below T_g and the occurrence of the expected physical aging is observed.
- For high Ge content glasses, both the fragility and the time required to reach equilibrium decrease at a given distance from T_g . The interpretation of the existence of an intermediate phase is attributed to the aging experiments at room temperature with widely differing T_g s.

References

1. Begum F, Simon SL. "Modeling methyl methacrylate free radical polymerization in nanoporous confinement" *Polymer* 2011;52:1539-1545.
2. Achilias DS, Verros GD. "Modeling of diffusion-controlled reactions in free radical solution and bulk polymerization: Model validation by DSC experiments" *Journal of Applied Polymer Science* 2010;116:1842-1856.
3. Begum F, Zhao HY, Simon SL. "Modeling methyl methacrylate free radical polymerization: Reaction in hydrophilic nanopores" *Polymer* 2012;53:3238-3244.
4. Begum F, Zhao HY, Simon SL. "Modeling methyl methacrylate free radical polymerization: Reaction in hydrophobic nanopores" *Polymer* 2012;53:3261-3268.
5. Verros GD, Latsos T, Achilias DS. "Development of a unified framework for calculating molecular weight distribution in diffusion controlled free radical bulk homo-polymerization" *Polymer* 2005;46:539-552.
6. Zhao HY, Simon SL. "Methyl methacrylate polymerization in nanoporous confinement" *Polymer* 2011;52:4093-4098.
7. Zhao HY, Yu ZN, Begum F, Hedden RC, Simon SL. "The effect of nanoconfinement on methyl methacrylate polymerization: T_g , molecular weight, and tacticity" *Polymer* 2014;55:4959-4965.
8. Zhao HY, Simon SL. "Equilibrium free- radical polymerization of methyl methacrylate under nanoconfinement" In preparation.

9. Li XC, King TA, Pallikari-Viras F. "Characteristics of Composites Based of PMMA Modified Gel Silica Glasses" *Journal of Non-Crystalline Solids* 1994;170:243-249.
10. Ng SM, Ogino S, Aida T, Koyano KA, Tatsumi T. "Free Radical Polymerization within Mesoporous Zeolite Channels" *Macromolecular Rapid Communications* 1997;18:991-996.
11. Kageyama K, Ng SM, Ichikawa H, Aida T. "Macromolecular Synthesis using Mesoporous Zeolites" *Macromolecular Symposia* 2000;157:137-142.
12. Ni XF, Shen ZQ, Yasuda H. "Polymerization of methyl methacrylate with samarocene complex supported on mesoporous silica" *Chinese Chemical Letters* 2001;12:821-822.
13. Kalogeras IM, Vassilikou-Dova A. "Dielectric probe of intermolecular interactions in poly (methyl methacrylate)(PMMA) and PMMA+ SiO₂ matrixes doped with luminescent organics" *Journal of Physical Chemistry B* 2001;105:7651-7662.
14. Kalogeras IM, Neagu ER. "Interplay of surface and confinement effects on the molecular relaxation dynamics of nanoconfined poly(methyl methacrylate) chains" *European Physical Journal E* 2004;14:193-204.
15. Uemura T, Ono Y, Kitagawa K, Kitagawa S. "Radical polymerization of vinyl monomers in porous coordination polymers: Nanochannel size effects on reactivity, molecular weight, and stereostructure" *Macromolecules* 2008;41:87-94.

16. Ikeda K, Kida M, Endo K. "Polymerization of methyl methacrylate with radical initiator immobilized on the inside wall of Mesoporous Silica" *Polymer Journal* 2009;41:672-678.
17. Uemura T, Ono Y, Hijikata Y, Kitagawa S. "Functionalization of coordination nanochannels for controlling tacticity in radical vinyl polymerization" *Journal of the American Chemical Society* 2010;132:4917-4924.
18. De Gennes PG. *Scaling Concepts in Polymer Physics*. Ithaca, NY: Cornell University Press; 1979.
19. Kong CY, Muthukumar MJ. "Polymer translocation through a nanopore. II. Excluded volume effect" *Journal of Chemical Physics* 2004;120:3460-3466.
20. Sakaue T, Raphael E. "Polymer chains in confined spaces and flow-injection problems: some remarks" *Macromolecules* 2006;39:2621-2628.
21. Cacciuto A, Luijten E. "Self-avoiding flexible polymers under spherical confinement" *Nano Letters* 2006;6:901-905.
22. Zhao HY, Koh YP, Pyda M, Sen S, Simon SL. "The kinetics of the glass transition and physical aging in germanium selenide glasses" *Journal of Non-Crystalline Solids* 2013;368:63-70.

CHAPTER 8

FUTURE WORK

8.1 Generalization

The dramatic enhanced reactivity, molecular weight, tacticity, and T_g in hydrophilic pores are attributed to the specific interaction between carbonyl group of PMMA side chains and the silanol group at pore surface [1-4]. To generalize the findings concerning how the reactivity and properties change under a nanoconfined environment, experiments should be performed with other materials, such as polystyrene [5] containing a stable phenyl group or poly(vinyl acetate) with high reactivity [6]. The polymerization of styrene confined in nanopore can testify whether the reduced chain diffusivity is influenced by the pore surface polarity. Considering literature findings, T_g was found to decrease with decreasing film thickness for PS thin films [7] but T_g of PVAc thin films show no dependence on film thickness [8]. Thus, it would also be interesting to investigate the T_g of PS or PVAc synthesized in CPG pores to compare with thin film.

8.2 Synthesized tool to obtain prespecified properties

With increased demands for high-tech, low cost polymers, the ability to control properties of free radical polymerization is gaining attention [9,10]. Controlled radical polymerization is usually achieved by living radical polymerization in solution to avoid side and termination reactions that compromise control of molecular weight, distribution, and chain structure. [11,12] Considering the environmental hazard

caused by metal catalysis used in living polymerization, an alternative method that synthesizes polymer in confined and specifically designed organic channels with pore sizes less than 5 nm has been investigated by research groups. [13,14] In comparison, in our monomer/nanopore system, the smallest nanopore we employed is 13 nm-diameter which is similar to the radius of gyration for PMMA polymerized at 80 °C in bulk (17 nm) [15]. Thus, we might expect more pronounced effects if we reduced the CPG pore diameter to smaller sizes, such as reported in literature [16,17]. In addition, our CPG pores are simple cylindrical structure and we might expect more changes by modifying the nanopore to the specifically designed structure, such as the helically twist nanochannels [18], thus using nanoconfinement geometry to control the polymerization.

8.3 Very high temperature polymerization

Approximately half of commercial polymeric materials are made by free radical polymerization [19] and the optimal reaction temperature is often high to avoid the influence of autoacceleration and to reduce the viscosity of reacted medium. Hence, a challenge for experimental investigation at these temperatures is to control the vapor pressure to minimize the volatility of the monomer reactant. In our current system, the boiling point of MMA is 101 °C and its volatility results in weight loss, for example, in DSC experiments at high temperature. Therefore, future work should consider investigating high temperature reactions using an alternative methacrylate monomer which has higher boiling point. For acrylate monomer, increasing the size of the alkyl group increases the boiling point (MMA: 101 °C, EMA: 119 °C, BMA:

163 °C) but only slightly affects the ceiling temperature due to the similar ΔH_p and ΔS_p ($-\Delta H_{p,MMA}$ vs. $-\Delta H_{p,EMA} = 56$ vs. 57.8 kJ/mol, $-\Delta S_{p,MMA}$ vs. $-\Delta S_{p,EMA} = 117.2$ vs. 124.4 J/mol/K) from literature [20]. Since the glass transition temperature of poly(ethyl methacrylate) (PEMA) is around 66 °C and $T_{c,EMA}$ is around 191 °C based on the equation (2.17), future work should investigate the equilibrium polymerization of EMA for the temperature ranging from 90 to 190 °C.

As was discussed in Chapter 5, we were not able to use medium pressure hermetic pans with o-rings to react MMA at high temperatures since a large amount of heat can be released in small space so that the reaction becomes explosive. However, we may expect the o-ring pan can work for another monomer that the autoacceleration is not as drastic as MMA, such as styrene (St). For styrene monomer, the boiling point is 146 °C and the depolymerization become appreciable when the reaction temperature is higher than 200 °C ($T_{c,st} = 310$ °C). [19] Since the polystyrene is good solvent for styrene monomer, the heat generated by autoacceleration can be dissipated to avoid explosive conditions so that it may be possible to use the medium pressure DSC pan with o-ring to study St equilibrium polymerization at high temperature (> 240 °C) with minimal weight loss.

One objective is to test the scaling of a confined chain under nanoconfinement. In literature [21-24], ΔS_{conf} is proportional to $-N^p d^{-m}$, where N is related to the molecular weight and m is related to the confinement geometry. To examine this scaling, we need to measure the molecular weight as function of temperature for the equilibrium polymerization and we also need to adjust the pore diameter to investigate

the influence of pore geometry and size. Since we found that polymerization of MMA/AIBN system only takes couple minutes at high temperature ($> 140\text{ }^{\circ}\text{C}$) in Chapter 5, thus, we may choose an alternative initiator to increase the experimental time scale to be able to measure the molecular weight. As reported in literature [25], di-*tert*-butyl peroxide (DTBP) may be a good choice since $k_{d,\text{DTBP}}$ is $3 \times 10^{-8}\text{ s}^{-1}$ at $70\text{ }^{\circ}\text{C}$, which is three order of magnitude smaller than $k_{d,\text{AIBN}}$ ($3 \times 10^{-5}\text{ s}^{-1}$) at the same temperature. One obstacle to obtain molecular weight for the samples in equilibrium polymerization is the influence of free radicals. If there is residual free radical in the system, the equilibrium balance can be broken even after the sample taken out of DSC furnace due to the fast propagation rate. Therefore, low concentrations of initiator (0.01 wt %) would be required. Once the equilibrium state is stable, we can transfer the DSC pans containing monomer/polymer mixture to liquid nitrogen environment for given time and then dissolve the mixture in tetrahydrofuran (THF) solvent with the free radical quencher 4-methoxyphenol for the GPC measurement.

The properties of PMMA synthesized in nanopores at high temperatures also attract our attention, and in particular, competing effects are of interest. For example, synthesis in nanopores tends to produce high molecular weight polymers but high reaction temperature tends to produce low molecular weight polymers due to monomer/polymer equilibrium. At low temperature polymerization, we found that surface chemistry exerts important influence on M_n , T_g , and isotacticity; however, the effect of those specific interactions is not clear at high temperatures. Thus, future work may involve studying the properties of polymer synthesized in nanopores with

different pore surface at high temperatures to determine conditions to achieve desired properties.

8.4 In situ polymerized nanocomposites

Although synthesis under nanoconfinement can obviously improve the properties of PMMA, use of the modified PMMA is achieved only after extracting the PMMA out of the nanopores using an organic solvent. However, such organic solvents, as methanol or THF, can cause the health and environmental hazards. Therefore, considering from another perspective, the polymers synthesized under nanoconfinement that can be directly used in practical applications without extraction may be of more practical use. For example, the polymer synthesized in nanopores has the potential to be used as conducting polymer [16] or the reinforced fillers in the nanocomposites [17].

Nanocomposites are systems of polymer matrix with usually a small amount of nanofiller added to enhance the chemical or physical properties including mechanical, thermal, and barrier properties. [26] For in situ polymerization, the first step is swelling the nanofiller or nanoclay in the monomer for specific time depending on the interaction between monomer and inorganic filler surface. After the monomers move into the space between layered silicates, the polymerization can be achieved when the reaction conditions are met. Our current work shows that the nanopores exert a catalytic effect so that the reaction kinetics increase due to confinement effects and/or specific interactions between PMMA and SiOH. However, the role of nanofiller may be more complicated since the nanofiller can be regarded as radical

scavenger that terminates the active primary free radicals to reduce the propagation rate or it may work as the barrier to increase the collision frequency for reactants and accelerate propagation. [27] Therefore, future work may include the extension of the current reaction kinetic studies to in situ polymerized PMMA nanocomposites.

References

1. Zhao HY, Simon SL. "Methyl methacrylate polymerization in nanoporous confinement" *Polymer* 2011;52:4093-4098.
2. Begum F, Zhao HY, Simon SL. "Modeling methyl methacrylate free radical polymerization: Reaction in hydrophilic nanopores" *Polymer* 2012;53:3238-3244.
3. Begum F, Zhao HY, Simon SL. "Modeling methyl methacrylate free radical polymerization: Reaction in hydrophobic nanopores" *Polymer* 2012;53:3261-3268.
4. Zhao HY, Yu ZN, Begum F, Hedden RC, Simon SL. "The effect of nanoconfinement on methyl methacrylate polymerization: T_g , molecular weight, and tacticity" *Polymer* 2014;55:4959-4965.
5. Achilias DS, Kiparissides C. "Development of a general mathematical framework for modeling diffusion-controlled free-radical polymerization reactions" *Macromolecules* 1992;25:3739-3750.
6. Uemura T, Ono Y, Kitagawa K, Kitagawa S. "Radical Polymerization of Vinyl Monomers in Porous Coordination Polymers: Nanochannel Size Effects on Reactivity, Molecular Weight, and Stereostructure" *Macromolecules* 2008;41:87-94.
7. Keddie JL, Jones RAL, Cory RA. "Size-dependent depression of the glass transition temperature in polymer films" *Europhysics Letters* 1994;27:59-65.

8. O'Connell PA, McKenna GB. "Dramatic stiffening of ultrathin polymer films in the rubbery regime" *European Physical Journal E* 2006;20:143-150.
9. Moad G, Chong YK, Postma A, Rizzardo E, Thang SH. "Advances in RAFT polymerization: the synthesis of polymers with defined end-groups" *Polymer* 2005;46:8458-8468.
10. Kamigaito M, Ando T, Sawamoto M. "Metal-catalyzed living radical polymerization: discovery and developments" *The Chemical Record* 2004;4:159-175.
11. Kamigaito M, Watanabe Y, Ando T, Sawamoto M. "A new ruthenium complex with an electron-donating aminoindenyl ligand for fast metal-mediated living radical polymerizations" *Journal of the American Chemical Society* 2002;124:9994-9995.
12. Mayadunne RTA, Rizzardo E, Chiefari J, Chong YK, Moad G, Thang SH. "Living radical polymerization with reversible addition-fragmentation chain transfer (RAFT polymerization) using dithiocarbamates as chain transfer agents" *Macromolecules* 1999;32:6977-6980.
13. Wu CG, Bein T. "Conducting polyaniline filaments in a mesoporous channel host" *Science* 1994;266:1013-1015.
14. Kageyama K, Tamazawa J, Aida T. "Extrusion polymerization: catalyzed synthesis of crystalline linear polyethylene nanofibers within a mesoporous silica" *Science* 1999;285:2113-2115.

15. Petersen K, Johannsmann D. "Measurements on the surface glass transition of PMMA from the decay of imprinted surface corrugation gratings: the influence of molecular weight" *Journal of Non-Crystalline Solids* 2002;307-310:523-537.
16. Enzel P, Bein T. "Inclusion of polyaniline filaments in zeolite molecular sieves" *Journal of Physical Chemistry* 1989;93:6270-6272.
17. Moller K, Bein T, Fischer RX. "Entrapment of PMMA polymer strands in micro-and mesoporous materials" *Chemistry of Materials* 1998;10:1841-1852.
18. Uemura T, Ono Y, Hijikata Y, Kitagawa S. "Functionalization of coordination nanochannels for controlling tacticity in radical vinyl polymerization" *Journal of the American Chemical Society* 2010;132:4917-4924.
19. Odian G. *Principles of Polymerization*. 3rd ed. New York: Wiley; 2004.
20. Brandrup J, Immergut EH, Gulke EA. *Polymer Handbook*. 4th ed. New York: Wiley; 1999.
21. De Gennes PG. *Scaling Concepts in Polymer Physics*. Ithaca, NY: Cornell University Press; 1979.
22. Kong CY, Muthukumar MJ. "Polymer translocation through a nanopore. II. Excluded volume effect" *Journal of Chemical Physics* 2004;120:3460-3466.
23. Sakaue T, Raphael E. "Polymer chains in confined spaces and flow-injection problems: some remarks" *Macromolecules* 2006;39:2621-2628.
24. Cacciuto A, Luijten E. "Self-avoiding flexible polymers under spherical confinement" *Nano Letters* 2006;6:901-905.

25. Nising P, Meyer T. "Thermal initiation of MMA in high temperature radical polymerizations" *Industrial and Engineering Chemistry Research* 2004;43:7220-7226.
26. Giannelis EP, Krishnamoorti R, Manias E. "Polymer-silicate nanocomposites: model systems for confined polymers and polymer brushes" *Advances in Polymer Science* 1998;138:107-147.
27. Siddiqui MN, Redhwi HH, Verros GD, Achilias DS. "Evaluating the role of nanomontmorillonite in bulk in situ radical polymerization kinetics of butyl methacrylate through a simulation model" *Industrial & Engineering Chemistry Research* 2014;53:11303-11311.